AFOSR-TR· ⠄ 2 ⠄⠄ 5 3

AD-A256 153

ULTRASTRUCTURE PROCESSING AND ENVIRONMENTAL STABILITY OF ADVANCED STRUCTURAL AND ELECTRONIC MATERIALS

FINAL REPORT

to

AIR FORCE OFFICE OF SCIENTIFIC RESEARCH
Bolling Air Force Base, DC 20332

Contract No. F49620-88-C-0073

Period Covered

April 1, 1988 - July 31, 1992

**DTIC
ELECTE
OCT 0 7 1992
A D
S**

Submitted by

L. L. Hench

*Advanced Materials Research Center
University of Florida
One Progress Blvd., #14
Alachua, Florida 32615*

92-26590
‖‖‖‖‖‖‖‖‖‖‖‖

Copyright: 1992

92 10 6 071

REPORT DOCUMENTATION PAGE	*Form Approved* OMB No. 0704-0188

a. REPORT SECURITY CLASSIFICATION Unclassified	1b. RESTRICTIVE MARKINGS

a. SECURITY CLASSIFICATION AUTHORITY	3. DISTRIBUTION / AVAILABILITY OF REPORT Approved for public release: Distribution unlimited
2b. DECLASSIFICATION / DOWNGRADING SCHEDULE	

PERFORMING ORGANIZATION REPORT NUMBER(S) Annual Report	5. MONITORING ORGANIZATION REPORT NUMBER(S)

a. NAME OF PERFORMING ORGANIZATION University of Florida	6b. OFFICE SYMBOL (If applicable)	7a. NAME OF MONITORING ORGANIZATION Air Force Office of Scientific Research/NC

6c. ADDRESS (City, State, and ZIP Code) Advanced Materials Research Center One Progress Blvd., #14 Alachua, Florida 32615	7b. ADDRESS (City, State, and ZIP Code) Bldg. 410 Bolling Air Force Base, DC 20332

a. NAME OF FUNDING / SPONSORING ORGANIZATION AFOSR	8b. OFFICE SYMBOL (If applicable) NC	9. PROCUREMENT INSTRUMENT IDENTIFICATION NUMBER F49620-88-C-0073

8c. ADDRESS (City, State, and ZIP Code) Bldg 410 BAFB DC 20332	10. SOURCE OF FUNDING NUMBERS

PROGRAM ELEMENT NO.	PROJECT NO.	TASK NO	WORK UNIT ACCESSION NO.
61102F	2303/A3		

11. TITLE (Include Security Classification)
ULTRASTRUCTURE PROCESSING AND ENVIRONMENTAL STABILITY OF ADVANCED STRUCTURAL AND ELECTRONIC MATERIALS

12. PERSONAL AUTHOR(S)
Hench, Larry L.

13a. TYPE OF REPORT Final	13b. TIME COVERED FROM 4/1/88 TO 7/31/92	14. DATE OF REPORT (Year, Month, Day) 920831	15. PAGE COUNT 114

16. SUPPLEMENTARY NOTATION

COSATI CODES			18. SUBJECT TERMS (Continue on reverse if necessary and identify by block number)
FIELD	GROUP	SUB-GROUP	glass, surfaces, optics, ultrastructure, infrared reflection spectroscopy, microstructure, gels, gel-glass transformation, processing, composites, silica, noise, powders, superlattices, metal organic precursors, drying, thermal

19. ABSTRACT (Continue on reverse if necessary and identify by block number)

The goals of this Multi-Investigator Research Program (MIRP) are: 1) achieve an understanding of the science of ultrastructure processing, and 2) apply the science of ultrastructure processing to produce new optical, electronic, optoelectronic, and structural materials. Ultrastructure processing refers to the manipulation and control of chemistry based processes to attain a new generation of high performance materials. Problem areas to benefit from ultrastructure processing include: advanced optical and opto-electronic systems, non-linear optical matrices, laser hosts, controlled particulates, transpiration cooled optics, effects of energetic particle beams, electronic behavior of high band gap semiconductors. Six projects are pursued. A cumulative list of the 60 papers published and 11 patents submitted during this contract is presented. A few papers from each project published during 1991-92 are presented.

Project A: Sol-Gel Processing Science. Three papers describe the physical chemical factors and structural evolution and characterization of the sol-gel processing of large SiO_2 monoliths. Real time monitoring of the drying behavior of large silica gels is reported. A third paper reports on sol-gel derived titania-silica glasses with FTIR and structural characterization.

20. DISTRIBUTION / AVAILABILITY OF ABSTRACT ☒ UNCLASSIFIED/UNLIMITED ☒ SAME AS RPT ☐ DTIC USERS	21. ABSTRACT SECURITY CLASSIFICATION Unclassified
22a. NAME OF RESPONSIBLE INDIVIDUAL Thomas E. Erstfeld	22b. TELEPHONE (Include Area Code) 202-767-4960	22c. OFFICE SYMBOL NC

DD Form 1473, JUN 86   *Previous editions are obsolete*   SECURITY CLASSIFICATION OF THIS PAGE

i

18.   Subject Terms (Continued)

analysis, aging, band gap, substrates, quartz, adsorption, polysilicon, space charge limited flow, molecular orbital calculations, INDO, water, transpiration cooling, windows, ultraviolet, near infrared, topology, quantum mechanics, lasers, dyes, bioactivity, implants, amino acids, membranes, fluorescence, positronium decay.

19.   Abstract (Continued)

Project B: *Sol-Gel Glass Applications*. Two papers describe the processing of two new types of gel-silica optics: Type V full density ultrahigh purity gel-silica and Type VI ultraporous gel-silica optical matrices. Use of the Type VI materials in multifunctional silica optics is described, with the special emphasis on optical composites. The description and use of precision multifunctional optics is discussed which provides the basis for producing waveguides, optical interconnects and hermetic isolation of optical polymers within the gel matrices.

Project C: *Theoretical Calculations of Gel-Silica*. One paper is presented which describes the use of semi-empirical molecular orbital methods to analyze the chemistry of sol-gel silica clusters with special emphasis on rings and chains and the optical properties of the clusters. theoretical and experimental results are compared.

Project D: *Biological Applications of Sol-Gel Science*. Two papers are included which discuss the use of sol-gel processing to produce a new generation of bioactive implant materials which have higher rates of bioactivity than materials made by traditional processing methods. The kinetics of bioactive ceramics are described and related to their biological behavior.

Project E: *Electronic Characterization of Semiconductor Interfaces*. One report is presented which describes visible light emission from porous silicon homojunction diodes.

Project F: *General Materials Science*. One paper is included. This paper is a collaborative study with the University of Nagoya in Japan on protonic conduction in phosphate glasses.

Accesion For		
NTIS CRA&I		☑
DTIC TAB		☐
Unannounced		☐
Justification		
By		
Distribution		
A-		
Dist		

A-1

ii

TABLE OF CONTENTS

SECTION I

INTRODUCTION

a. Overview of Program Goals and Progress

The goals of our Multi-Investigator Research Program (MIRP) are: 1) to achieve an understanding of the science of ultrastructure processing of glasses, ceramics and composites, and 2) apply the science of ultrastructure processing to produce new optical, electronic, optoelectronic, and structural materials. Ultrastructure processing as used in our program and in this report refers to the manipulation and control of chemistry based processes for the purpose of attaining a new generation of high performance materials with unique properties.

The primary emphasis of the MIRP is devoted to the science and application of sol-gel processing to achieve a new generation of optical and optoelectronic materials with unique properties. The rationale for this emphasis on sol-gel processing is the low thermal requirements to produce materials in this way and the unique physical properties that result. Net shapes of optical components can be made using our sol-gel processing method thereby eliminating costly grinding and polishing. Micro-optical components can be produced reliably and inexpensively by use of plastic molds for casting the sols. Two new types of optical silicas and important new optical devices have resulted from alkoxide sol-gel processing.

An important material characteristic of sol-gel derived materials is the very large (30-70%) percentage of microporosity in the materials after drying. Consequently a wide range of physical properties can be achieved with materials of the same chemical composition by varying the volume fraction, size distribution, and connectivity of the microporosity. Impregnation of the optically transparent microporous structures to produce a wide range of composite optical materials is also possible. Preparation of sol-gel derived materials with

1

reinforcing whiskers, fibers, or weaves is also possible resulting in an even wider range of properties.

Consequently, one of our operating hypotheses for the MIRP is that understanding the chemistry of sol-gel derived materials will make it possible to achieve unique combinations of physical properties to fulfill a broad range of design objectives.

Because of the breadth of this objective we pursue two parallel paths in our sol-gel studies: 1) Sol-gel monoliths, and 2) Theoretical predictions of sol-gel structures and processing. Previous efforts on organometallic precursors, solution derived particulates, and sol-gel coatings have been phased out of the MIRP. This has made it possible to concentrate on achieving a new generation of optical materials during the last two years of research. The collection of papers listed in Part IX in this report illustrate the rapid growth of our contribution to both the science and the technology of this new field. For example, Project A is focused on the chemistry of sol-gel derived silica monoliths using alkoxide precursors. The papers discuss in detail the several steps involved in the processing of sol-gel derived optical silicas: 1) mixing, 2) casting, 3) gelation, 4) aging, 5) drying, 6) stabilization, and 7) densification. The low temperature sol-gel method developed in the MIRP, using alkoxide precursors, results in an ultrastructure that is approximately 200X smaller than achieved by the colloidal method. Consequently dried and stabilized gel monoliths made by the University of Florida MIRP route are optically transparent and can be used for transmission optics. This new material, with properties unique to any previous optical material, has been designated Type VI optical silica. The development and characterization of this new optical material is discussed in several papers. The optically transparent ultraporous Type VI silica can be impregnated with a broad range of optically active polymers, as discussed in Project B. It also can be used as a substrate for laser densified structures.

2

Full density is achieved in the alkoxide sol-gel derived silica, termed Type V gel-silica, at 1150°C. This low temperature is in contrast to the colloidal sol-gel method which requires 1450-1720°C. The physical properties of the Type V alkoxide gel-silica optics developed in the MIRP are superior to most optical silicas. The optical transmission is higher throughout the Vacuum UV, UV, Visible, and near IR than other silicas, the homogeneity of index of refraction is better, strain birefringence lower, and other defects such as bubbles and inclusions are non-existent. The coefficient of thermal expansion is also substantially lower than other silicas, such as the NIST standard silica. Thus, the MIRP Type V optical silica is as close to an intrinsic amorphous silica as has ever been made. Because of the importance of the development of these new silica materials a new direction for the MIRP was launched during this contract, theoretical predictions of ultrastructured materials based upon quantum mechanical molecular orbital calculations. This effort, headed by Dr. Jon West, has been in collaboration with the AFOSR theoretical silicon chemistry group of Professor Marc Gordon, North Dakota State University and Drs. Larry Burgraff and Larry Davis, AFOSR, and the University of Florida Quantum Theory Project with Professor Mike Zerner participating. INDO, and AM-1 (MOPAC) and HMO calculations have been completed for a wide range of silica clusters with and without extrinsic defects. Predictions of the size of our acid catalyzed alkoxide gel ultrastructures have been achieved along with the theoretical UV cut-off of our Type V optical silica. Effects of extrinsic OH on optical absorption have also been predicted. Calculations of the effects of H_2O on the silica structures correspond to experimental dilatometry and NIR measurements.

The MIRP continues to support the interdisciplinary work between the Departments of Electrical Engineering and Materials Science and Engineering in the area of understanding the electron transport and noise of semiconductor devices. This program, albeit a small one, continues to produce a very high level of science in a field that may evolve into a new

direction for ultrastructured quantum well high band gap devices. A new Monte Carlo method of simulating charge transport in GaAs two terminal devices has been reported previously by Professor Bosman's group and this report presents new work on visible light emission of P-N porous silicon homojunction diodes.

A collaboration was also launched with Professor Hsieh of the University of Florida Mechanical Engineering Department in the area of theoretical modelling of laser densification which has resulted in a couple of papers.

One of the distinguishing features of the MIRP is a continuing series of interinstitutional collaborations. The cooperative effort in quantum calculations was mentioned earlier. Similarly, the collaboration with the University of Illinois Chemistry Department and Professor Jeri Jonas continues to be profitable. New directions were launched during this contract with Texas Christian University and Professor T. Zerda with results published that describe use of positronium decay analysis of the pore distribution of gel monoliths. A long standing interaction with Professor Y. Abe of Nagoya University in Japan has resulted in a series of papers on proton conduction in oxide glasses, Project F.

A new direction was launched in this contract to integrate our efforts in understanding the molecular level of silica structural evolution with biological processes. Two papers are included in Project D and experimental work on sol-gel derived bioactive materials has led to a new generation of alkali-free bioactive materials with a much broader range of composition. These new $CaO-P_2O_5-SiO_2$ gel-glasses have higher levels of bioactivity than any other material. They are protected by patent.

The MIRP has pursued a broad base of process and application patents which are listed in Section X. Most are licensed and production of gel-derived silica optics is underway by the licensee.

4

In summary, the MIRP continues to serve as an excellent management vehicle for initiating exciting new directions in chemically derived materials with unique ultrastructures. Projects that offer the most promise for eventual employment in DOD systems are maintained long enough to achieve statistically significant property measurements and reliability analysis. Prototypes of useful devices are produced, characterized and tested. The technology for these successful new materials, such as Type V and Type VI optical silicas, is transferred by licensing arrangements of the University of Florida to a U.S. corporation (Geltech, Inc.) for scale-up to manufacturing. Products made by sol-gel processing developed by the MIRP are now being supplied to a large number of DOD contractors. This linkage between basic science - applied science - and product development has been very successful and is one of the main strengths and accomplishments of the MIRP. This effort has been published as a semi-quantitative model of technology transfer processes.

Projects that have been interesting and fruitful from a publication standpoint but show meager potential for eventual DOD application are phased out from support by the MIRP upon graduation of the students.

In this manner the MIRP maintains a health and vitality that we believe makes each year's achievements new and exciting.

The last two sections of this report itemize a complete list of the publications and patent applications for the four (4) year AFOSR MIRP program.

SECTION II

LIST OF PROJECTS AND FACULTY INVESTIGATORS

<u>PROJECT</u>

A: **Sol-Gel Processing Science**
L. L. Hench and J. K. West

B: **Sol-Gel Glass Applications**
L. L. Hench, J. K. West, and C. K. Hsieh

C: **Theoretical Calculations of Gel-Silica**
J. K. West, L. L. Hench, and S. Wallace

D: **Biological Applications of Sol-Gel Science**
L. L. Hench, J. Wilson, A. E. Clark, and G. LaTorre

E: **Electronic Characterization of Semiconductor Interfaces**
G. Bosman and C. Van Vliet

F: **General Materials Science**
L. L. Hench and Y. Abe

SECTION III

PROJECT A:
Sol-Gel Processing Science

15

a. SOL–GEL PROCESSING OF LARGE SILICA OPTICS

L.L. HENCH, M. J. R. WILSON, C. BALABAN, AND J. L. NOGUÈS

15.1. INTRODUCTION

In the first Ultrastructure Processing Conference in 1983, J. D. Mackenzie summarized numerous potential advantages and disadvantages of sol–gel processing [1]. The advantages cited were largely based upon the intimate mixing possible with chemically based processing compared with powder processing. The disadvantages primarily centered around the difficulties in controlling this new generation of molecular-based processing and potential costs.

The objective of this Chapter is to summarize and present, 6 years later, the progress made in achieving the advantages and minimizing the disadvantages in the sol–gel processing of one important application, sol–gel-derived silica optics. The potential advantages discussed are homogeneity, purity, coefficient of thermal expansion, As-cast shapes and surface features, and unique properties of silica ultrastructures, such as for doping applications and laser-enhanced densification.

The possible disadvantages discussed in this Chapter are inherent to size scaleup. They can be in most cases overcome by well-defined processing including control of drying, elimination of casting defects, and precise at-

mosphere control. The consequence of overcoming most of these problem areas is the ability to make new types of silica optics with sizes of 100 mm and larger using organometallic-based sol–gel silica processing.

15.2. SILICA OPTICS PROCESSING

Silica optics are preferred for many optical systems, such as intracavity laser optics, because of the characteristics listed in Table 15.1. Development of a successful sol–gel-derived process for making silica optics requires achieving all the features listed in this table. It also requires achieving significant improvements in at least some of the most important properties over what is presently produced commercially.

There are presently four major methods of manufacturing silica optics, as summarized in Table 15.2 [2,3]. The first two processes involve melting naturally occurring quartz crystals at high temperatures. The resulting materials are termed *fused quartz*. Deficiencies of fused quartz optics can include: substantial amounts of cation impurities (type I), hydroxyl impurities (type II), inhomogeneities, seeds, bubbles, inclusions, and microcrystallites. The relative extent of these defects depends on the grade of fused quartz. The higher the grade, the fewer the defects, but the higher the cost and the more difficult the production of large optics.

Both types III and IV are termed *synthetic fused silica*. The cation impurity content of fused silica optics is substantially lower than fused quartz optics due to the higher purity of the raw materials [3]. It is difficult for the chemical reactions indicated in Table 15.2 for these types of silica to go to completion, consequently water contents up to a few thousand parts per million are present in type III silica, and Cl ion contents of a few hundred parts per million can be retained as an unreacted residue in both type III and type IV silicas. Other defects are somewhat lower for fused silicas than for fused quartz [3]. The nature of the chemical processes involved in the production of types III and IV silicas

TABLE 15.1. Features of Silica Optics

1. Excellent optical transmission from the ultraviolet (160 nm) to near infrared wavelengths (3600 nm)
2. Excellent refractive index homogeneity.
3. Isotropic optical properties.
4. Small strain birefringence.
5. Very low coefficient of thermal expansion of about $0.55 \times 10^{-6}/°C$.
6. Very high thermal stability.
7. Very high chemical durability.
8. Small numbers of bubbles or inclusions.
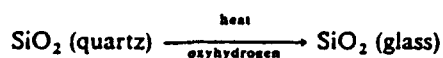9. Ability to be polished to high standards.

**TABLE 15.2. Methods of Silica Optics Manufacture**

Fused Quartz

Type I: Electric melting of natural quartz crystals

$$SiO_2 \text{ (quartz)} \xrightarrow[\text{vacuum}]{\text{heat}} SiO_2 \text{ (glass)}$$
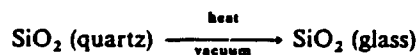
Type II: Flame fusion of natural quartz crystals

$$SiO_2 \text{ (quartz)} \xrightarrow[\text{oxyhydrogen}]{\text{heat}} SiO_2 \text{ (glass)}$$

Fused Silica

Type III: Vapor-phase hydrolysis of pure silicon tetrachloride carried out in a flame

$$SiCl_4 + O_2 + 2H_2 \rightarrow SiO_2 \text{ (glass)} + 4HCl$$
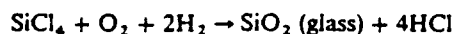
Type IV: Oxidation of pure silicon tetrachloride, which is fused electrically or by means of a plasma

$$SiCl_4 + O_2 \rightarrow SiO_2 \text{ (glass)} + 2Cl_2$$

Gel-Silica

Type V: Gelation of alkali silicate colloidal solutions with fully densification (1500 to 1720°C), or
Hydrolysis and condensation of organometallic precursor with fully densification (1150 to 1200°C)

$$Si(OR)_4 + 4H_2O \rightarrow Si(OH)_2 + 4(ROH)$$

$$Si(OH)_4 \rightarrow SiO_2 \text{ (dense gel-silica)} + 2(H_2O)$$
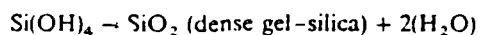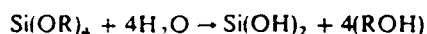
Type VI: Hydrolysis and condensation of organometallic precursor with partial densification (600 to 950°C)

$$Si(OR)_4 + 4H_2O \rightarrow Si(OH)_4 + 4(ROH)$$

$$Si(OH)_4 \rightarrow SiO_2 \text{ (porous gel-silica)} + 2(H_2O)$$

---
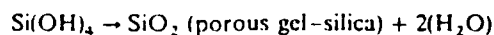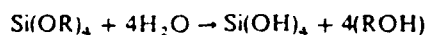
makes the direct manufacture of near net shape optics impossible. Price increases considerably as the quality of fused silica and the size of the optics increase.

During the last few years chemically based sol-gel processes have been developed and lead to the manufacture of types V and VI silicas as described in Table 15.2 [3–6]. These processes offer the potential for improving many

10

features of silica optics listed in Table 15.1. Additional advantages over types I to IV silicas are also possible, as described in Table 15.3.

Two primary sol-gel processing methods for silica optics have reached commercialization: (1) hydrolysis and condensation of an organometallic precursor [3-5] and (2) gelation of a colloidal alkali silicate powder suspension [6]. The silicas resulting from these sol-gel processes are termed *type V* when the final product is fully dense with no residual porosity. If the densification process is not accomplished entirely, the organometallic method produces a porous optical material named *type VI silica*.

The ultrastructure of the gel and the final densification conditions are considerably different for the organometallic versus the colloidal methods of manufacture of sol-gel silicas, as summarized in Fig. 15.1. An organometallic-based sol-gel silica, such as Gelsil™†, has a totally interconnected porosity with a dried bulk density of 1.2 g/cm³, an average pore diameter of 2.5 nm, and a specific surface area of 700-800 m²/g prior to densification [3]. Because of the very small pore size and the very narrow distribution of pores, the gel is optically

TABLE 15.3. Potential Advantages of Gel-Silica Optics

Net Shape/Surface Casting

Complex geometries
Light weight optics
Aspheric optics
Surface replication (e.g., Fresnel lenses)
Internal structures
Reduced grinding
Reduced polishing

Improved Physical Properties (Type V) .

Lower coefficient of thermal expansion
Lower vacuum ultraviolet cutoff wavelength
Higher optical transmission
No absorption due to H_2O or OH bands
Lower solarization
Higher homogeneity
Fewer defects

Transparent Porous Structures (Type VI)

Impregnation with organic polymers
Graded refractive index lenses
Laser-enhanced densification
Controlled chemical doping
Control of variable oxidation states of dopants

---

†Gelsil™ is a trademark of GELTECH, Inc.
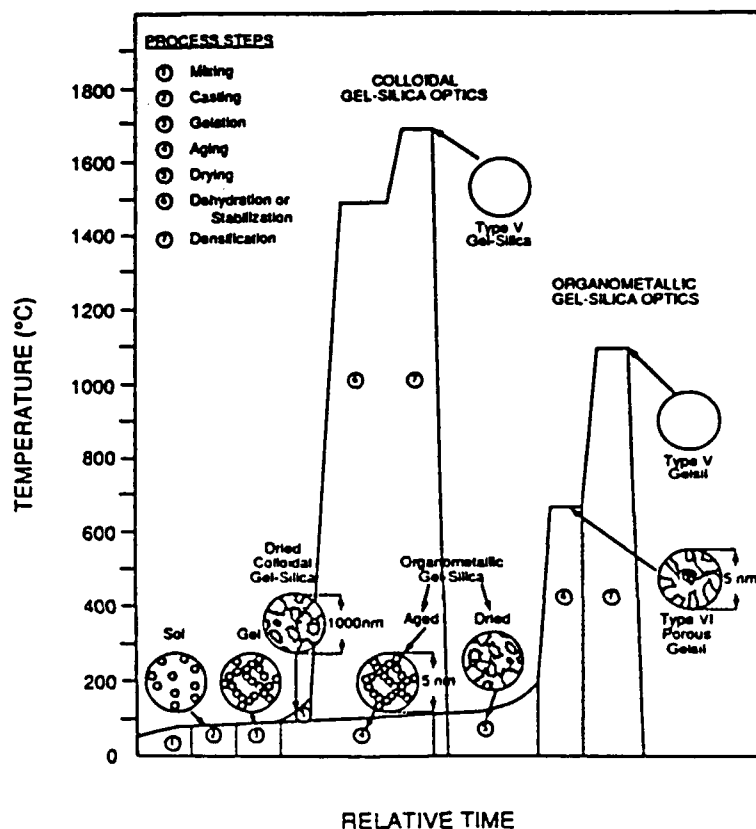
11

Gel-Silica Glass Process Sequence

Figure 15.1. Processing sequence for sol-gel silica optics.

transparent. The uniformity of the ultrastructure results in densification at a very low temperature, 1150°C, without a change in mean pore radius. Densification takes place almost entirely by decreasing the connectivity (genus) of the uniform pore network [7] and is very sensitive to pore size, as shown in Fig. 15.2.

Because there is no pore growth by Ostwald ripening, the organometallic derived monoliths remain optically transparent throughout the processing schedule shown in Fig. 15.1, after they pass the opaque stage in drying (Chapter 22). Examples of a large 100-mm organometallic sol-gel-derived optical silica monolith after drying is shown in Fig. 15.3a. Samples of organometallic-derived type VI and type V silica plano-plano optical components are shown in Figs. 15.3b and c, respectively.

The colloidal sol-gel optics process developed by Shoup [6] involves nucleation and polymerization of potassium silicate by colloidal silica in the presence of a hydrolytic organic reagent. By varying the ratio of colloidal species
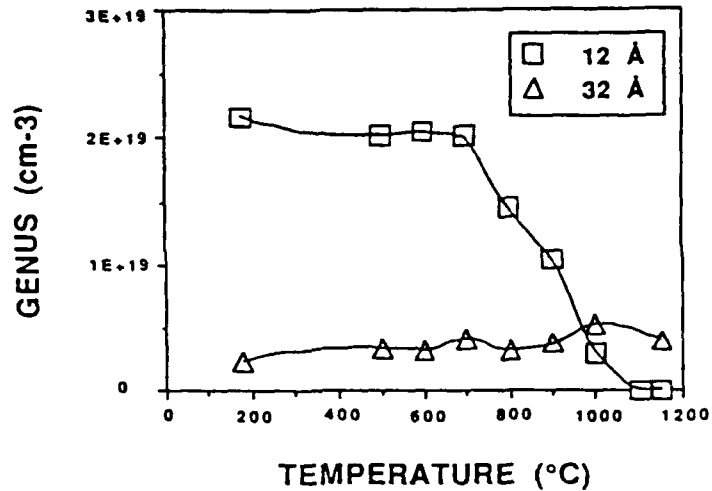
Figure 15.2. Temperature dependence on pore network connectivity of organometallic gel-silicas with differing mean pore radii. (Data courtesy of W. Vasconcelos, University of Florida.)
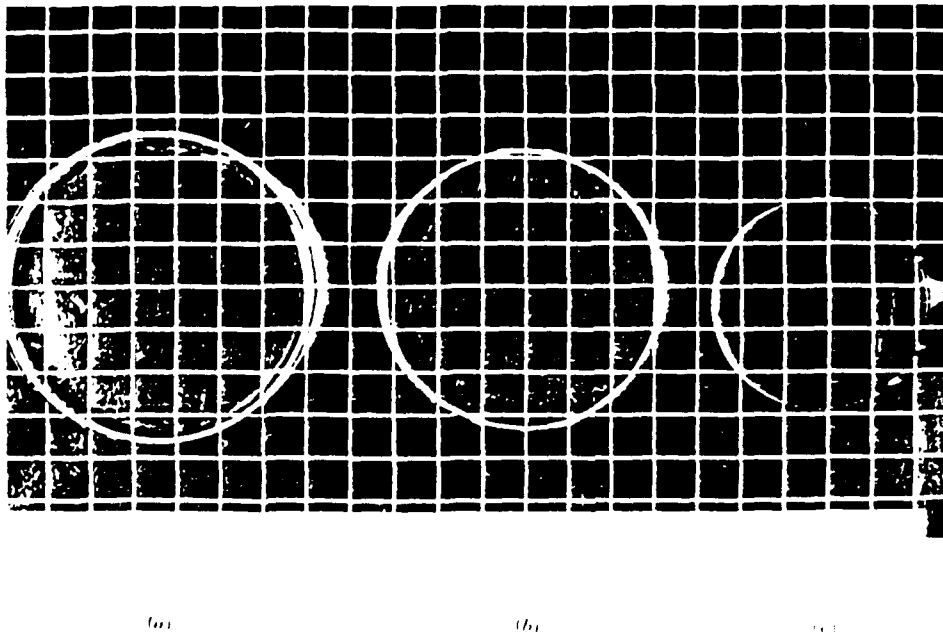

Figure 15.3. Organometallic sol-gel silica monoliths (a) dried, (b) porous plano-plano optical component (type VI Gelsil™), (c) fully dense plano-plano optical component (type V Gelsil™)

13
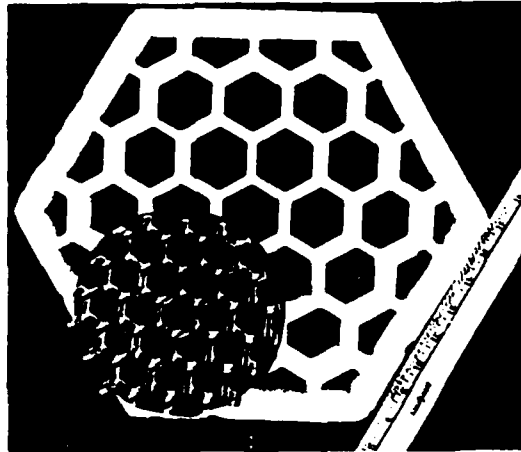
Figure 15.4. Lightweight mirror backing made by colloidal gel–silica process: (*a*) after drying, (*b*) after densification. (Photo courtesy of R. D. Shoup, Corning Glass Works.)

to soluble silicate, the gel pore diameter can be controlled between 10 and 300 nm with a relatively narrow size distribution. As a result, strong silica gel structures are formed by the colloidal process with large pores, >200 nm diameter, that can resist capillary pressures encountered during drying. Microwave drying can be used for these $\geqslant 80\%$ porous colloidal gels in minutes to hours, depending on body dimensions, without cracking.

The large-pore structures produced in the colloidal sol–gel method help in the removal of alkali ions by an aqueous dealkalization process. The large pores also facilitate gaseous removal of chemisorbed impurities prior to densification, yielding low water levels and alkali and transition metal impurity of a few

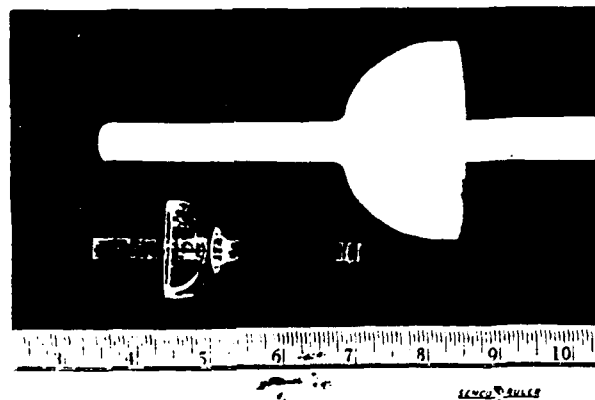**Figure 15.5.** Near net-shape colloidal gel–silica component: (*a*) after drying, (*b*) after densification. (Photo courtesy of R. D. Shoup Corning Glass Works.)

14

hundred parts per million. Total density is achieved after 30 min at 1500°C and high-quality optical silica is achieved after 10 min at 1720°C. Examples of type V silica glasses made by the colloidal gel–silica process are shown in Figs. 15.4 and 15.5.

15.3. FACTORS IN SIZE SCALEUP

Scaleup of sol–gel processing has been considered potentially one of the greatest uncertainties. In order to achieve large optical components by the sol–gel route it is essential to control: (1) drying rates, (2) defects in the as-cast gel monoliths, and (3) removal of chemisorbed water prior to pore closure in densification. Control of these factors is less sensitive in the colloidal method because of the large pores in the structure.

1. *Drying Control.* A critical step in the drying of organometallic-derived sol–gel optics is the rate of removal of water during the "opaque stage." As shown by Wilson and Hench in this text (Chapter 22), it is during the transition between filled pores and pore emptying that substantial bulk strains are developed in the gel monoliths. The rate of water removal must be slowed during this critical period to avoid cracking. The gel monolith is relatively insensitive to the rate of drying prior to and after the opaque stage.

2. *Defect Control.* Imperfections in a gel will cause stress risers during drying and further processings steps. Consequently, even if a gel monolith has sufficient strength to withstand a given level of bulk strain, the presence of stress risers will induce fracture. These imperfections can take many forms and are usually created during casting of the sol and are incorporated in the solid when gelation occurs. Several examples of bubbles, which are particularly damaging stress risers, are shown in Fig. 15.6. In Fig. 15.6a, a
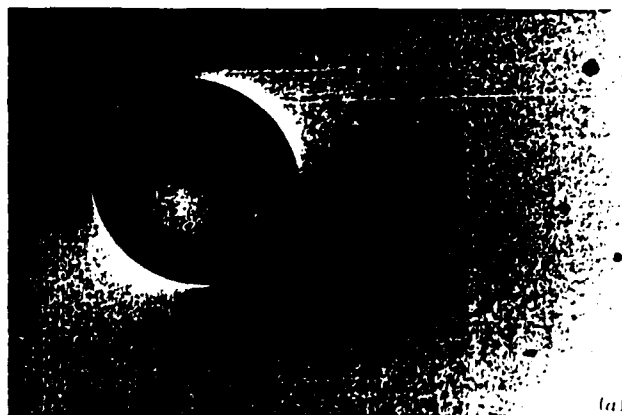

(a)

Figure 15.6. Bubbles in a gel silica monolith (a) acting as a stress riser, (b) initiating a crack, (c) initiating three cracks, and (d) initiating a complex crack front.

stress field is beginning to develop around the bubble; in Fig. 15.6b, we can see a crack initiating from a bubble; in Fig. 15.6c, three cracks have initiated; and in Fig. 15.6d, a complex crack front originates from the interaction of stress fields around two bubbles.

Elimination of bubbles involves careful deareation of the sol prior to casting, using a casting technique that does not introduce air, avoiding gas generating chemical additives in the sol formula, and avoiding containers that nucleate bubbles at the interface.

3. *Atmosphere Control.* Tightly bound hydroxyl ions on the surface of pores must be removed prior to pore closure during densification for both organometallic and colloidal sol-gel silicas. Surface dehydroxylation occurs from 200 to 1000°C for organometallic-derived gels and up to 1300°C for colloidal silica monoliths. It is usually necessary to enhance the dehydroxylation process by flowing halogen-containing gases through the pore network before closure. In this particular case the atmosphere control treatment should include the removal of any halogen left in the structure of the glass. If densification is attempted without hydroxyl removal, foaming and bloating result due to expansion of the gases formed and trapped in the closed pores. Because of the very small size of pores in organometallic-derived gels and the absence of pore growth during densification, it is especially critical to have complete hydroxyl removal for these materials if they are to achieve full density. It is important to recognize that more internal SiOH groups are retained in an acid-catalyzed organometallic-derived gels at high temperature than base-catalyzed gels [8]. The internal SiOH groups polarize the silica tetrahedra [9], which probably is responsible for a decrease in the viscosity of the silica gel network. Consequently viscous flow, responsible for pore closure and reduction of pore network connectivity, takes place at a lower temperature. Thus, it is essential to optimize hydroxyl removal for acid-catalyzed gels when the pore network has as large a connectivity as possible, such as at as low a temperature as possible, for example, below 900°C for small pore organometallic-derived gels (Fig. 15.2).

Control of drying rates, elimination of casting defects, and rigorous atmosphere control can yield large sol-gel silica optical components as shown in Figs. 15.3 to 15.5.

15.4. POTENTIAL ADVANTAGES OF SOL-GEL SILICA OPTICS

15.4.1. Homogeneity

One of the primary incentives for use of chemically based ultrastructure processing of materials is improvement of homogeneity. The fact that or-

17

ganometallic precursors can be hydrolyzed with water on a molecular scale of mixing yields the possibility that the glass structure derived from an organometallic gel may have a molecular level of homogeneity. However, as indicated above macroscopic defects must be eliminated first in order to achieve high levels of homogeneity. Also, processing controls must be developed to eliminate fluctuations in the density and index of refraction during densification.

Successful processing controls have been achieved for organometallic-derived optics up to 75 mm for type V silica and 100 mm for type VI silica (Fig. 15.3). Results from optical property measurements show no evidence of bubbles, no striae, a superior index of refraction homogeneity of about $1-6 \times 10^{-6}$, and very low strain birefringence of 4-6 nm/cm. These characteristics of organometallic-
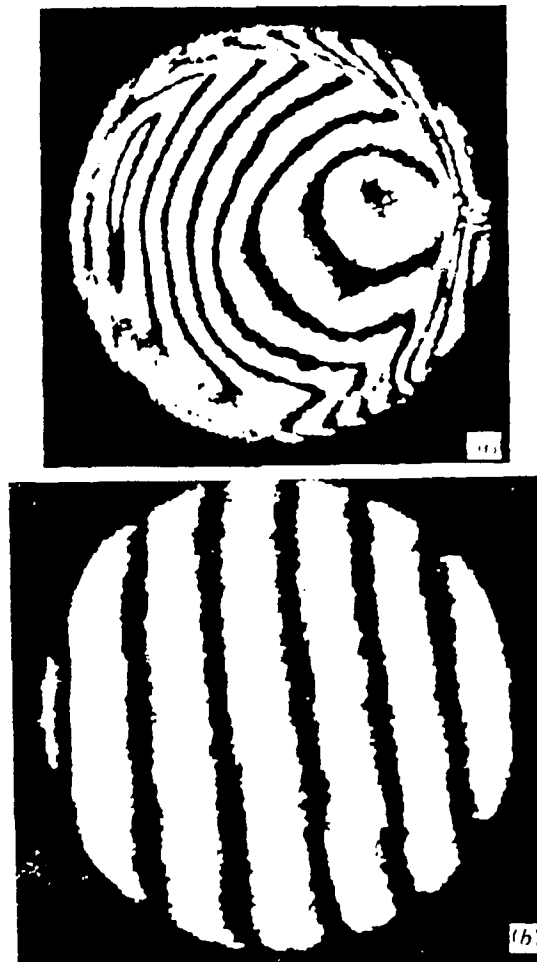

Figure 15.7. Interferometry analysis of dense organometallic gel silicas (type V Gelsil™): (a) improperly densified with severe index gradients. (b) ideal densification with good homogeneity.

18

derived sol-gel silica (Gelsil™) are equal or superior to types I to IV optical silicas. Figure 15.7a is an example of an earlier generation organometallic gel-silica monolith that was homogeneous as a gel, but developed large index of refraction gradients during densification. This type of inhomogeneity can be eliminated, as shown in Fig. 15.7b.

15.4.2. Purity and Properties

Another major incentive for low-temperature, chemically based processing is achieving a higher level of purity than traditional glass and ceramic-processing methods. The organometallic sol-gel glasses have very few cation and hydroxyl impurities. An important consequence of the elimination of impurities is the improvement of transmission throughout the optical spectrum. Figure 15.8 compares the ultraviolet op'ical transmission of two commercial ultraviolet (UV)-grade optical silicas (type III) with a typical spectrum from an organometallic-derived gel-silica (type V). The vacuum UV cutoff wavelength is substantially improved for the gel-silica material. Recent quantum mechanical calculations of West et al. have shown that the greater transmission in the UV can be attributed to a lower alkali and OH radical content in the gel-silica (Chapter 11). Results from the quantum mechanics calculations are compared in Fig. 15.9 with the improvement in gel-silica transmission over the last three Ultrastructure Processing Conferences, as the OH radical content of the gel-silica glasses has been progressively eliminated. The ultraviolet transmission of
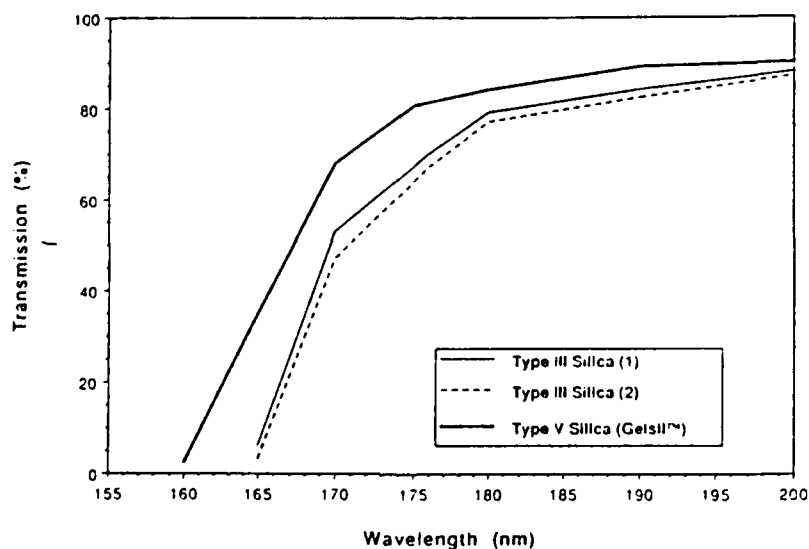

Figure 15.8. Ultraviolet optical transmission of a dense organometallic gel-silica (type V Gelsil™) compared with two commercial type III silicas.

19
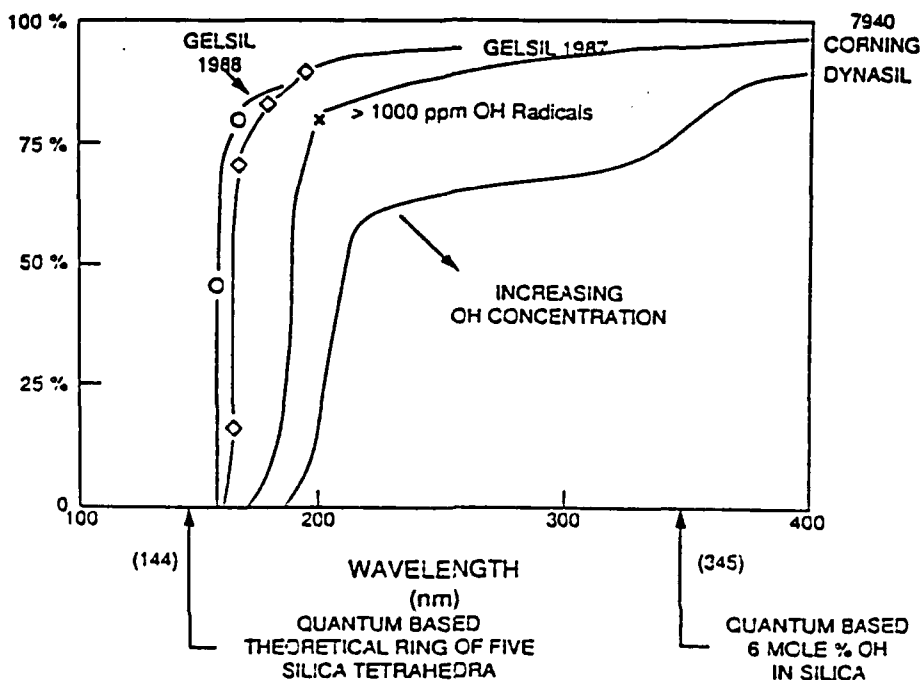
UV TRANSMISSION

Figure 15.9. Improvements in UV transmission of organometallic gel-silicas with time compared with quantum mechanics predictions of UV cutoff wavelength.

colloidal based silica is poorer than organometallic-derived gel-silica due to a higher level of impurity inherent to the alkali-silicate-based colloidal process.

Elimination of OH radicals from gel-silica optics also results in elimination of absorption bands in the near infrared, as shown in Fig. 15.10. This figure shows the difference between type V gel-silica and type III silica, which exhibits absorption bands at 1400 and 2200 nm, and a very broad absorption band at 2730 nm. Reliability of production of low OH radical content in type V gel-silicas (Gelsil™) has also been recently achieved.

15.4.3. Coefficient of Thermal Expansion

A very low coefficient of thermal expansion (CTE) is an especially important physical characteristic of optical silica. The organometallic process leads to the production of a type V silica having a lower CTE than other types of silica. Figures 15.11 and 15.12 compare the thermal expansion and the CTE values of a type V silica (Gelsil™) optics with the NBS silica reference and type III and IV commercial silicas over the temperature range of 25 to 700"C. The organometal-

Figure 15.10. Near infrared transmission of a dense organometallic gel-silica (type V Gelsil™) compared with a type III silica.
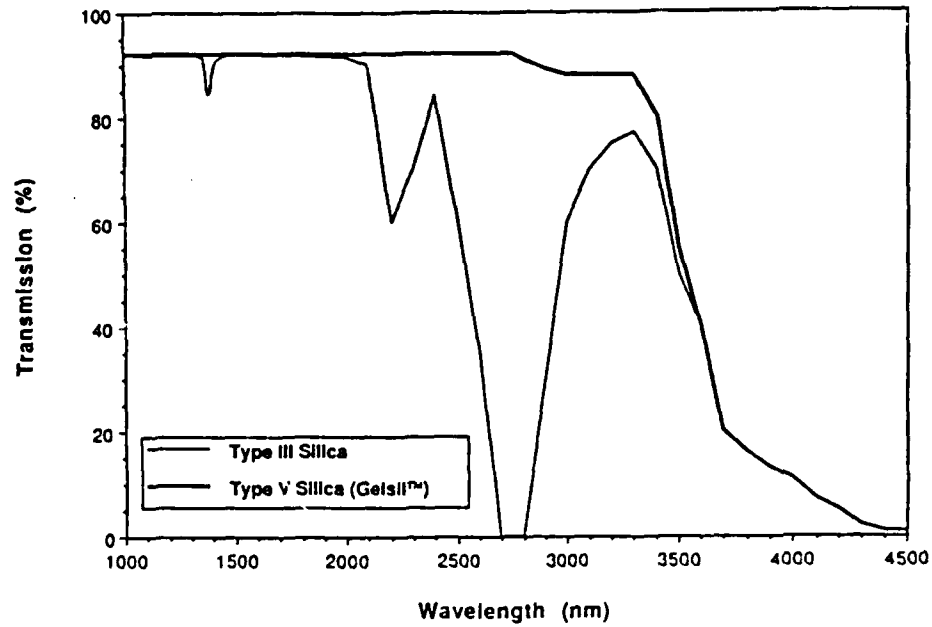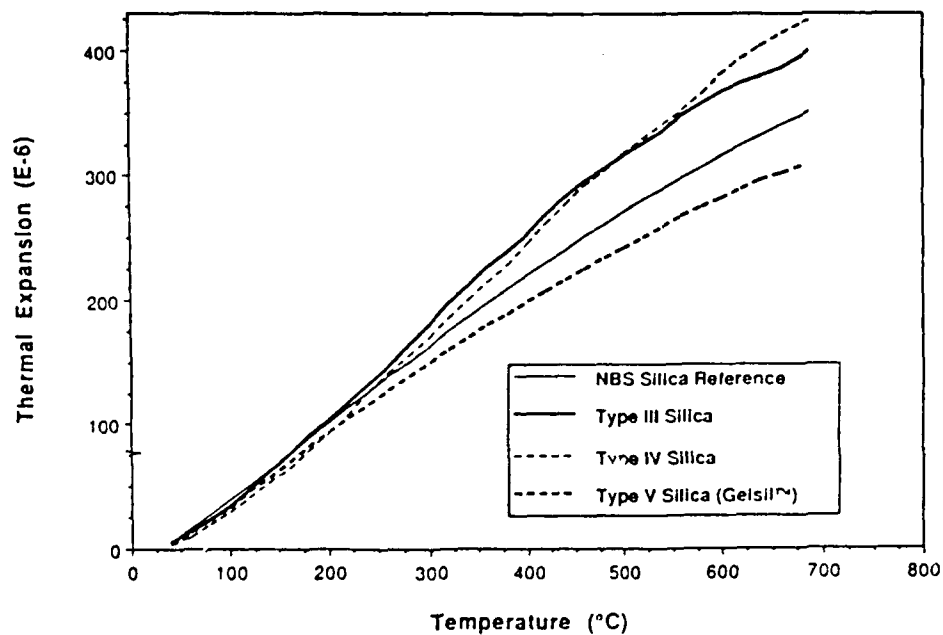

Figure 15.11. Thermal expansion of a dense organometallic gel-silica (type V Gelsil™) compared with NBS silica reference and types III and IV silicas.

21
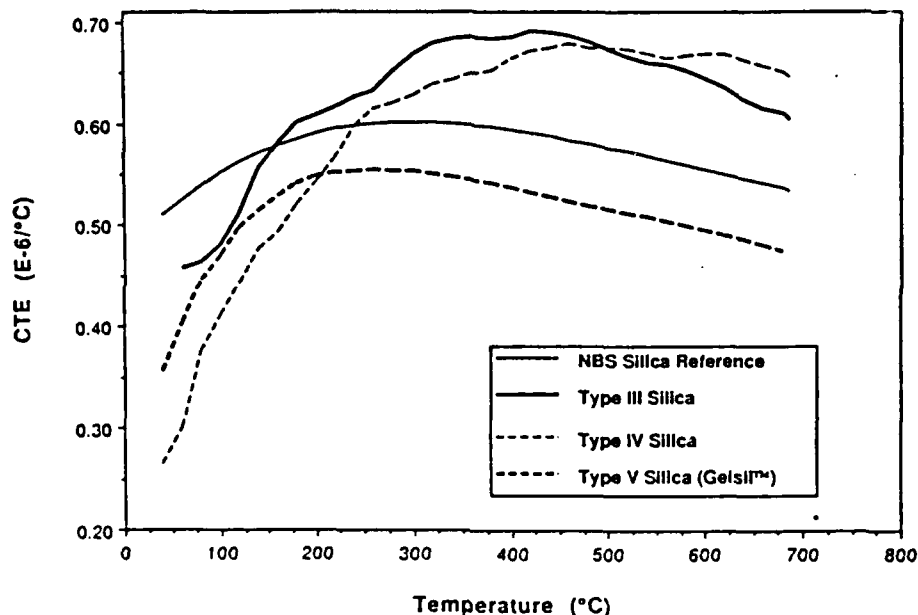
Figure 15.12. Coefficient of thermal expansion (CTE) of a dense organometallic gel–silica (type V Gelsil™) compared with NBS silica reference and types III and IV silicas.

lic sol–gel optical silica have lower values of thermal expansion and CTE than the other types of silica [10].

15.4.4. As-Cast Shapes and Surface Features

Another area of potential advantage of sol–gel optics processing is that of obtaining net shapes and surfaces or at least near-net shapes and surfaces through casting sols at low temperature into molds of predetermined configurations. Advantages offered by this type of processing are listed in Table 15.3. A lightweight mirror with integrally cast face plate and honeycomb backing made by gelation of silica organometallic precursor is shown in Fig. 15.13. This configuration has been successfully dried and a sample of similar size (75 mm in diameter) and shape has been successfully densified. A net shape honeycomb mirror backing made by the colloidal route is shown in Fig. 15.4 and a complex mold casting of colloidal silica gel–glass is shown in Fig. 15.5.

Another application of net shape casting is the replication of specific surface features. For example, Fig. 15.14 shows the surface characteristic graphs obtained on a Sloan Dektak/FLM profilometer of a plastic Fresnel lens master and the corresponding gel–silica Fresnel lens. The lens master was machined in a polymer and the organometallic sol–gel silica positive replica was made by direct casting against it. Figure 15.15 shows a microscope photograph of a dry organometallic sol–gel silica part. It can be seen from this photograph and the
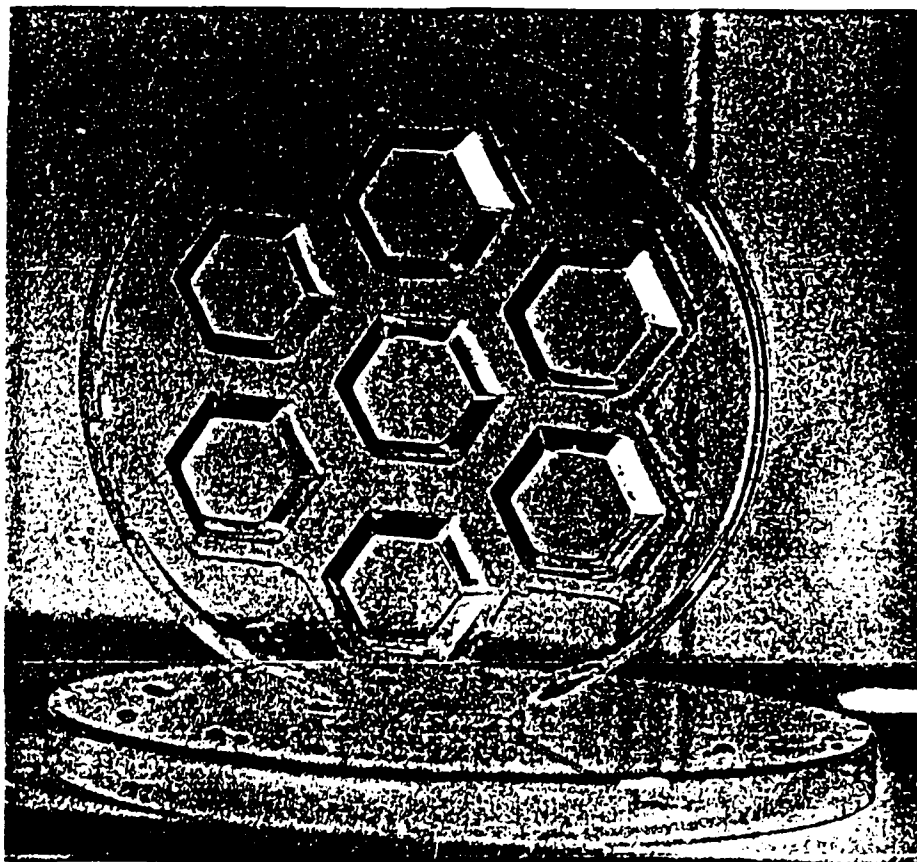
Figure 15.13. Lightweight sol-gel silica mirror with integral faceplate made by the organometallic route. (Photo courtesy of F. West, M. T. P. Wilson, J. Parramore, and B. F. Zhu, University of Florida.)

profilometry graphs that the replication of the surface details is very good. The precision of the master was maintained through densification into a type V gel-silica. The advantages of the silica Fresnel lens over a polymer lens is the very low thermal expansion coefficient and the thermal and radiation stability of the silica compared to a polymer.

15.4.5. Porous Type VI Gel-Silica and Applications

The extremely small scale of interconnected porosity in organometallic derived gel-silica results in optical transparency to UV wavelengths as far as 250 nm. The transparent porous structure can be impregnated with a second phase thereby achieving an optical composite. Examples of optical polymers that have been put into type VI silica (porous Gelsil™) are shown in Table 15.4. Results
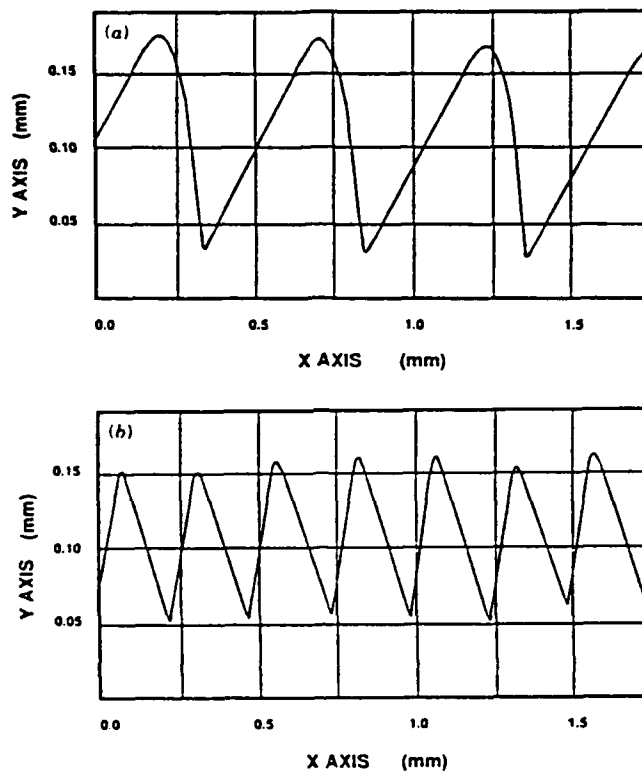
Figure 15.14. Profilometry graphs of Fresnel lenses: (a) polymer master. (b) replication in organometallic gel-silica.

Figure 15.15. Microscope photograph of a dry organometallic gel-silica Fresnel lens.

24

TABLE 15.4. Optical Composite Made from Type VI Silica (Porous Gelsil™)

Non-linear Optical Polymers

Phenylenebenzobisthiazole
2-Methyl-4-nitroaniline

Organic Fluors

2-(4′-t-Butylphenyl)-5-(4″-biphenylyl)-1,3,4-oxadiazole
p-Terphenyl
p-Quaterphenyl

Wavelength Shifter

3-Hydroxyflavone

Other Organics

Laser dyes
Liquid crystals

from some of these studies have been discussed elsewhere [3, 11]. The colloidal-based silica processing produces gels with large pore size that are not optically transparent and therefore cannot be used to make type VI optical silica.

Another unique application of the type VI structure is to use it as the substrate for laser densification. Optical waveguides have been made using laser writing of higher-density tracks on the porous gel–silica substrate [12]. The higher-density tracks have a greater index of refraction than the porous matrix and therefore can serve as a planar waveguide. The prime advantage of the laser-written waveguide is that it matches the index of refraction of silica fiber optics, which is not the case for ion-exchanged or diffusion-based waveguides.

15.5. CONCLUSIONS

Since the first Ultrastructure Processing Conference, the progress made in sol–gel science allowed the development of two new types of optical silica. A fully dense sol–gel-derived silica, termed *type V gel–silica*, can be made either with a colloidal process or an organometallic process. The colloidal method results in optically opaque gels to large pores of >200 nm in diameter with ⩾80% porosity requiring 1500 to 1720°C densification temperatures. The organometallic process results in optically transparent gels with 45% pores of only 2.5 nm in diameter and require a densification temperature of only 1150°C. An optically transparent sol–gel-derived porous silica, termed *type VI gel–silica*, can be made by the organometallic route. This new type of silica can be used for applications such as an optical element with a second phase impregnated within the pores or as a substrate for laser-written waveguides.

The major progress was made in size scaleup. This was achieved by (1) developing an understanding of the chemical mechanisms involved in each of the seven sol–gel–glass processing steps and (2) establishing careful process controls for each processing step. It is the precise control over the chemical mechanisms and rates of reactions that allows the production of optics of 75 and 100 mm in diameter or larger for both type V and type VI silicas, respectively.

The physical properties of the organometallic-derived type V gel–silica are equal or superior to types I to IV optical silicas and include short UV cutoff, low optical absorption throughout the spectrum, high homogeneity, very few defects, low strain birefringence, and low coefficient of thermal expansion.

Both the colloidal and the organometallic methods of optical gel–silica manufacture can be used to produce complex net shapes by direct casting at ambient temperature. This unique property of the sol–gel process can be used to make optics with special shapes and surface features, such as lightweight mirrors, Fresnel lenses, and aspheric optical components.

ACKNOWLEDGMENTS

REFERENCES

1. J. D. Mackenzie, in: L. L. Hench and D. R. Ulrich, Eds., *Ultrastructure Processing of Ceramics, Glasses, and Composites*, p. 15, Wiley, New York (1984).
2. M. Grayson, Ed., *Encyclopedia of Glass, Ceramics, Clays and Cement*, Wiley, New York (1985).
3. L. L. Hench, S. H. Wang, and J. L. Nogues, *SPIE Proc.*, 878, 76 (1988).
4. S. H. Wang, C. Campbell, and L. L. Hench, in: J. D. Mackenzie and D. R. Ulrich, Eds., *Ultrastructure Processing of Advanced Ceramics*, p. 145, Wiley, New York (1988).
5. L. L. Hench, G. Orcel, and J. L. Nogues, in: C. J. Brinker, D. E. Clark, and D. R. Ulrich, Eds., *Better Ceramics Through Chemistry, Mater. Res. Soc. Symp. Proc.*, 73 (1986).
6. R. D. Shoup, in: J. D. Mackenzie and D. R. Ulrich, Eds., *Ultrastructure Processing of Advanced Ceramics*, p. 347, Wiley, New York (1988).
7. W. Vasconcelos and L. L. Hench, in: *Proceedings 4th Ultrastructure Processing Conference*, Tucson, AZ, February 1989.
8. G. Orcel, J. Phalippou, and L. L. Hench, *J. Non-Cryst. Solids*, 88 114 (1986).
9. J. K. West, personal communication, 1987.
10. L. L. Hench and S. H. Wang, *Phase Transitions*, 24–26, 785 (1990).
11. J. L. Nogues, S. Majewsi, J. K. Walker, M. Bowen, R. Wojcik, and W. V. Moreshead, *J. Am. Ceram. Soc.*, 71, 1159 (1988).
12. R. V. Ramaswamy, T. Chia, R. Srivastava, A. Miliou, and J. K. West, *SPIE Proc.*, 878, 86 (1988).

22

b. REAL TIME MONITORING OF SILICA GEL DRYING BEHAVIOR

M. J. R. WILSON AND L. L. HENCH

22.1. INTRODUCTION

One of the main difficulties in monitoring changes during the drying of gels is that the "as formed" gel is extremely sensitive to physical contact. Any device contacting the gel may affect drying behavior by altering the surface temperature, causing inhomogeneous evaporation and development of differential stresses that can lead to cracking.

In this apparatus, optical means are used to measure changes in thickness and diameter of a gel and the stresses that develop during drying. Weight change is measured simultaneously enabling density and pore volume to be calculated.

The gel is suspended within a drying chamber contained within an oven. Both the drying chamber and the oven are equipped with windows to provide 360° viewing of the sample. The windows allow transmission of polarized light through the sample and also side illumination. An automatic 35-mm camera is used to record the dimensions of the gel (by careful use of mirrors) and the balance readout at any time interval, from 1 sec to 120 hr. An automatic data collection system records temperature at up to eight locations within the drying chamber in order to confirm temperature homogeneity. Temperature control is provided by means of a (Micristar) ramp and soak controller.

247

22.2. EXPERIMENTAL APPARATUS

The apparatus is shown in detail in Fig. 22.1. Evaporation rate is controlled by both temperature and by two vapor outlets, one of which is variable. Details are shown in the inset of Fig. 22.1. The camera records the sample dimensions on high-resolution 35-mm slides that afford a four- to five-times magnification of the sample.
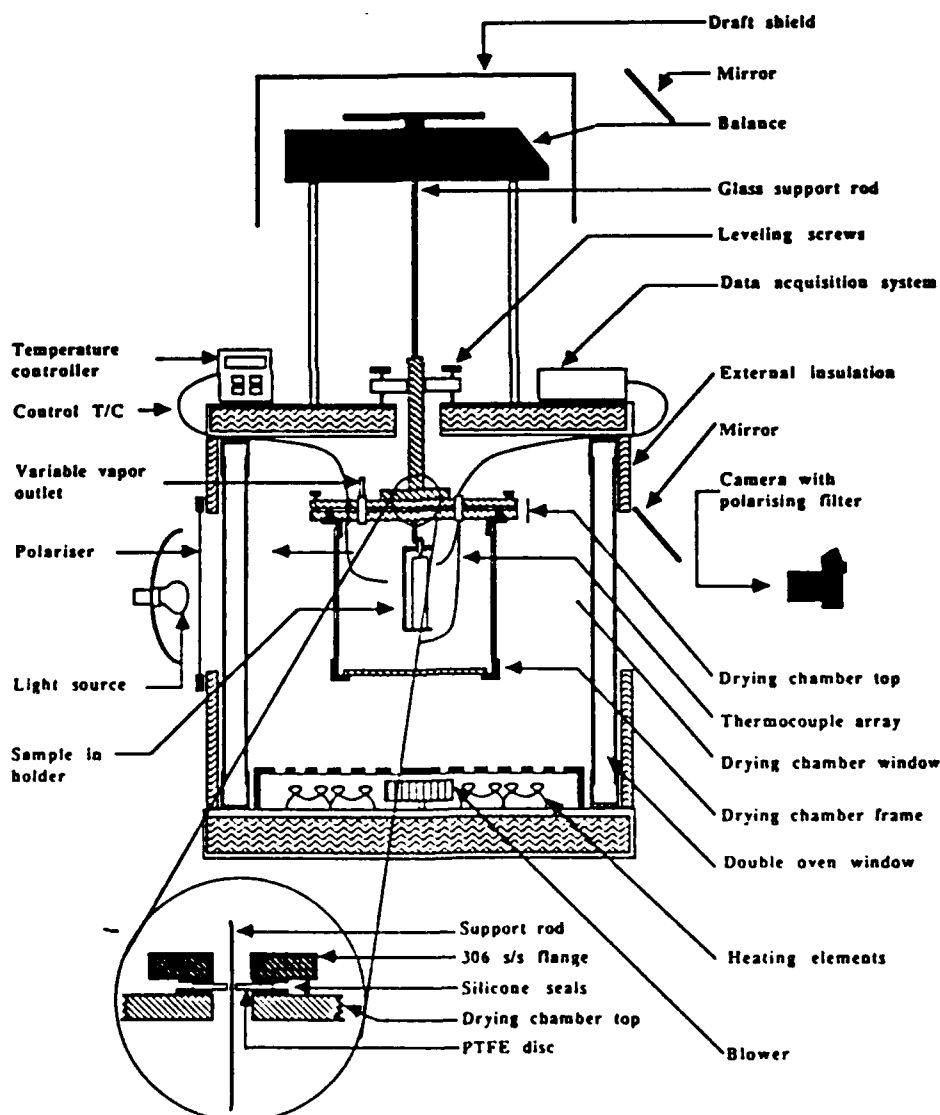

Figure 22.1. Experimental apparatus for real-time monitoring of silica gel drying behavior.

The gels 22 and 25 used in this study were made by adding 1 mol of tetramethyloxysilane to 16.17 mol of water containing 0.089 mol of nitric acid at pH ~ 1.5. After stirring for 10 min, the resulting sol was chilled to 20°C and cast into a 110-mm-diameter polymethylpentene mold. Gelation occurred in 55 hr at 23°C and was followed by aging for 3 months at 22°–25°C. The aged gel was removed from its mold and placed on edge on the sample holder. The drying chamber was sealed and the wet weight recorded. The drying chamber was heated to 110°C at a rate of 5°C/hr. The gel was maintained at 110°C ± 0.5°C until no further changes in weight or dimension occurred, this was about 135 hr for gel 25.

22.3. RESULTS

The data collected are weight, diameter, thickness, birefringence, transparency (or opacity), and temperature. These data are shown in Fig. 22.2 for a 99.3-mm-diameter, 21.2-mm-thick silica gel monolith (gel 25) with an initial density of 1.077 g. The sequence of photographs (1 to 10) in Fig. 22.2a show the appearance of the gel at points marked on Fig. 22.2. Figure 22.3 shows the equivalent data for a similar monolith 99.4 mm in diameter and 19.4 mm thick with an initial density of 1.080 g/cm^2 (gel 22).

The pore volume can be calculated by

$$V_p = V_b - V_s$$

where V_b is the bulk volume, calculated from the sample thickness and diameter, and V_s is the volume of the network, calculated from knowledge of the amount of SiO$_2$ in the sample (from the amount of alkoxide used) and assuming a structural density of 2.11 g/cm^3 for the acid-catalyzed gels used (Chapter 11). The time dependence of the pore volume is shown for gel 25 in Fig. 22.4c. The change in the rate of weight loss and density is shown in Figs. 22.4a and 22.4b. Figure 22.5 shows the comparative (log) loss rates for both samples. During the rise in temperature the gel expands slightly up to ~ 70°C after which evaporative losses begin to dominate and the gel rapidly loses both weight and volume (stage 1). This first stage of drying accounts for over 80% of the total weight loss and almost 100% of the total volume loss while taking only 30% of the total drying time. The end of this stage coincides with the maximum observed density of 1.48 g/cm^3. This value corresponds to the calculated density of the dry gel with the pores completely full of pore liquid.

After shrinkage stops, the rate of evaporation slows and assumes a linear relationship with time (Fig. 22.4a). This stage (stage 2) accounts for 11% of the total weight loss and about 35% of the total drying time. Shortly after entering this stage the gel turns opaque (photographs 5 to 10), first at the edges, progressing linearly toward the center. It is normally during this opaque stage that the gel breaks, if sufficient stress or defects are present (Chapter 15). Some

(a)

(b)
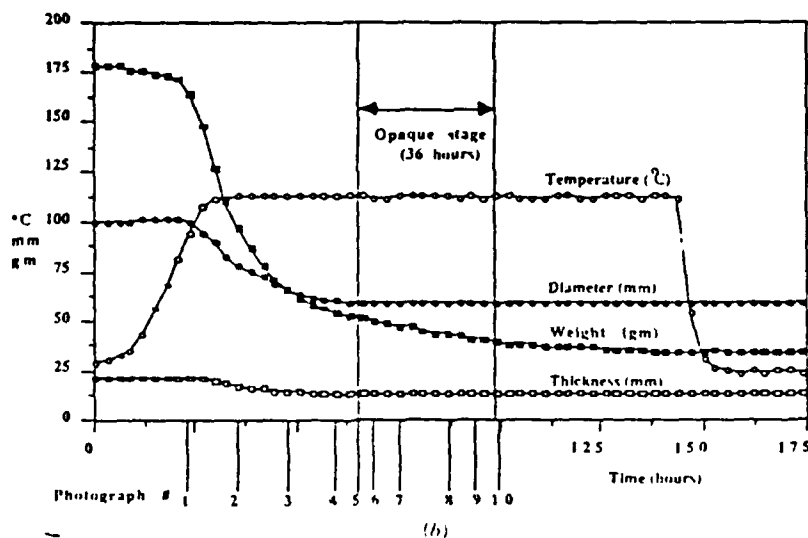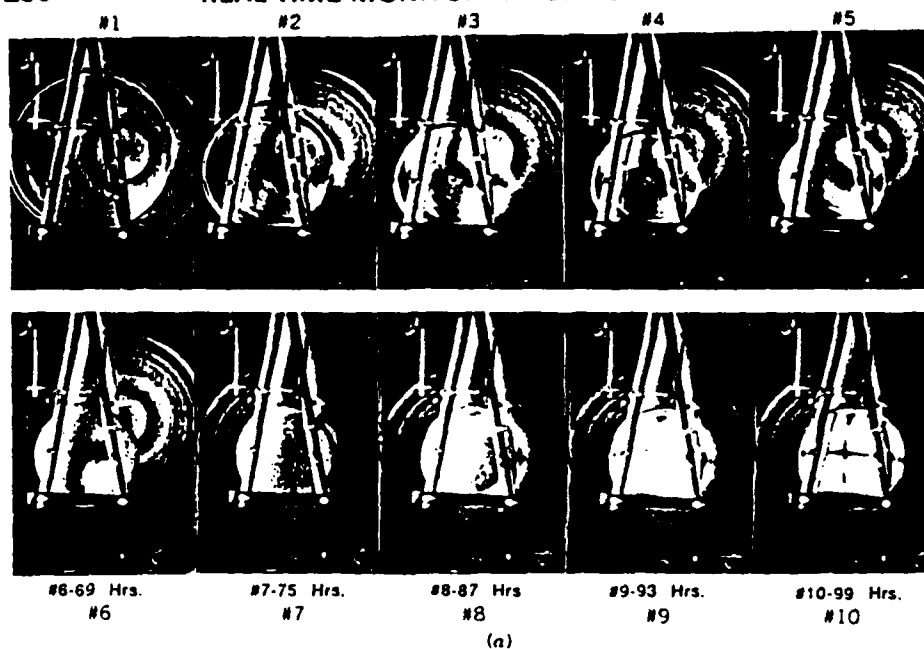
Figure 22.2. Drying behavior of silica gel as a function of time (gel 25).

further shrinkage ($\sim 1\%$ linear) is observed during this stage, although the gel subsequently expands to its previous size as transparency is regained. At the end of this stage, the gel is within 5%, of the theoretical weight of silica formed in the original hydrolysis and subsequent polycondensation. Further soaking at $110°C$ reduces the weight to within 2.2%, of the theoretical value, but at a very reduced rate. This final stage (stage 3), leading to equilibrium, accounts for the remaining
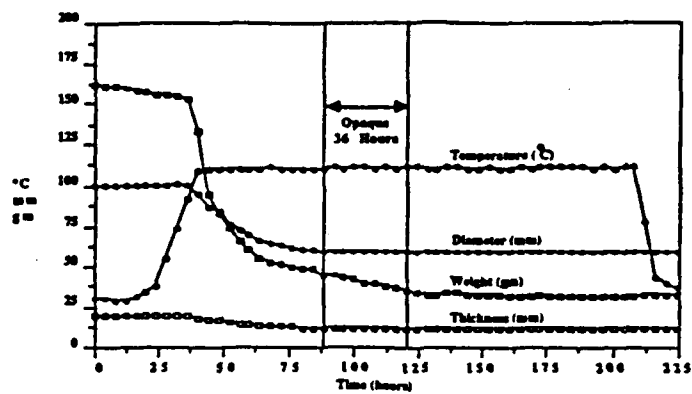
Figure 22.3. Drying behavior of silica gel as a function of time (gel 22).
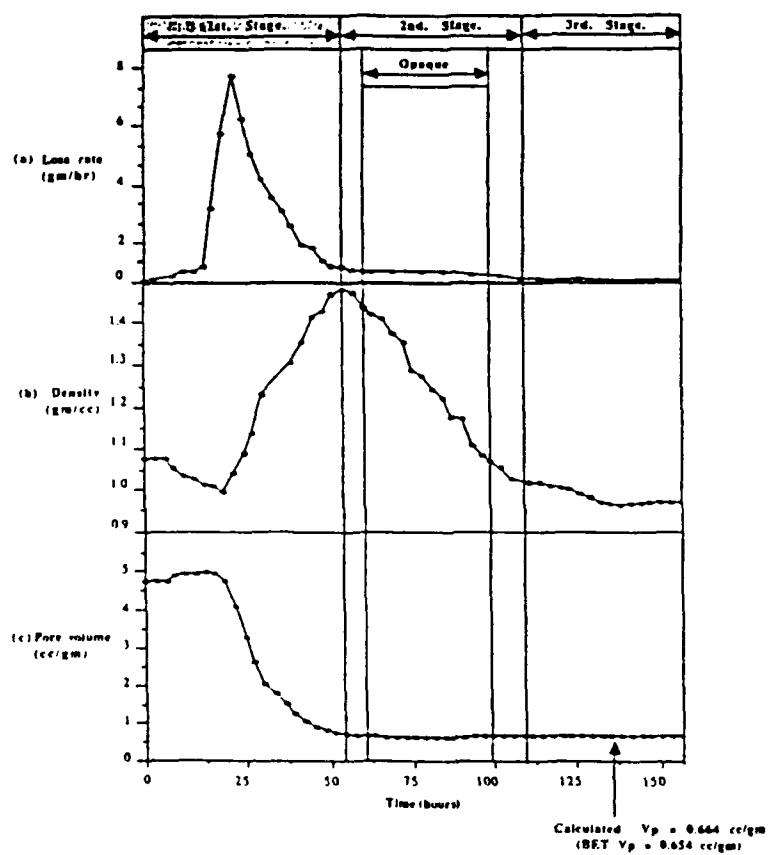
Figure 22.4. Time dependence of (a) rate of weight loss (b) density and (c) pore volume for gel 25.

251

31
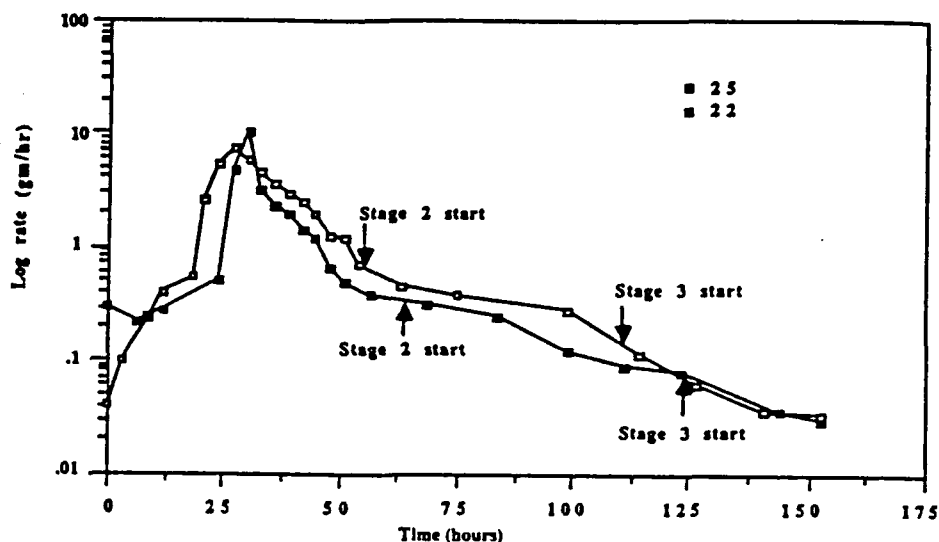
Figure 22.5. Comparative (log) loss rates for gel 22 and gel 25.

drying time. The aged gel consists, by volume, of 91% pore liquid (35% methanol/65% water at pH ~1.5) and 9% solid phase. The 110°C dry gel, in contrast, consists of 42% solid phase, 57% open porosity, and 1% adsorbed moisture. The Brunaur–Emmett–Teller data give an average pore radius of 23.1 Å, a surface area of 566 m^2, and a pore volume of 0.654 cm^2/g for gel 25, compared to a pore radius of 23.8 Å, a surface area of 581 m^2, and a pore volume of 0.692 cm^3 for gel 22.

22.4. DISCUSSION

The drying process consists of three stages:

Stage 1. During which the greatest changes in volume weight and structure occur.

Stage 2. In which changes in weight and volume are small, but large changes in optical characteristics are seen.

Stage 3. In which there are no further dimensional changes, but there is a progressive loss of weight to the minimum attainable value.

The physical changes that occur during these stages are shown in Fig. 22.4. In stage 1, the rise in temperature is accompanied by the rapid increase in the loss rate seen in Fig. 22.4a and Fig. 22.5. The rise in temperature is also responsible for the small increase in pore volume seen in Fig. 22.4c due to thermal expansion

of the enclosed pore liquid. The drop in density seen in Fig. 22.4b can only be partially attributed to this expansion. The minimum density observed occurs slightly before the peak loss rate. The volume loss does not equal the volume of evaporated pore liquid, but follows closely behind suggesting that the evaporation rate is greater than the maximum strain rate of the gel and that pore emptying is occurring. As the evaporative forces begin to dominate, the gel begins to shrink rapidly, resulting in an increased packing density of the solid phase, further polycondensation (formation of new Si–O bonds) and a rise in density, modulus, and viscosity of the solid phase. The shrinkage is accompanied by a nonlinear decrease in the loss rate, which may be due to decreasing surface area and pore radius. This structural change would create a dry surface layer through which vapor must diffuse to reach the surface. A decrease in the strain rate of the gel or a combination of these factors may also be involved in producing the observed rates. The maximum density corresponds to the point at which shrinkage stops and the meniscus is at the surface. This is the point where the resistance to shrinkage becomes greater than the applied stress, and the meniscus penetrates the interior of the gel. This marks the beginning of stage 2. Once this occurs the loss rate progressively slows as the liquid vapor interface moves toward the center. The opacity seen during stage 2 is due to this interface. Shaw [1] suggests that this phenomenon is caused by light scattering from isolated pores (or groups of pores) of such a dimension that they are able to scatter light. The data obtained during stage 2 indicate an increase in open porosity from 0.012 to 0.364 cm^3/g during the opaque transition, thus supporting Shaw's scattering theory. The start of stage 3 occurs when the loss rate again drops. The division between stages 2 and 3 is not as well defined as that between 1 and 2, but can be seen clearly in Fig. 22.5.

A small level of stress birefringence appears to be present throughout the whole process. However during stage 1 the position and motion of the stress generated isogyres is difficult to monitor. During the opaque stage the birefringence is obscured by the scattering. On completing the opaque stage the stress birefringence becomes sufficiently strong to lead to the formation of the biaxial optical figure of the two curved isogyres and the Maltese cross optical figure seen in Fig. 22.2a(8–10). For further analysis of this stress birefringence data see Ref. 4.

The presence of differing drying rates for silica gels has been noted by Zarzycki [3], although long drying times (~400 hr) were required to preserve monolithicity. Dwivedi [4] reported that the water loss during drying of alumina gels takes place in two stages, although cracking occurred during the drying process. The detailed drying data presented herein on uncracked monoliths shows three identifiable stages of drying. These three stages are consistent with the constant rate period (stage 1), the first falling rate period (stage 2), and second rate period (stage 3), discussed by Scherer and Brinker [5]. For further discussion of the differences between stage 1, as determined herein and the constant rate period, see Ref. 2.

22.5. CONCLUSIONS

The apparatus described is capable of accurately monitoring the physical and optical changes that occur while drying large monolithic gels. The data show that the drying process consists of three distinct phases.

Stage 1. Initial gel expansion is followed by rapid loss of weight and volume.

Stage 2. When shrinkage ceases, the gel turns opaque to transmitted light and undergoes a small and temporary reduction in volume. During this second stage the rate of weight loss becomes linear.

Stage 3. The rate of loss falls to a lower value. The third stage takes considerable time, but results in a gel within ~2% of theoretical dry weight at 110°C.

ACKNOWLEDGMENT

REFERENCES

1. T. M. Shaw, in: *Better Ceramics Through Chemistry, Mat. Res. Soc. Symp. Proc.*, 73 (1986), 215.

2. M. J. R. Wilson, Drying Kinetics of Pure Silica Xerogels, Master Thesis, University of Florida (1989).

3. J. Zarzycki, in: *Ultrastructure Processing of Ceramics, Glasses, and Composites*, p. 27, Wiley, New York (1984).

4. R. K. Dwivedi, *J. Mater. Sci. Lett.*, 5, 373 (1986).

5. G. W. Scherer and C. J. Brinker, *Sol-Gel Science*, Academic Press, New York, 1989.

31

c. SCL-GEL-DERIVED TITANIA-SILICA GEL-GLASSES

YEU-CHYI CHENG AND LARRY L. HENCH

31.1. INTRODUCTION

TiO_2-SiO_2 glasses are of significant technical importance due to their unusual thermal expansion behavior. The linear thermal expansion coefficient decreases with increasing titania content, with zero expansion in the range of 7–8 wt% TiO_2 [1, 2]. Conventionally, the titania-doped silica glasses, produced either by melting or by flame hydrolysis, are difficult to prepare as large, transparent, homogeneous single-phase materials. Recently, the sol-gel technique has been successfully used to prepare glasses at a relatively lower temperature. Yoldas [3] and Kamiya and Sakka [4, 5] have shown that it is possible to prepare titania-silica glasses through this route, which involves hydrolyzing liquid metal alkoxides and subsequently heating the gel to produce a vitreous glass.

It is concluded from X-ray diffraction [6] and infrared analysis [7, 8] that the titanium ions are in tetrahedral coordination in the TiO_2-SiO_2 glass system with up to 10.5 wt% TiO_2. Also, these glasses are built up of a homogeneous network in which each TiO_4 tetrahedron is linked to four SiO_4 tetrahedra.

The objectives of this investigation are (1) to study the effect of atmosphere on the densification of the TiO_2-SiO_2 monoliths, (2) to determine the physical properties as a function of densification temperature, and (3) to investigate the effect of densification on the coordination of titanium ions in the monolith throughout densification using Fourier transform infrared spectroscopy.

333
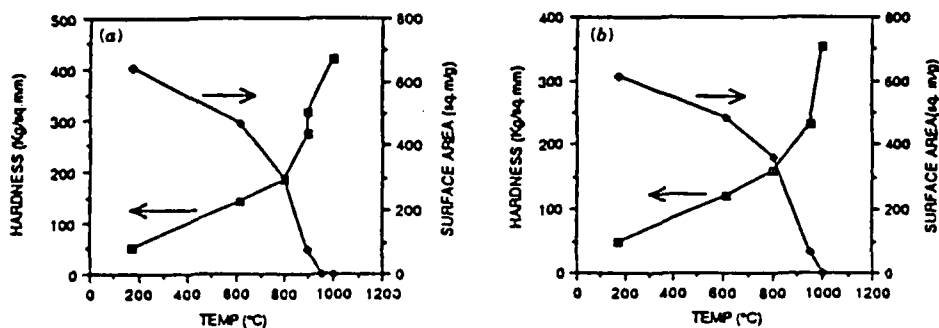
Figure 31.4. The effect of processing temperature on the hardness and surface area of titania-silica gel-glasses (a) $3\%TiO_2$ (b) $7\%TiO_2$.

Figures 31.4 and 31.5 illustrate the effect of processing temperature on the physical properties of titania-silica gel-glasses when sintered in flowing dry air. The change of linear dimension, weight loss, and skeletal density as a function of temperature for 5% titania-silica gel-glass is shown in Fig. 31.6.

31.4. DISCUSSION

All the physical properties determined in this study, that is, microhardness, specific surface area, pore radius, pore volume, and bulk density, show no significant changes below $600°C$ regardless of TiO_2 content. Above $600°C$, these properties change rapidly with temperature. However, there is about 6% shrinkage when the dried titania-silica gels are heated to $600°C$ for all the compositions studied. Gel shrinkage can be attributed to four mechanisms: (1) capillary contraction, (2) condensation-polymerization, (3) structural relaxat-
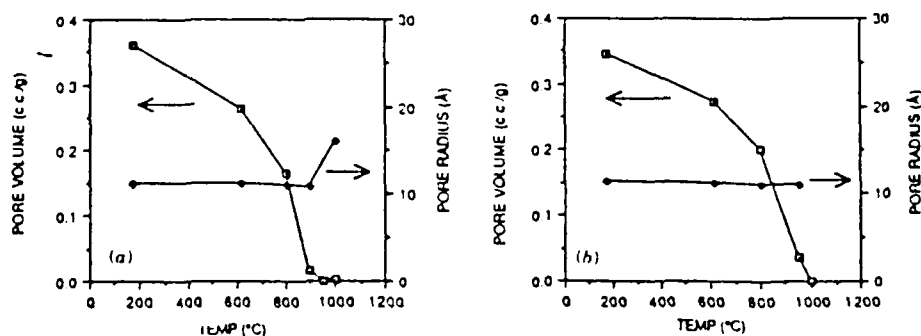
Figure 31.5. The effect of processing temperature on the pore volume and pore radius of titania-silica gel-glasses (a) $3\%TiO_2$ (b) $7\%TiO_2$
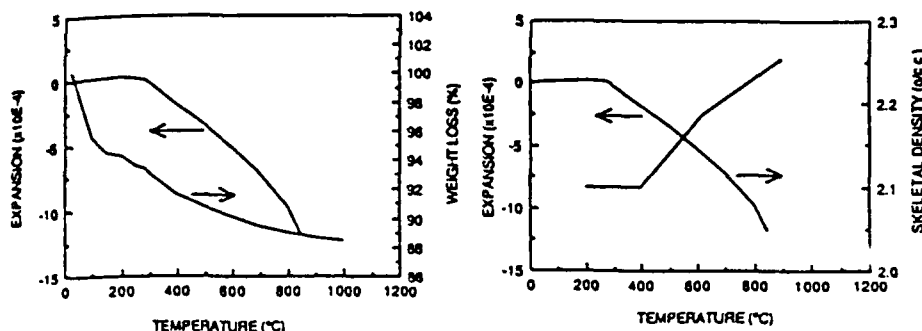
Figure 31.6. The change of linear dimension, weight loss and skeletal density as a function of temperature for a 5% titania-silica gel-glass.

ion, and (4) viscous sintering [11]. Below 400°C, the skeletal density of the gels is essentially constant (see Fig. 31.2) with 10% weight loss in this temperature regime as indicated by thermogravimetricanalysis results (see Fig. 31.6). This weight loss is attributed to the desorption of water molecules and pyrolysis of the gels. Thus, shrinkage in this temperature range is attributed to condensation reactions, $Si-OH + HO-Si \rightarrow Si-O-Si + H_2O$, which result in a more rigid network and increases the bulk density and microhardness.

At higher temperature (<600°C), structural rearrangement or structural relaxation takes place due to available thermal energy, which results in the decrease of the excess free volume. This is confirmed by the increase of the skeletal density as shown in Fig. 31.2. Thus, both condensation and structural relaxation contribute to the shrinkage observed. In addition, the network structure is further strengthened as indicated in Fig. 31.3. The infrared peak at $1050 \, cm^{-1}$, attributed to the antisymmetric Si-O stretching mode within the SiO_4 tetrahedra, and the peak at $460 \, cm^{-1}$, attributed to the bending mode of O-Si-O within tetrahedra and Si-O-Si between tetrahedra, are shifted toward higher wavenumbers, suggesting higher force constant for the vibrations. The vibrational band associated with TiO_4 tetrahedra is obtained at $945 \, cm^{-1}$, as reported in the literature [8, 9].

It is observed that gels sintered under ambient static atmosphere all bloated at a temperature above 800°C. On the other hand, sintering conducted under a dried air atmosphere showed no sign of bloating at a temperature of 1000°C. This is presumed to be due to the lower water content of gels sintered in dried air atmosphere. Densification of silica glass increases with increasing OH content [12]. Consequently, densification starts earlier for gels with higher water content, as in the case of static ambient atmosphere, and bloating is observed, because pores are closed before water can be thermally desorbed.

There is no question that gels with higher titania content are more difficult to sinter. Because the size of the Ti^{4+} ion is larger than that of Si^{4+}, it is expected that as Ti^{4+} enters the glass network, both bond angle and bond length are

affected. Greegor et al. [13] and Morikawa et al. [14] have shown a Ti-O-Si bond angle of 159° and a Ti-O distance of 1.80 to 1.86 Å compared to the 152° Si-O-Si bond angle and 1.6-Å Si-O bond distance. Thus, the network structure "opens up" upon titania addition. The increase in densification of the TiO_2-SiO_2 glasses thus may be attributed to the introduction of more easily deformed Ti-O-Si bonds, which increase the ease of structural rearrangement.

31.5. CONCLUSIONS

Large, monolithic TiO_2-SiO_2 gel-glasses were produced using organometallic sol-gel technology. The physical properties of the gel-glasses do not change significantly below 600°C in either an ambient static or controlled dried air atmosphere. Above 600°C, the properties change rapidly with densification temperature. Bloating of the samples was observed when sintering was carried out in ambient static, but not in controlled dried air atmosphere. This was attributed to the difference in the water content of the samples, which resulted in the difference in densification rates. The network structure is strengthened as densification temperature increases, as indicated by the increase in the wavenumbers of infrared vibration peak. The vibrational band associated with TiO_4 tetrahedra is obtained at 945 cm^{-1}. The increase in densification with increasing titania concentration is explained in terms of the weaker nature of the Ti-O-Si bond, increasing the ease of structural rearrangement as titania content increases.

ACKNOWLEDGMENT

REFERENCES

1. P. C. Schultz and H. T. Smyth, *Amorphous Materials*, Wiley, New York (1972).
2. P. C. Schultz, *J. Am. Ceramic Soc.*, 59, 214 (1976).
3. B. E. Yoldas, *J. Non-Cryst. Solids*, 38-39, 81 (1980).
4. K. Kamiya and S. Sakka, *J. Mater. Sci.*, 15, 2937 (1980).
5. K. Kamiya and S. Sakka, *J. Non-Cryst. Solids*, 32, 357 (1982).
6. D. L. Evans, *J. Am. Ceramic Soc.*, 53, 418 (1970).
7. K. Kusabiraki, *J. Non-Cryst. Solids*, 79, 208 (1986).
8. H. R. Chandrasekhar and M. Chandrasekhar, *Solid State Comm.*, 31, 329 (1979).
9. Y. C. Cheng and L. L. Hench, presented at the MRS spring meeting, Reno, Nev., April 5-9, 1988.
10. S. Wallace and L. L. Hench, in: L. L. Hench and D. R. Ulrich, Eds., *Science of Ceramic Chemical Processing* p. 148, Wiley, New York (1986)

11. C. J. Brinker and G. W. Scherer, *J. Non-Cryst. Solids*, **70**, 301 (1985).

12. J. Arndt, *J. Am. Chem. Soc.*, **52**, 285 (1969).

13. R. B. Greegor, F. W. Lytle, D. R. Sandstrom, J. Wong, and P. Schultz, *J. Non-Cryst. Solids*, **55**, 27 (1983).

14. H. Morikawa, T. Osuka, F. Marumo, A. Yasumori, and M. Yamane, *J. Non-Cryst. Solids*, **82**, 97 (1986).

SECTION IV

PROJECT B:
Sol-Gel Glass Applications

a. OPTICAL COMPOSITES

L. L. Hench, Advanced Materials Research Center, University of Florida, One Progress Blvd., #14, Alachua, FL 32615

Two methods are described for preparation of optical composites: (A) a sol method where an organic phase is mixed with an inorganic precursor and (B) where an optical transparent inorganic Type VI gel-silica matrix is first prepared and stabilized thermally, then an optically active polymer is impregnated into the interconnected 3-D pore network. Comparisons of relative processing merits, mechanical properties and optical applications are presented with emphasis on solid state tunable dye lasers.

INTRODUCTION

For centuries optical components have been primarily single phase materials with or without chemical dopants to produce specific optical characteristics. Examples include glasses and single crystals for lenses, mirrors, lasers, filters; polycrystalline ceramics for optoelectronics; and glass-ceramics for mirrors.[1] During the last few years the use of sol-gel chemical processing has made it possible to develop optical composites which have two or more phases, and thereby possess unique optical properties. The composites are usually an optically active organic phase and a sol-gel derived oxide matrix. Because of the chemical stability of an oxide network such optical composites offer substantial advantages in processing, reliability, and performance over the organics by themselves. Many of the organics of interest are liquid at ambient temperature and are therefore restricted in use in an optical system. By using the composites approach these restrictions are circumvented.

Several groups have pioneered the growing interest in optical composites including Reisfeld, Avnir and colleagues in Israel;[2,3,4] Mackenzie[5] and Dunn[6] and co-workers at UCLA; King and colleagues at the University of Manchester, U.K.;[7], Prasad and Karasz at SUNY at Buffalo and University of Massachusetts[8] and Nogues and co-workers at the University of Florida and Geltech, Inc.[9] Their developments will be reviewed as examples of this new field along with recent results from our laboratory.[10]

PROCESSING

Two alternative pathways are used in making optical composites, as illustrated in Figure 1. In Method A, termed *sol processing*, the metal organic sol-gel precursor is mixed with the optical organic molecules. Hydrolysis and polycondensation reactions occur in Process Steps 1-3, see References 11 and 12 for details, which results in formation of a highly porous, interconnected 3-D oxide network, the gel, containing the organic within the framework of the gel. Removal of the alcohol-water liquid from the pores of

OPTICAL COMPOSITES PROCESSING

Process Step		METHOD A (Sol Processing)	METHOD B (Adsorption or Impregnation Processing)	
1	25°C < 1 Hr	Mixing (Hydrolysis & Condensation)	Mixing (Hydrolysis & Condensation)	Produces colloidal suspension (sol). Used for films, coatings.
2	25°C < 1 Hr	Casting	Casting	Sol cast into inexpensive molds of desired product shape/surface replication.
3	25°C Minutes - > 48 Hrs	Gelation (Polycondensation)	Gelation (Polycondensation)	Sol solidifies by cross linking of fundamental particles.
4	< 100°C 12 - 48 Hrs	Aging (Syneresis)	Aging (Syneresis)	Structural evolution of the gel by polycondenstation, dissolution and redeposition.
5	100 - > 180°C 24 - 72 Hrs	Drying	Drying	Removal of the gel liquid phase.
			Stabilization (Dehydration)	Removes any remaining surface species without significant structural alteration. (Type VI gel-silica)
6	180 - > 950°C 12 - 72 Hrs		Porous Matrix (Type VI Gel-Silica)	
7			Adsorb or Impregnate Optical Organic	
8			Drying	
		OPTICAL COMPOSITE	OPTICAL COMPOSITE	

Figure 1. Process steps for two methods of making optical composites.

the gel, Step 5, produces a dry and moderately strong two phase material. The size and volume fraction of pores containing the organic phase are influenced greatly by the amount of water or alcohol used in making the gel and the pH of the solution. The mechanical and chemical behavior of a composite made in this manner is restricted by the temperature limitation of drying imposed by the thermal stability of the optical polymer. Figure 2 illustrates the range of microhardness, flexural and diametral tensile strength, and hydroxyl content of silica gel monoliths dried at 180°C. The improvement

Advanced Composite Materials
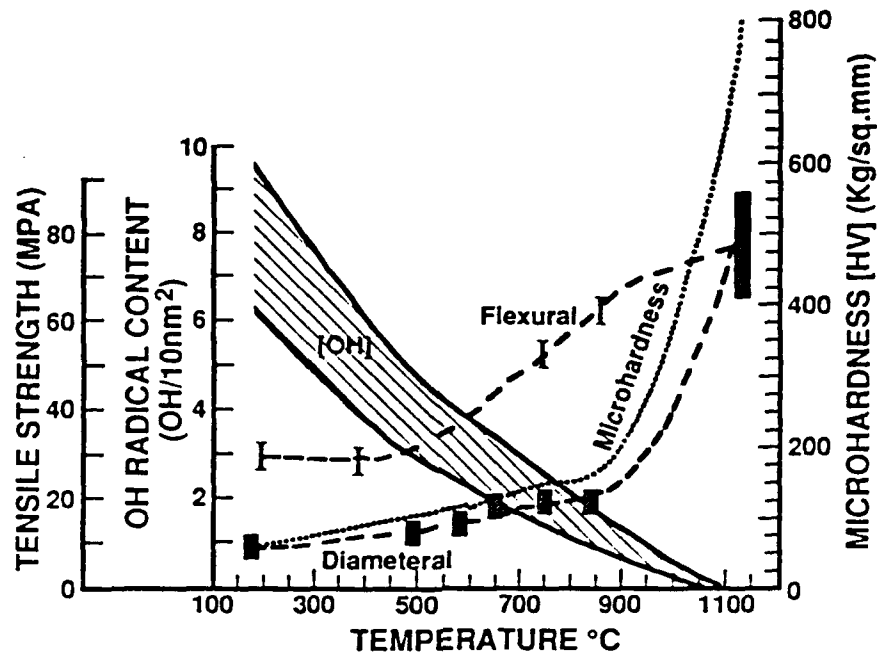
Figure 2. Effect of stabilization temperature on properties of Type VI gel-silica optical matrices with 1.2 nm pores OH content, ref.: flexural strength (MPa), ref.: diametral tensile strength (MPa), ref.; Microhardness (Kg/mm^2), ref. X = flexural strength for fully dense vitreous silica, ref.

in mechanical properties with increased processing temperature is also illustrated in Figure 2.

Method B is a two part process, termed *absorption or impregnation processing,* which circumvents the thermal stability limitation on processing. The first part, Steps 1-6, uses the sol-gel method to make an optically transparent gel-silica matrix with a very large volume fraction of interconnected porosity with a very small average pore radius (<10nm). This type of material is termed Type VI gel-silica. (For a discussion of Type I-IV silicas see Bruckner,[13] for a description of the processing of Types V and VI gel-silica see references 11 and 14.) The Type VI matrix is chemically stabilized by a thermal treatment, see Figure 1, Step 6, and then ground or polished, if necessary, to produce an optical element. In the second part, Steps 7 and 8, the optical organic phase is diffused or impregnated into the porous matrix where it is chemically or physically absorbed within the pore network. The extent of chemical interaction between the optical organic phase and the network is strongly influenced by the stabilization treatment which controls the silanol concentration on the surface of the pores.[15,16] Figure 3 illustrates two variations in the pore geometry, silanol concentrations, adsorbed

Figure 3. Schematics of: (a) Surface silanols with adsorbed water molecules forming bound water layer, (b) Small pore (1.2 nm) diameter gel-silica matrix with 0.7 nm thick bound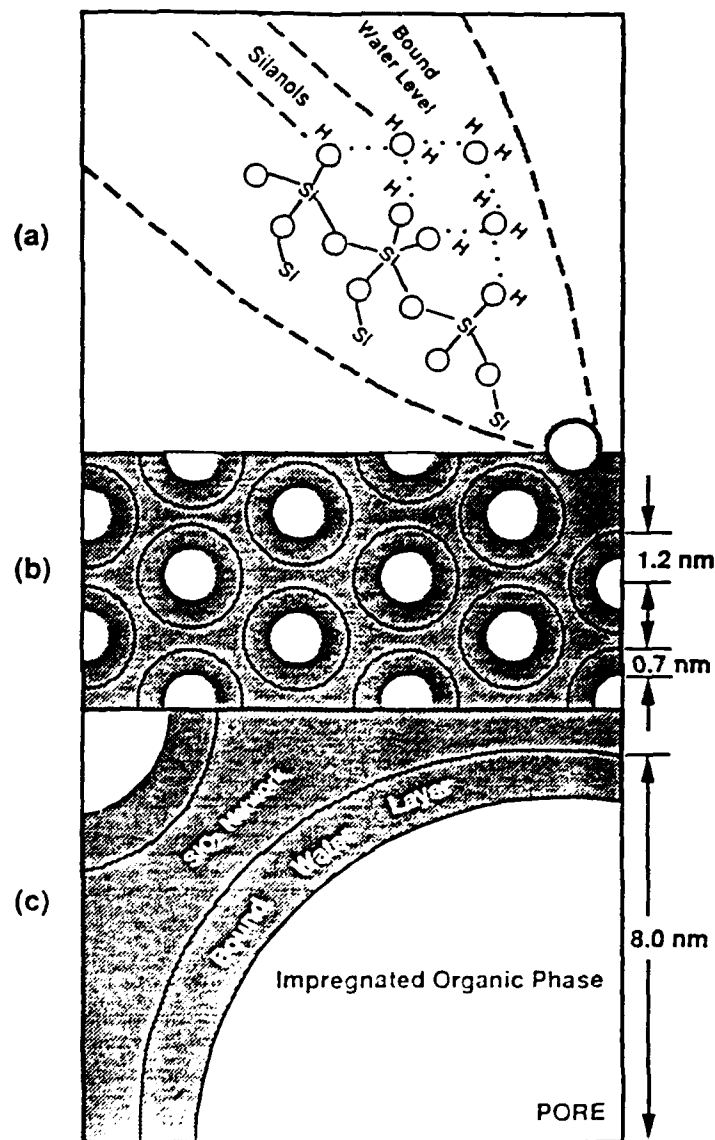 water layer, (c) Large pore (8.0 nm) gel-silica matrix with 1.2 nm thick bound water layer. Note large difference in volume available for impregnated organic molecules.

4.4

and bound water layers, and sorbed organic molecules that are possible using Method B processing of optical composites. Thickness of the bound-water layer varies from 0.7 to 1.2 nm as pore radius increases from 1.2 to 7.5 nm, References 11 and 16.

There are advantages and disadvantages of both process options. The primary advantage of Method A is its simplicity. There is relatively little information on the mechanical, and thermal properties of composites made by Method A. Likewise data on ultrastructural or textural characterization of composites made by Method A is limited.

The primary advantages of optical composites made by Method B, Table 1, is that the textural properties such as volume fraction and pore size distribution can be tailored for specific applications. Also, the chemical nature of the pore network, largely controlled by pore radius, silanol concentration, and absorbed water layers can be varied during stabilization, Step 6, and optimized for a particular organic impregnate. For example, Nikiel, et al. have shown[17] that the rotational relaxation times for acetonitrile in a Type VI gel-silica matrix is an order of magnitude larger when the molecules are adsorbed in the first monolayer compared with molecules that completely fill the pores. Perry and Li[18a] and Hench and West[1] and Wang[18b] have shown that the extent of pore surface hydration affects the ligand fields of elements adsorbed in the pores.

Table 1
Advantages of Type VI Gel-Silica as a Laser Dye Host

1) Fabricability into laser rods, slabs, or Brewster angle segments	2) Wide range of volume fraction of porosity
3) Polishability	4) Wide range of pore sizes
5) High mechanical strength	6) High thermal stability
7) Net shape and net surface casting	8) High chemical stability
9) High purity	10) Excellent transmission over wide range of wavelengths
11) Ability to tailor chemically the surface to control the dye-matrix interface	

PROPERTIES OF TYPE VI GEL-SILICA OPTICAL MATRIX

Some textural characteristics of the optical matrices made by Method B are summarized in Figure 4. Average pore radii, calculated from N_2 adsorption isotherms, vary from 1.2 nm to 8 nm. The smaller pore size range is made using acidic conditions to control hydrolysis and condensation, Step 1, whereas the larger pore sizes are produced by also using HF in Step 1 or aging in basic conditions, Step 4. The volume fraction of porosity varies from 0.3 to 0.75 depending upon the initial sol chemistry; aging treatments, Step 4; or thermally induced changes during stabilization, Step 6. The

connectivity of the porosity, which influences the impregnation of a second phase, also varies with processing, as determined by Vasconcelos, et al.[19] Figure 5 shows the variation in pore connectivity with densification or stabilization temperature for three Type VI gel-silica matrices with pore radii of 1.2, 3.2 and 8.1 nm. The connectivity is calculated as the topological parameter genus, where the genus of a completely dense solid is zero. For details, see References 20 or 21.
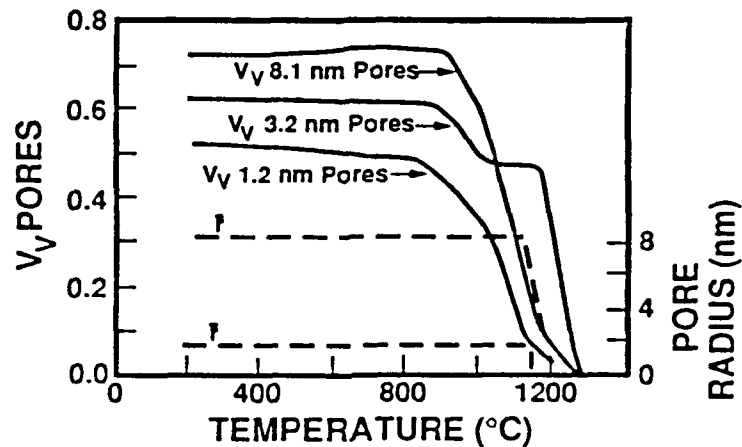

Figure 4. Variation of volume fraction and size of pores as a function of stabilization temperature for Type VI gel-silica optical matrices with 1.2nm, 3.2nm, and 8.1nm pore sizes.
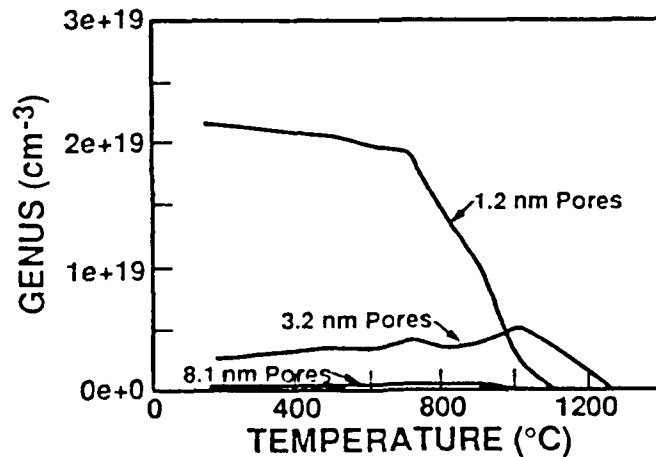

Figure 5. Variation of the connectivity of the pore network (genus) of Type VI gel-silica optical matrices as a function of stabilization temperature and initial pore size.

The optical properties of the matrices depend on the texture of the pore network and stabilization history. The UV cut-off increases to longer wavelengths as the pore size increases, due to Raleigh scattering,[22] Figure 6, and as the OH content increases.[11,16,23] Consequently, the optical characteristics of Type VI matrices are a function of processing temperature, as shown in Figure 6. The UV cut-offs for fully dense silicas, Types I-IV, are shown for comparison.[23] Absorption within the near IR increases with increasing OH content, as discussed in References 16 and 23. The OH content of the pore network varies with thermal treatment,[15] as shown in Figure 2.

Mechanical properties also vary with the texture of the gel and interconnecting pore network as shown in Figure 2 based upon Vasconcelos,[24] Park[25] and Wang's[18b] work. It is a major advantage of Method B processing over Method A that the strength and hardness of the optical matrices can be increased substantially by thermal processing without loss of the ability to impregnate the network with a second phase to form a composite. Consequently, it is possible to use Method B processing to design a matrix for an optical composite with a specific volume fraction of porosity of a particular size that has a controllable concentration of silanol groups on the pores and a pre-determined thickness of bound water or water-alcohol mixture when the organic molecules are impregnated into the pore network. This approach can be considered as molecularly tailoring of the composite and offers great potential for optimizing the optical performance of the multiple phase material.
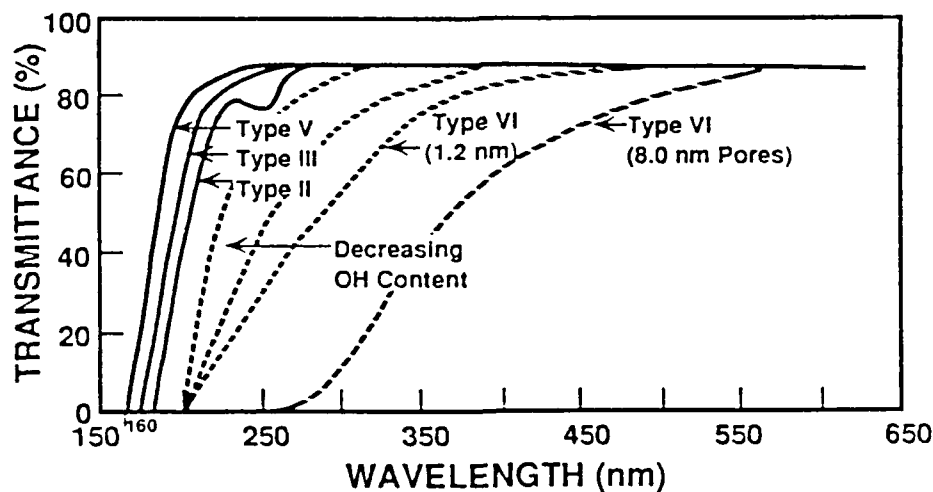

Figure 6. Ultraviolet cut-offs for Types II and III optical silica, Type V full density optical gel-silica, and Type VI porous optical matrices. Variation of uv cut-off with stabilization temperature and pore size of Type VI matrices is illustrated.

TYPES OF OPTICAL COMPOSITES

Reisfeld has reviewed[4,26] the use of Method A sol processing to form a very large variety of optical composites and discussed in detail several of those developed by her Institute. Table 2 summarizes several of the optical composites made by either Method A or Method B and their potential applications. It is clear that the versatility of these methods is extraordinary. However, in most cases considerable effort is still required to optimize the composite systems and make them commercially viable. Two systems that have received considerable attention, solid state dye lasers made by both Methods A and B, and scintillators and detectors, Method B, are reviewed here.

SOLID-STATE DYE LASERS

Incorporation of laser dyes in a solid matrix has been studied for many years with the goal of obtaining a lightweight, portable solid state system which is inexpensive to fabricate, is reliable, and is safe to handle. Organic dyes are attractive for use in lasers because they offer tunability. In contrast to tunable lasers based on transition elements, such as chromium III, doped in crystals which operate only in the near IR,[27] organic dyes can emit in the entire visible spectrum. The potential advantages of solid state dye lasers over their liquid dye counterparts are listed in Table 3.

In most solid state dye laser systems, inorganic crystals, glasses and polymers are used as host materials or saturable absorbers.[4] Recently, porous structures made by Method A sol processing have been used to incorporate dye molecules in the solid state systems.[2-7,32] Type VI gel-silica made by Method B has also been studied by King[7] and Shaw, et al.[33] and Hench, et al.[10] for lasing characteristics using two different types of dyes. The Type VI matrix is potentially superior because it can be made as a laser rod and has many desirable features, as listed in Table 2. Controlling the chemical environment of the dye molecules is likely to be essential to achieve high photostability, based upon comments by Reisfeld.[4]

In the recent work by Zhu, et al.[34] and Hench, et al.[10] rectangular gel-silica specimens of 6 X 6 X 10 mm were stabilized to 800°C for 4 hrs. The ends of the rectangles were polished to 600 grit and are parallel to each other. Other surfaces of the specimens were not polished and were kept in an as-cast condition.

The laser dye used in this study developed by Lee and Robb[35] was 4-{2-(5-phenyl-oxazolyl)}-1-methylpyridinium p-toluenesulfonate (4PyPO-MePTS).* This dye is water soluble which is a major advantage in the processing of the composite. The dye also has exceptionally high photostability.[35]

Type VI gel-silica monoliths with pore sizes ranging from 1.2 to 8 nm were filled with the dye solution, and tested using methods discussed in another publication.[34] The

---

*Aldrich Chemical Company, Inc., Milwaukee, Wisconsin.

impregnated gel-silica monoliths exhibited good environmental, chemical and thermal stability.

Table 2 Types of Optical Composites			
PROCESS METHOD A			
Matrix	*Organic*	*Application*	*Ref.*
sol-gel silica film polymer/sol-gel film	Rh6G	luminescent solar concentrators	37
sol-gel silica/polymer	BASF-241	luminescent solar concentrators	38
sol-gel alumina/polymer	Rh6G, RhB, oxazine-4, BASF-241	solid state dye laser (N_2 pumping)	5
sol-gel silica/polymer	[2,2'-Bipyridyl]-3,3'-D10L	solid state dye laser	39
sol-gel silica/ethanol	Rh6G	solid state dye laser (Q-switched Nd laser pumping	40
sol-gel silica	fluorescein	non-linear optics	41
sol-gel silica	acridine yellow	non-linear optics	4
sol-gel silica	acridine orange	non-linear optics	4
sol-gel silica film	ruthenium (II) trio (2,2' bipyridl cation	photochemical conversion of solar energy	42
sol-gel silica film	oxazine 170	reversible optical sensor for ammonia and acids	4,43
PROCESS METHOD B			
Type VI gel-silica	Rh6G	solid state dye laser (249nm K F excimer lacer, 532nm doubled Nd:YAG, 504nm flashlamp excited dye laser pumping)	7,33
Type VI gel-silica	4PyPO-MePTS	solid state dye laser (N_2 laser pumping)	10,34
	inorganic Nd (Al_2O_3)	low expansion Nd-silica laser	7
Type VI gel-silica	PBD,P-TP,P-QD (fluors) 3-HF (wavelength shifter	scintillation detector	9

49

Table 3
Advantages of Solid State Dye Lasers

Advantage	Consequence
1) Eliminate fluid pumping and flow system	Compactness, ease of handling, less expensive
2) Isolation of dye molecules by pore walls	Minimizes dimerization and aggregation
3) Increase thermal stability	Operate at higher power
4) Isolate dye molecules	Inhibits destructive photo processes
5) Steric hindrance of dye molecules by porous silica matrix	Reduces rotational modes that cause non-radiative loss
6) Easy substitution of laser rods with different dyes	Wide selection of wavelength throughout uv, visible and NIR
7) Higher thermal conductivity	Higher pumping thresholds than liquids

In brief, the impregnated gel was tested in a single optical cavity using nitrogen laser pumping at 337.1 nm in a transverse configuration where the rectangular nitrogen laser beam was focused to a line within the specimen. The maximum average power of the system was 50 mW, the maximum energy per pulse, 2.5 mJ, and the pulse duration, 800 ps.

Laser dye solutions were compared with the dye impregnated gel-silica. The latter was pumped by the nitrogen laser beam split from the primary laser source in an amplifier stage to increase the population density of the signal. The amplification factors are based upon this single path mode. The particular wavelength was selected through a grating system.

The major features of the transmittance spectra from 200 to 900 nm for 4PyPO-MePTS water solutions and for the dye impregnated gel-silica specimens are an absorption at the region between 300 and 430 nm due to the presence of the dye. Therefore, it is possible to use a nitrogen laser at 337.1 nm as the primary source for pumping. The high transmittance of the Type VI gel-silica matrix over a wide region, Figure 6, makes this an ideal host material for the impregnated laser dye.

A gain of 23 was observed after amplification with a single pass of the laser beam at 509.5 nm through the dye gel-silica sample.[10,34] A much higher gain is expected when the ends of the rectangular gel specimen are optically smooth and parallel to each other.

Advanced Composite Materials

50

Figure 7 compares the tuning curve for 4PyPO-MePTS impregnated gel-silica over the blue-green spectral region with the dye solution.[10,34] The relative energy of the laser output shows a maximum at 510 nm. This result is consistent with Contnoir's data[36] where he used water as the solvent. However, the tuning range of the dye water solution is wider (40 nm) compared to that of the solid state sample (20 nm).

The spectroscopic properties of both liquid and solid state 4PyPO-MePTS and R6G dye lasers are summarized in Ref. 10. With R6G, two kinds of host materials are compared including sol-gel derived silica and the microporous quartz glass (MQG), which is a leached sodium silicate glass. The gel-silica used in this study has a higher volume fraction of porosity (0.5) but smaller average pore radius (1.2 nm) as compared to MQG with <0.25 volume fraction of pores and an average pore radius of 3-4 nm. The maximum of the fluorescence spectra reported by Avnir, et al.[2] and Shaw, et al.[33] are very close to each other. However, Efendiev's fluorescence spectrum shows a maximum located at lower wavelength along with a lower value of the volume fraction of porosity of the glass matrix.[32] With 4PyPO-MePTS, the peak shifted to a lower wavelength for the solid state dye laser compared to that for the solution.
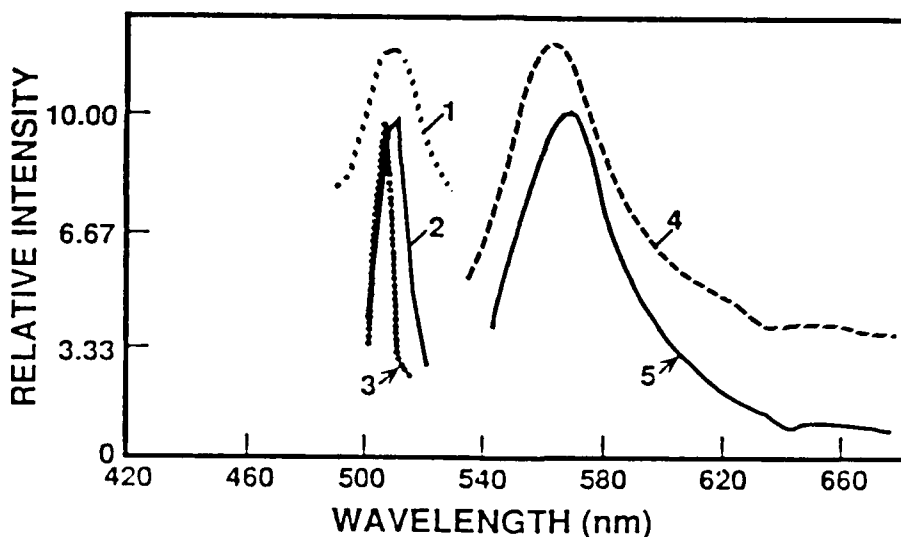

Figure 7. Tuning curves of the 4PyPO-MePTS or R6G impregnated gel-silica and the dye solutions 1-4PyPO-MePTS water solution; 2-4PyPO-MePTS impregnated gel-silica with data from the total energy output; 3-4PyPO-MePTS impregnated gel-silica with data after grating; 4- R6G water solution; and 5-R6G impregnated gel-silica.

SCINTILLATORS AND WAVELENGTH SHIFTERS

Fast radiation hard scintillators have been developed by Nogués, et al.[9] using Type VI gel-silica as the matrix with a 1.2 nm average pore radius and 0.35 volume fraction of

porosity to host organic fluors such as B-PBD, P-TP and P-QP. The silica matrix provides high γ-ray radiation resistance compared to the organic plastic scintillators and the organic fluor provides fast scintillation response. Both properties are advantageous for high-speed counting necessary for high-energy physics applications.

The problem encountered with B-PBD, P-TP and P-QP is that their fluorescence spectra typically peaks at wavelengths below 400 nm at which the gel matrix has some absorption. To solve this problem, Nogués, et al.[9] used 3-HF as a wavelength shifter to absorb the <400 nm radiation of the primary fluor and to re-emit in wavelengths of 500-600 nm. These wavelengths are advantageous as they are less absorbing in glass than the shorter wavelengths and also result in high quantum efficiency for silicon photodiodes. When analyzed for scintillation efficiency with α-, β-, and γ-ray sources, the light output was reported to be only a few times lower than the much more highly developed plastic scintillators but very much more resistant to γ-radiation.

CONCLUSIONS

Two methods of preparing optical composites have been developed. Both are extremely versatile processes. Method A, where the organic is mixed directly with the sol offers the advantage of simplicity. Method B, where the organic is adsorbed or impregnated into a porous gel-silica matrix, offers the advantage of superior mechanical properties and considerable control over the interfacial chemistry of the pores and organic phase. It is too early to establish which is preferable for commercially viable optical devices.

ACKNOWLEDGEMENTS

REFERENCES

1. L. L. Hench and J. K. West, Principles of Electronic Ceramics, Chap. 8, Wiley, New York, 1990.

2. D. Avnir, D. Levy and R. Reisfeld; J. Phys. Chem. 88, 5956 (1984).

3. D. Avnir, V. R. Kaufman and R. Reisfeld, "Organic Fluorescent Dyes Trapped in Silica and Silica-Titania Thin Films by the Sol-Gel Method. Photophysical, Film and Cage Properties," J. Non-Cryst. Solids 74, 395 (1985).

4. R. Reisfeld, J. Non-Cryst. Solids 121, 254-266 (1990).

5. E. J. A. Pope and J. D. Mackenzie, "Incorporation of Organic Dyes in Polymer/Oxide Composites," MRS Bulletin, March 17/May 15, 29-31 (1987).

6. B. Dunn, J. D. Mackenzie, J. I. Zink, O. M. Stafsudd, "Solid-State Tunable Lasers Based on Dye-Doped Sol-Gel Materials," SPIE Sol-Gel Optics Conf., San Diego, July 1990.

7. T. A. King, SPIE High Power Solid State Lasers Conf., The Hague 1990, Vol. 1277.

8. P. N. Prasad, F. E. Karasz, Y. Pang and C. J. Wung; U.S. Patent Appl. #312132.

9. J. L. Nogues, S. Majewski, J. K. Walker, M. Bowen, R. Wojcik and W. V. Moreshead, J. Am. Ceram. Soc., 71[12], 1159-1163 (1988).

10. L. L. Hench, J. K. West, B. F. Zhu and R. Ochoa, "Gel-Silica Hybrid Optics," SPIE Sol-Gel Optics Conf., San Diego, July 1990.

11. L. L. Hench and J. K. West, "The Sol-Gel Process," Chem. Rev. 90, 33-72 (1990).

12. C. J. Brinker and G. W. Scherer, Sol-Gel Science, Academic Press, New York, 1990.

13. R. Bruckner, "Properties and Structural of Vitreous Silica. I," J. Non-Cryst. Sol. 5, 121-170 (1970).

14. L. L. Hench, S. H. Wang and J. L. Nogues, "Gel-Silica Optics", Multifunctional Materials 878, 76-85, Robert L. Gunshor, ed., SPIE, Bellingham, WA (1988).

15. V. Ya. Davydov, A. V. Kiselev and L. T. Zhuravler, Trans. Faraday Soc. 60, 2254 (1964).

16. S. Wallace, "Porous Silica Gel Monoliths, Structural Evolution and Interactions with Water," Ph.D. Dissertation, University of Florida, 1990.

17. L. Nikiel, T. W. Zerda and L. L. Hench, "Molecular Motion in Porous Silica", Am. Cer. Soc. Composites Conf., Orlando, FL, Nov. 1990.

18a. C. Perry and X. Li, "NIR Studies of Monolithic Silica Gels," to be published.

18b. S. H. Wang, "Sol-Gel Derived Silica Optics," Ph.D. Dissertation, University of Florida (1988).

19. W. L. Vasconcelos, R. T. DeHoff and L. L. Hench, "Structural Evolution During Sintering of Optical Sol-Gel Silica," J. Non-Cryst. Sol. 121, 124-127 (1990).

20. W. L. Vasconcelos, "Topological Evolution and Properties of Sol-Gel Silica Monoliths," Ph.D. Dissertation, University of Florida (1989).

21. W. L. Vasconcelos, R. T. DeHoff and L. L. Hench, "A Topological Model of the Sintering of Sol-Gel Silica," in: Proc. 4th Int. Conf. on Ultrastructure Processing of Ceramics, Glasses and Composites, Tucson AZ, Feb. 1989, D. Uhlmann and D. R. Ulrich, eds., Wiley, New York, 1990 (in press).

22. E. Elias, "Pore Size Effects on the Thermal Stability of Sol-Gel Derived Silica Monoliths," Masters Thesis, University of Florida, (1989).

23. L. L. Hench and S. H. Wang, "The Sol-Gel Glass Transformation of Silica," Phase Transitions, Vols 24-26, 785-834 (1990).

24. W. L. Vasconcelos and L. L. Hench, "Mechanical Properties Evolution During Sintering of Optical Sol-Gel Silica," J. Non-Cryst. Sol. 121, 132-135 (1990).

25. S. C. Park and L. L. Hench, "Physical Properties of Partially Densified SiO_2 Gels," 186-182, In: Science of Ceramic Chemical Processing, L. L. Hench and D. R. Ulrich, eds., Wiley, New York, 1986.

26. R. Reisfeld, "Theory and Application of spectroscopically Active Glasses Prepared by the Sol-Gel Method," SPIE Int. Symp. on Sol-Gel Optics, San Diego, CA, July 8-13, 1990.

27. R. Reisfeld and C. K. Jorgensen, Structure and Bonding 69, 63 (1988).

28. G. B. Altshuler, V. Bakhanov, E. G. Dulneva and J. K. Meshkovskii, Opt. Spektrosk., 55, 369 (1983).

29. S. Muto, A. Ando, O. Yoda, T. Hanawa and H. Ito, Trans. IECE, Japan E70, 317 (1987).

30. H. Wang and L. Gampel, Opt. Communn. 18, 444 (1976).

31. V. Danilov, A. Eremenko, S. Lan'kova, D. Savel'ev and A. Stepanov, Bull. of the Academy of Sciences of USSR (Physics Series) 47, 86 (1983).

32. T. S. Efendiev, Y. V. Kostennich and A. N. Rubinov, Appl. Phys. B33, 167 (1984).

33. D. J. Shaw, C. Whitehurst and T. A. King, "Sol-Gel Glass Solid State Lasers Doped with Organic Molecules," SPIE Sol-Gel Optics Symp., San Diego, CA, July 8-13, 1990.

34. B. F. Zhu, R. Ochoa and L. L. Hench (to be published).

35. L. A. Lee and R. A. Robb, IEEE J. Quantum Electronics, QE-16, 7, 777 (1980).

36. L. J. Cotnoir, Appl. Opt. 20, 2332 (1981).

37. R. Reisfeld, R. Zusman, Y. Cohen and E. Eyal, Chem. Phys. Lett. 147, 142 (1988).

38. R. Reisfeld, D. Brusilovsky, M. Eyal, E. Miron, Z. Burshtein and J. Ivri, Chem. Phys. Lett. 160, 43 (1989).

39. M. Eyal, R. Reisfeld, A. Grabowska, "Absorption, Emission and Lifetime Measurements of [2,2'-bipyridyl]-3,3'-diol in a Sol- Gel Glass", Chem. Phys. Lett.

40. G. B. Atshuler, V. A. Bakhanov, E. G. Dulneva, A. V. Erofeev, O. V. Mazurin, G. P. roskova and T. S. Tsekhomskaya. Opt. Spectrosc, (USSR) 62, 709 (1988).

41. R. Reisfeld, M. Eyal and R. Gvishi, Chem. Phys. Lett. 138, 377 (1987).

42. R. Reisfeld, D. brusilovsky, M. Eyal and C. K. Jorgensen, Chimia 43, 385 (1989).

43. V. Chernyak, R. Reisfeld, R. Gvishi and D. Venezky, "Oxazine 170 in Sol-Gel Glass and PMMA Films as A Reversible Optical Waveguide Sensor for Ammonia and Acids," submitted to Sensors and Materials.

54

b. Sol–Gel Silica for Precision and Multifunctional Optics†

Larry L. Hench

Advanced Materials Research Center, University of Florida, One Progress Blvd, 14, Alachua, FL 32615, USA

Abstract: The sol–gel method of producing silica optics results in both fully dense Type V gel-silica and a Type VI gel-silica intermediate product. Advantages of the Type V gel-silica for net shape precision optics are described. Uses of the Type VI gel-silica as multifunctional optical components is discussed, including transpiration cooled windows, fast radiation-hard scintillating detectors and solid state dye lasers.

1 INTRODUCTION

Optical systems have become one of the largest growth fields in high technology industry. All optical systems require many precision optical components. In some cases the optical components are very small and extremely difficult and too costly to machine. Thus there is a major need for a new approach to the manufacture of small precision optics.

Precision optics have been made by basically the same process since the time of Galileo, i.e. grains of crystalline quartz have been melted with various fluxes, homogenized at very high temperatures above the liquidus and cast into glass ingots.[1-3] Sections of the ingots with minimum bubbles, seeds, striae or other defects have been selected by hand for grinding by skilled opticians into the shape of lenses, prisms, windows or mirrors, followed by successive polishing steps, again performed by highly trained optical technicians. The quality of each optical component is therefore dependent on the sum-

mation of the quality of each step of processing, which in turn is a function of the skill, training and time devoted by technicians. The performance of an optical system is an aggregate of the quality of the individual components and therefore is highly dependent on the availability and skill of technical manpower. As the size of optical components decrease the limitations of human grinding and polishing become even more severe. Thus there is a finite limitation to size and precision imposed by economics and availability of skilled personnel. A major objective of sol–gel processing of precision optical components is to eliminate the need for grinding and polishing. This objective is termed *net shape casting*. There is no limitation imposed by size in sol–gel casting of optics, in fact smaller is easier. There is also no limit of centro-symmetry as is often desired for traditional grinding and polishing. Aspheric optics or angular optics are equally easy. All that is required is a master mold.

Until recently optical components have for the most part also served only a single function in an optical system, i.e. lenses refract, mirrors reflect, windows transmit, filters absorb and lasers amplify. As optical systems requirements become ever more demanding there is a great incentive for components to serve more than one function. This need is very difficult to satisfy with traditional methods of

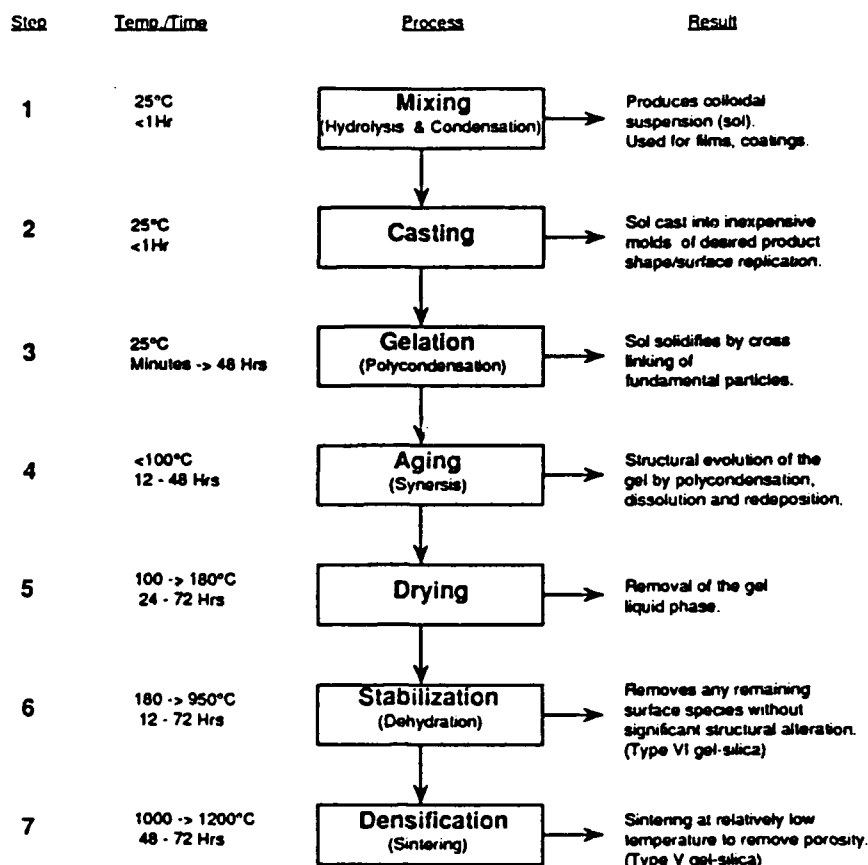| Step	Temp./Time	Process	Result
1	25°C <1 Hr	**Mixing** (Hydrolysis & Condensation)	Produces colloidal suspension (sol). Used for films, coatings.
2	25°C <1 Hr	**Casting**	Sol cast into inexpensive molds of desired product shape/surface replication.
3	25°C Minutes -> 48 Hrs	**Gelation** (Polycondensation)	Sol solidifies by cross linking of fundamental particles.
4	<100°C 12 - 48 Hrs	**Aging** (Synersis)	Structural evolution of the gel by polycondensation, dissolution and redeposition.
5	100 -> 180°C 24 - 72 Hrs	**Drying**	Removal of the gel liquid phase.
6	180 -> 950°C 12 - 72 Hrs	**Stabilization** (Dehydration)	Removes any remaining surface species without significant structural alteration. (Type VI gel-silica)
7	1000 -> 1200°C 48 - 72 Hrs	**Densification** (Sintering)	Sintering at relatively low temperature to remove porosity. (Type V gel-silica)

Fig. 1. Sol–gel processing sequence for multifunctional optics.

Table 1. Potential advantages of gel-silica optics

Net shape/surface casting
- Complex geometries
- Lightweight optics
- Aspheric optics
- Surface replication (e.g. Fresnel lenses and gratings)
- Internal structures
- Reduced or no finishing
- Higher reliability
- Eliminate grinding
- Reduced or no polishing

Improved physical properties (Type V)
- Lower coefficient of thermal expansion (CTE)
- Lower vacuum ultraviolet cut-off wavelength
- Higher optical transmission
- No absorption due to H_2O or OH bands
- Lower dispersion
- Lower solarization
- Higher homogeneity
- Fewer defects
- No striae

Transparent porous structures (Type VI)
- Impregnation with organic polymers
- Graded refractive index lenses (GRIN)
- Laser enhanced densification
- Controlled chemical doping
- Controlled or variable oxidation states of dopants
- Controlled interfaces with polymers

making precision optics. The fundamental characteristics of glass as an isotropic, homogeneous solid generally restrict its use to a single optical function.

Sol–gel chemical processing of silica provides a new approach to each of the historical restrictions of silica optical components summarized above, i.e. (1) elimination of hand operations in manufacturing by net shape casting and (2) development of multifunctional optics by producing ultraporous silica matrices that are optically transparent.

A summary of the potential advantages offered by sol–gel processing optics is given in Table 1. Many of these advantages have been realized during the last 2 years of R&D in this field. Several examples are presented in this review.

2 SOL–GEL PROCESSING

Recent publications discuss the important features of sol–gel technology used in producing monolithic silica optical components.[4,5] There are three general approaches to making sol-gel monoliths suitable for optical applications:[5,6]

Method 1: Gelation of colloidal powders.
Method 2: Hydrolysis and polycondensation of

alkoxide precursors, followed by hypercritical drying to form aerogels.

Method 3: Hydrolysis and polycondensation of alkoxide precursors, followed by aging and drying under ambient atmospheres to form xerogels.

Method 1 has been used by Shoup[7] to make silica for reflective optics. Method 2 has been used by Kistler,[8] Fricke,[9] Phalippou et al.[10] and others to make aerogels which can be used as very low density optical components with an index of refraction close to 1·00, or densified to form silica glass.[11]

In order to make net shape multifunctional optics Method 3 is used,[4] with an emphasis on controlling at a molecular level each of the seven steps of processing listed in Fig. 1.

In our process the alkoxide is tetramethylorthosilicate (TMOS) and the catalyst is either nitric acid or hydrofluoric acid, depending upon the average pore size desired after drying. Type V gel-silica used in full density net shape precision optics requires all seven steps listed in Fig. 1. Partially dense, controlled porosity Type VI gel-silica optics require only the first six steps listed in Fig. 1. (For detail of the differences in processing and properties of Types I, II, III, IV, V and VI silicas see Refs 4 and 5.)

3 TYPE V, DENSE GEL-SILICA

The average pore size of the dried monoliths used in making Type V dense gel-silica is very small, in the range of 1·2 nm, with a very narrow size distribution. Densification occurs at a low temperature, 1150°C, in a dry atmosphere due to the very small pore radii and very large, >700 m²/g, surface area. There is almost no change in pore radii as densification occurs. As shown by Vasconcelos,[12] nearly all the change in texture during the densification is due to a decrease in connectivity of the pore network, which decreases the surface area and volume fraction of the pores per unit volume. At 1150°C all the pores are eliminated and the bulk density of the glass is 2·2 g/cm³, equivalent to that of fused quartz or synthetic vitreous silica, Types I–IV, made by other processes.[4,5,13]

The shape of the optical component is determined by the shape of the mold used for gelation (Step 2 in Fig. 1). With use of precision molds and sol–gel processing it is possible to achieve as-cast tolerances for the diameter, thickness and radius of curvature of silica lenses which exceed the tolerances achieved by precision grinding and polishing. A major
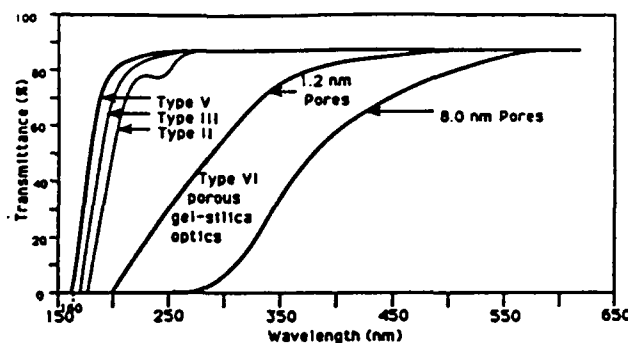

Fig. 2. UV cut-offs of Types I, II, III, V and VI silica.

advantage of the sol–gel method is the low temperature (<100°C) of casting and gelation. Consequently inexpensive polymers can be used for molds. The low temperatures also mean that molds can be reused. Consequently the economics of gel-silica precision optics are very favorable compared with traditional processing methods.

The optical properties of Type V gel-silica are also superior to most of the commercial grades of optical silica.[4,5,13] Figure 2 compares optical transmission from the vacuum ultraviolet range of wavelengths to the visible for Type V gel-silica with typical curves for Types II and III optical silicas. Type V gel-silica has a lower wavelength UV cut-off than even Type III silica, made by flame hydrolysis of $SiCl_4$, which is used for UV applications. Removal of cation and hydroxyl impurities in sol–gel silica processing and maintenance of purity by low temperature dehydration and densification is responsible for the improvement in optical transmission. The low temperatures of densification also eliminate problems of warping and sagging, and loss of dimensional tolerance. This is a very important advantage of the alkoxide route (Method 3) to make precision optics.

Transmission in the near IR of Type V gel-silica is also excellent, as illustrated in Fig. 3. There are no absorption peaks due to hydroxyl impurities (see Table 1), unlike Type III optical silicas.

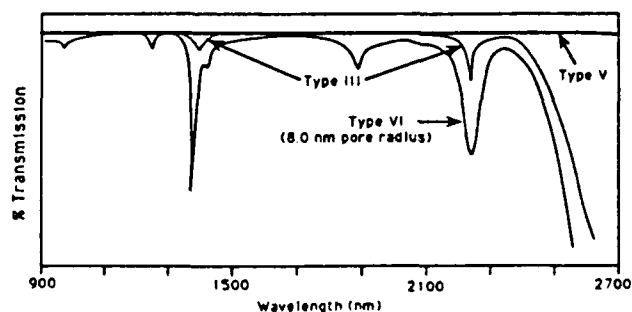Other physical properties are similar to both UV

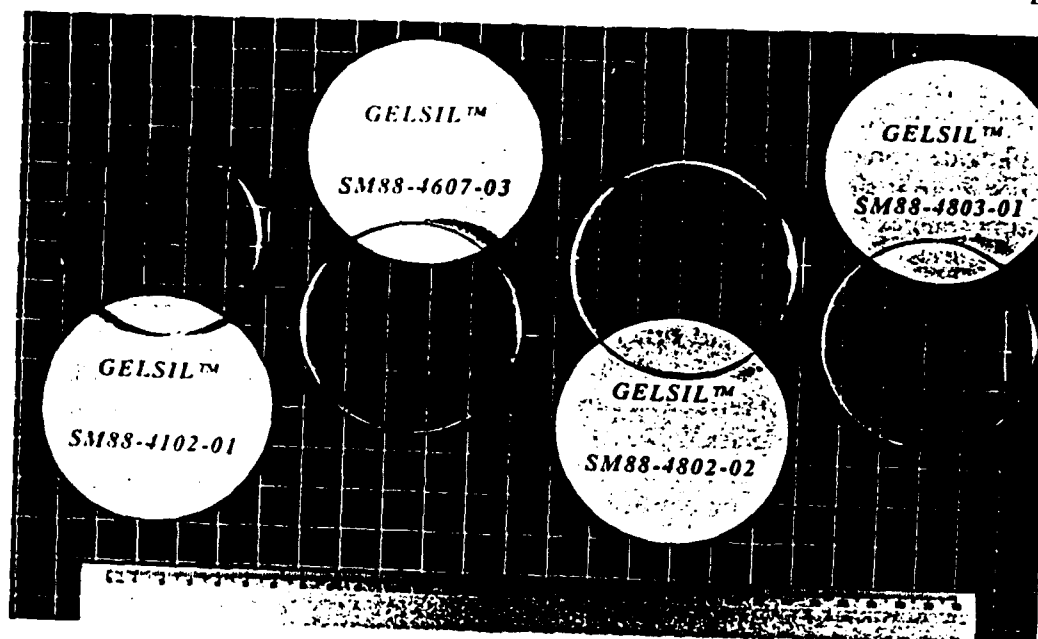Fig. 3. NIR transmission curves for Types III, V and VI silica.

Fig. 4a. Net shape, net surface plano-plano Type V gel-silica optical windows.

Fig. 4b. Net shape casting of 19 cm diameter lightweight mirror with integral face plate.

Fig. 4c. Optically transparent ultraporous Type VI gel-silica (10 cm diameter).

and IR grade optical silicas. However, the chemical method results in greater homogeneity and lower striae, and fewer heterogeneities. There is also the advantage of a lower coefficient of thermal expansion of 0.2×10^{-7} cm cm.

4 TYPE VI, ULTRAPOROUS GEL-SILICA

References 5, 14 and 15 show that Type VI gel-silica monoliths heated up to 800–900 C still retain a large volume fraction of porosity. Vasconcelos' studies of the topological characteristics of these gels show that this porosity is completely interconnected.[12] Because of the very small size of the pores (1.2–8.0 nm) the material is optically transparent (Fig. 4). By heating to 800–900 C stabilization (Step 6 in Fig. 1) the concentration of silanols on the surface of the pore network can be controlled, as illustrated in Fig. 3, thereby making the material chemically stable when exposed to an aqueous environment. This is an

especially important characteristic in the use of Type VI gel-silica for impregnation with second phases as required for many multifunctional optical applications.[4,5]

It is possible to vary the pore size and volume fraction of porosity of the Type VI gel-silica by using HF as a catalyst in Step 1, as discussed by Parsell,[16] Vasconcelos[12] and Elias.[15] Details of textural characteristics and the thermal behavior of monoliths with a range of pore sizes from 1·2 to 8·0 nm are presented elsewhere by Vasconcelos[12] and Elias.[15] Increasing the pore size of the network is important for a number of multifunctional optical applications, as shown below. However, the larger pores degrade the UV cut-off to some extent, from 160 to 235 nm as shown in Fig. 2, probably due to Rayleigh scattering as shown by Elias.[15] The porous Type VI optics also have a small concentration of residual hydroxyls retained on the pore network (Fig. 3), with the concentration dependent on the maximum stabilization temperature. Davydov *et al.*[17] have shown that nearly 1100°C is required to eliminate all hydroxyls from silica gel powders by thermal decomposition. Since the larger pore network is more thermally stable,[12,14,15] the larger pore optics can be heated to the higher stabilization temperatures to decrease the OH content and still retain a very large volume fraction of porosity. The increase in volume fraction of porosity and greater thermal stability of the larger pore Type VI gel-silica offers a major advantage for the multifunctional optical applications discussed below.

5 TRANSPIRATION COOLED UV WINDOWS

Multifunctionality is highly desirable for optically transmitting windows in high speed rocket guidance systems due to severe operating conditions. The windows need to transmit light over a broad range of wavelengths, including the ultraviolet. Most importantly, the optical transmission must not be affected by very high ambient temperatures and impingement of very energetic gases. Reasonably good structural strength, thermal stability and thermal shock resistance is also required for rocket windows.

A unique approach to achieving thermally resistant properties is to cool the window by passing gases *through* the window. Such a concept is possible with the ultraporous Type VI gel-silica monoliths.

The objective of the multifunctional optical component is to cool the window via transpiration

of gases through the interconnecting pore structure while optical transmission is maintained.

The first step in evaluation of the concept of a transpiration cooled window is to determine whether transpiration of gases is possible through a porous Type VI gel-silica medium. The second step, if transpiration is possible, is to characterize the transpiration velocity as a function of pressure, pore radius, sample thickness and type of gas. The third step is to determine whether UV transmission occurs through the Type VI porous gel-silica window at elevated temperatures and with gases impinging on it. Fourth, thermal shock characterization of the window is also needed.

Most of these multifunctional performance characteristics have now been demonstrated.[18,19] UV transmission was shown to exist at temperatures >1000°C when exposed to an oxygen-acetylene torch heat source.[18] Flow of both He and N_2 through the window has been demonstrated at pressures up to 3·2 MPa. Maximum He transpiration velocities of up to 3 cm/s have been measured for windows with 5-nm pores.[19] This is three times the velocity needed for transpiration cooling. The flow rate of He is considerably faster (~3×) than nitrogen. Transpiration velocities of He of 0·6 cm/s result in cooling effects as large as 44°C from 160°C. Tests of cooling at elevated temperatures are under way.

6 FAST, RADIATION-HARD SCINTILLATING DETECTOR

The physical features of Type VIA porous gel-silica described above are attractive to use as matrices for doping or impregnation with fluors, non-linear optical polymers or compounds, wavelength shifters or lasing dyes. The result is a hybrid multifunctional optical component. Table 2 lists examples of some organic and inorganic compounds that have been successfully impregnated into several Type VI gel-silica samples.[4,5]

It is possible to select various combinations of second phase loading which are a function of pore size and total pore volume of the porous optical matrix. Previous studies have shown that physical properties such as flexural strength, compressive strength, elastic modulus, coefficient of thermal expansion, density and microhardness are also a function of pore size and volume fraction of porosity.[12] For example,[18] an 800 C heat treatment of a 1 in diameter × ¼ in thick plano-plano Type VI gel-silica blank with 1·2 nm pores produces an

Table 2. Compounds impregnated into Type VI porous gel-silicas[4]

Non-linear optical polymers	Transition metals
PBT (phenylenebenzobisthiazole)	Cu
MNA (2-methyl-4-nitroaniline)	Ni
	Cr
Organic fluors	Ce
B-PBD ((2-4'-*t*-butylphenyl)	Ag
5-(4"-biphenylyl)-1,3,4-oxadiazole)	Fe
P-TP (*p*-terphenyl)	Co
P-QP (*p*-quarterphenyl)	
Wavelength shifter	Rare earths (lanthanides)
3-HF (hydroxyflavone)	Nd
	Er
Laser dye	
Rhodamine 6G	
4PyPO-MePTS	

optically transparent component that weighs 4·02 g, has a 117 HV microhardness and has nearly 2500 m^2 surface area with pores ~1·2 nm radius. This component can accept 1·6 cm^3 of a dopant second phase using various impregnation techniques. Thus 40–50 vol.% of the component can be filled with a second phase.

If a harder and stronger component is desired, a 900°C heat treatment can be used although the amount of dopant phase is reduced to 1·31 cm^3.

The Type VI gel-silicas with larger pore sizes described above make it possible to impregnate the component with higher molecular weight polymers. The same 800°C treatment of a 1 in diameter × ¼ in thick sample with 8·0 nm pores produces an optical component that weighs 1·98 g, has a 18 HV micro-hardness and has nearly 583 m^2 surface area with pores ~8·0 nm radius. This component can accept 2·36 cm^3 of a dopant second phase in its 70–75 vol.% porosity.

For example, consider the fast radiation-hard scintillator developed by Nogues *et al.*[20] They utilized a Type VI gel-silica matrix with a 1·2 nm average pore radius and 0·35 volume fraction porosity as a host matrix for organic fluors to produce a fast, radiation-hard scintillation detector. The silica matrix provides high radiation resistance compared to the organic plastic scintillators and the organic fluor provides fast scintillation response. Both properties are advantageous for the high-speed counting necessary in high-energy physics applications. The primary fluors used by Nogues *et al.*[20] B-PBD, P-TP and P-QP (Table 2), have good radiation resistance and short decay times of a few nanoseconds, but the fluorescence spectra typically peak at wavelengths below 400 nm, making it difficult to measure. To overcome this problem

Nogues *et al.*[20] used another fluor, termed a wavelength shifter (WLS) 3-HF (Table 2), which absorbs the <400 nm radiation of the primary fluor and re-emits in wavelengths of ≈500–600 nm. These wavelengths are advantageous as they are less absorbing in glass than the shorter wavelengths and also result in higher quantum efficiency for silicon photodiodes. When analyzed for scintillation efficiency with α-, β- and γ-ray sources, the light output was reported to be only 6–7 times lower than the much more highly developed plastic scintillator. The γ-radiation resistance of the silica matrix was many times greater than the organics. These are very encouraging results for the first generation of multifunctional optical components.

This same type detector with the 3-HF fluor dopant was supplied by Nogues for use as the WLS/ detector used for the high-temperature UV transmission test in the above-mentioned transpiration window study.[18] A source emitting 365 nm radiation passes through the heated porous window being tested for transmission and is absorbed and re-emitted by the detector as visible green → yellow-green light from the WLS/detector. Thus a qualitative and visual method for testing high-temperature UV transmission through a porous silica matrix was achieved. The Type VI porous gel-silica window protected the window from the oxygen-acetylene torch. The combination window–detector system demonstrates the effectiveness and versatility of this new class of optical materials.

7 SOLID STATE GEL-SILICA DYE LASER

There are many advantages of organic laser dyes, including a wide tuning range of 300–3800 nm and high quantum yields of fluorescence, absorption and emission. However, there are many limitations of liquid dye lasers, including thermal stability, ease of handling, spectral shifts and non-radiative quenching of upper lasing levels. These disadvantages are associated with the liquid medium of the dye. Consequently incorporation of laser dyes in thermally stable gel-silica matrices offers potentially great advantages for tunable dye lasers.[21–24]

Two studies have been conducted to test these potential advantages. In both Type VI optically transparent gel-silica matrices were prepared following a schedule similar to Fig. 1. The porous gels were prepared to yield average pore radii of 1·2 nm and pore volume fractions of ≥0·46.

4-[2-(5-phenyloxazolyl)]-1-methylpyridinium-*p*-toluenesulfonate (4PyPO-MePTS) was impregnated

by Zhu & Hench[25] into the gel-silica matrix, which had been stabilized at a critical temperature to control the thickness of the adsorbed water layer. This laser dye was selected due to its excellent photostability, as demonstrated by Lee & Robb.[26]

The impregnated specimens were tested for lasing in a single cavity using nitrogen laser pumping at 337·1 nm in a transverse configuration where the rectangular nitrogen laser beam was focused to a line within the specimen. The testing system, PRA 1000 in a triggered mode, was used as an amplifier to increase the signal output. Lasing of a gel-silica hybrid dye laser was observed in the blue-green spectral region.

Power outputs were measured at single modes after the grating. Gains of 7–35 times the standard cell were obtained at 509·5 nm with half widths of 0·3 nm. Details are presented elsewhere.[25]

Successful lasing of an equivalent Type VI gel-silica matrix impregnated with Rhodamine 6-G(R6G) laser dye has been reported by Berry & King.[24] They showed that the photostability of the R6TG laser dye increased by an order of magnitude by using the Type VI gel-silica matrix to replace the liquid organic laser host. Because the dye molecules were isolated within the ultrapore silica network the formation of dimers of the dye molecules was negligible; when dimers are formed in liquid media they greatly decrease the lasing ability of the dye.

Also Berry & King conclude that molecular immobilization of the dye molecules in the porous glass matrix can reduce the intermolecular collisional deactivation of dye molecules. Collisions can occur between the dye molecules and other dye molecules, photodecomposition products or impurities. Since dye molecules cannot migrate in the porous silica matrix then repeated quenching and decomposition is prevented.

The isolation of dye impurities from the photoactive dye molecules by the porous matrix prevents quenching of upper laser levels. Likewise, the adsorbed photoactive dye molecules are isolated from organic solvents and gases with low chemical or thermal stability. Consequently molecular isolation of the dye molecules results in higher quantum yields and improved spectroscopic and kinetic behavior of the dyes.

An additional advantage of incorporating laser dyes in the porous gel-silica matrix is improved heat dissipation. Berry & King suggest that there is a more uniform temperature distribution throughout the photoactive medium which reduces formation of refracting convection currents common in liquid dye hosts. Consequently thermal lensing, which leads to loss in laser energy and reduction in beam quality, is reduced. Since excess heat can be removed at a faster rate, laser outputs of higher powers can be achieved for the same cavity.

It may also be possible to use transpiration cooling of the dye-impregnated porous matrix to dissipate heat even more quickly and effectively.

By varying the volume fraction and size of porosity in the gel-silica matrix it is possible to achieve relatively high dye concentrations. This should make it possible to design more compact and efficient laser cavities. The higher concentrations are feasible since collision-induced aggregation and dimerization of the molecules is minimized by chemisorption of the dye molecules in the pore network.

Berry & King's investigation of the solid state R6G dye laser in Type VI gel-silica confirms an increase in the fluorescence lifetime of the upper laser level in the dye molecules. They conclude that the increase is due to bonding of the dye molecules in the porous glass network which makes the transition to lower states less allowed. Consequently population inversion is easier to attain and threshold for gain is reduced. Laser linewidths are similar to that of R6G in methanol.

Recent work of Berry & King[24] using a C504 pulsed dye laser for pumping the solid state R6G Type VI dye laser shows great promise with no photodegradation of the dye doped glass even after 100 high-energy pulses.

The results from Zhu & Hench and Berry & King indicate that flashlamp pumping of solid state dye lasers may be feasible. If this can be achieved Berry and King suggest it should be feasible to use small cavities that house solid state dye-Type VI rods with flashlamps and samarian down-conversion filters to produce a low-cost compact tunable laser.[24] Such a configuration would be much more along the lines of conventional solid state ruby or Nd:YAG or glass lasers. The advantages offered by net shape, net surface casting of Type V or Type VI gel-silica (Section 3) will make it feasible to use either slab or rod configurations for these new solid state tunable dye lasers. There should also be important economic advantages of net shape casting of gel-silica matrices over traditional glass or crystal solid state lasers.

8 CONCLUSIONS

Sol-gel processing of silica monoliths has resulted in two new types of silica optics: Type V, fully dense gel-

silica, and Type VI, ultraporous, optically transparent gel-silica. An important advantage of both Types V and VI gel-silica is the ability to produce net shape castings of precision optical components, eliminating costly and time-consuming grinding and polishing. The ultrahigh purity and ultrahigh homogeneity of Type V gel-silica also offers large advantages in many optical systems where minimal absorption is required in the vacuum UV to the NIR and a very low coefficient of thermal expansion is desired.

The Type VI porous gel-silica optics offers a totally new approach to tailoring optical components. It is possible to cool the optics by transpiration cooling. It is possible to impregnate optical polymers into the matrices and achieve new hybrid optical components such as solid state dye lasers. Applications of this new technology should expand tremendously in the next few years.

ACKNOWLEDGEMENTS

REFERENCES

1. BRUCKNER, R., *J. Non-Cryst. Solids*, 5 (1970) 123-75.
2. GRAYSON, M. (ed.), In *Encyclopedia of Glass, Ceramics, and Cement*. John Wiley, New York, 1985, pp. 837-45.
3. ILER, R., *The Chemistry of Silica*. John Wiley, New York, 1979.
4. HENCH, L. L., WANG, S. H. & NOGUES, J. L., In *Multifunctional Materials*, Vol. 878, ed. Robert L. Gunshor. SPIE, Bellingham, Washington, 1988, p. 76.
5. HENCH, L. L. & WEST, J. K., *Chem. Rev.*, 90 (1990) 33-72.
6. BRINKER, C. J. & SCHERER, G. W., *Sol-Gel Science*. Academic Press, New York, 1989.
7. SHOUP, R. D., In *Ultrastructure Processing of Advanced Ceramics*, ed. J. D. Mackenzie. John Wiley, New York, 1988, p. 347.
8. KISTLER, S. S., *Nature*, 127 (1931) 742.
9. FRICKE, J. (ed.), In *Aerogels, Springer Proceedings in Physics*, Vol. 6. Springer-Verlag, Heidelberg, 1986.
10. PHALIPPOU, J., PRASSAS, M. & ZARZYCKI, J., *J. Non-Cryst. Solids*, 48 (1982) 17.
11. HENCH, L. L. & WANG, S. H., The Sol-Gel Glass Transformation of Silica. *Phase Transitions*, 24-26 (1990) 785-843.
12. VASCONCELOS, W., PhD thesis, University of Florida, 1989.
13. NOGUES, J. L., BALABAN, C., MORESHEAD, W. V. & SHEU, R. S., In *Advanced Ceramics*, ed. W. P. E. Longo, S. N. Monteiro & J. D. Filho. Florida-Brazil Institute, Rio de Janeiro, 1989, pp. 51-60.
14. WANG, G., Masters thesis, University of Florida, 1988.
15. ELIAS, E., Masters thesis, University of Florida, 1989.
16. PARSELL, D., Personal communication, University of Florida, 1990.
17. DAVYDOV, V. YA., KISELEV, A. V. & ZHURAVLEV, L. T., *Trans. Faraday Soc.*, 60 (1964) 2254.
18. HENCH, L. L. & FOSMOE, A., Multifunctional silica optics. In *Fall MRS Meeting Proceedings*, Boston, MA, 1989.
19. FOSMOE, A. & HENCH, L. L., Transpiration cooled VI silica rocket windows. In *Better Ceramics Through Chemistry, Spring MRS Meeting*, San Francisco, CA, 1990.
20. NOGUES, J. L., MAJEWSKI, S., WALER, J. K., BOWEN, M., WOJCIK, R. & MORESHEAD, W. V., *J. Am. Ceram. Soc.*, 71(12) (1988) 1159-63.
21. AVNIR, D., LEVY, D. & REISELD, R., *J. Phys.*, 88 (1984) 5956.
22. AVNIR, D., KAUFMAN, U. R. & REISFELD, R., *J. Non-Cryst. Solids*, 74 (1985) 395.
23. SALIN, F., LE SAUX, G., GEORGES, P., BRUN, A., BAGNALL, C. & ZORZYNCKI, J., *Optics Lett.*, 14 (1989) 785.
24. BERRY, A. & KING, T., Personal communication, University of Manchester, 1990.
25. ZHU, B. F. & HENCH, L. L., SPIE Meeting, San Diego, CA, 1990.
26. LEE, L. A. & ROBB, R. A., *IEE J. Quantum Electron.* QE-16 (1980) 777.

SECTION V

PROJECT C:
Theoretical Calculations of Gel-Silica

11

a. QUANTUM CALCULATIONS ON SOL–GEL SILICA CLUSTERS

J. K. WEST, S. WALLACE, L. L. HENCH, AND C. R. LISHAWA

11.1. INTRODUCTION

Recent developments in sol–gel optics have produced type V amorphous silica monoliths with extremely wide optical transmission bands [1,2]. Laser-densified optical waveguide tracks have been produced in porous type VI silica [3]. Optically transparent soda–silica monoliths with good UV cutoff wavelengths have also been made [4] at substantially lower densification temperatures than the pure silica system.

These developments and others increase the importance of understanding the structural models of sol–gel silica and the theoretical grounds for the UV cutoff of silica optics. Thus, semiempirical quantum calculations have been initiated using Hückel molecular orbital (HMO) [5] and intermediate neglect of differential overlap (INDO) molecular orbital models. The INDO program was made available by the Quantum Theory Project at the University of Florida [6].

11.2. MODEL STRUCTURES

The structures evaluated contain from one to six silica tetrahedra. In each model two bridging oxygens and two nonbridging oxygens are bonded to each silicon.

111

One hydrogen is bonded to each of the nonbridging oxygens to terminate the structure and balance charge. Both ring and chain cluster models of silica tetrahedra were evaluated and their energies compared. Figure 11.1 shows the two-dimensional projection of a geometrically optimized INDO chain and ring structure for four silica tetrahedra. These projections are typical of the hydroxylated silica structures modeled in this study.

The clusters were each optimized for the minimum energy using a molecular mechanics (MM2) [7] routine. The molecular orbitals were calculated first using HMO then using geometrically optimized INDO calculations. The molecular energies were evaluated and compared to establish the relative stability of each structure. The energy gap between the highest occupied molecular orbital (HOMO) and the lowest unoccupied molecular orbital (LUMO) for the single states and the corresponding UV cutoff wavelength were determined.

The heteroatom parameters, k and h, which are used to modify the Hamiltonian matrix for the HMO calculations, were adjusted to compensate for the differences in the bonding orbitals between carbon and silicon. In HMO theory the matrix diagonal represents the ionization potentials, σ_i, of the valence electrons for carbon i, where $h = 1$, and the off diagonal matrix elements represent the bond interactions, β_{ij}, between carbon atoms i and j, where $k = 1$:

$$\sigma_i = -11.26 \times h_i(\text{eV}) \tag{1}$$

$$\beta_{ij} = -2.5 \times k_{ij}(\text{eV}) \tag{2}$$

The HOMO–LUMO gap for a single silica tetrahedra was set at 8.2 eV, and the parameters were determined. Thus, the relative energies of the various structures were determined without further adjustment of the parameters by comparison to a single silica tetrahedra. Table 11.1 shows the results of the empirical determination of the k and h parameters for silicon [8], carbon, oxygen, and nitrogen [5].

(a) CHAIN OF 4 SILICA TETRAHEDRA   (b) RING OF 4 SILICA TETRAHEDRA
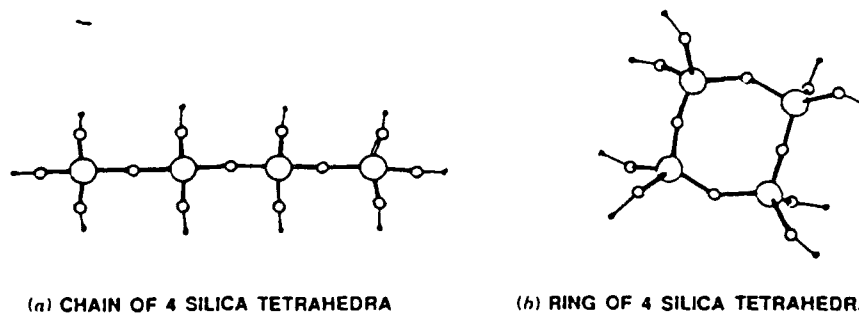
Figure 11.1. The two dimensional projection of a geometrically optimized INDO chain and ring structure for four silica tetrahedra.

TABLE 11.1. Heteroatom Parameters

Bond	k parameter	Reference No.	Atom	h parameter	Reference No.
C—C	1.00	5	C	1.00	5
C—O	0.80	5	O	1.00	5
C—N	0.80	5	N	1.50	5
C=C	1.00	5	Si	0.80	8
C=O	1.414	5			
C=N	1.0	5			
C=Si	0.72	8			
O=Si	1.4	8			

11.3. RESULTS AND DISCUSSION

Table 11.2 summarizes the HMO calculations of these silica structures. The Hückel energy (HE) is the total molecular energy for each structure. The relative stability of each structure can be compared using the HE per silica tetrahedra. In Table 11.3, summarizing the INDO calculations, a similar calculation is shown to compare the relative stability of the INDO structures. The more negative the energy, the more stable the structure.

Figure 11.2 shows the INDO energy per silica tetrahedra for rings and chains as a function of the number of tetrahedra and suggests that the chain structures are more stable than the rings. This has been observed experimentally using
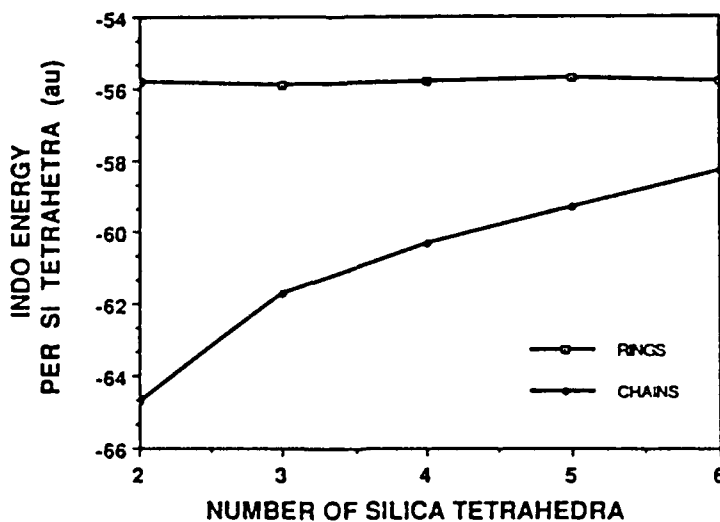

Figure 11.2. INDO energy per silica tetrahedra for rings and chains as a function of the number of tetrahedra.

66

TABLE 11.2. Hückel Calculations for Silica Structures

Number of Silica Tetrahedra	Structure	Resonance Energy (eV)	HE[a] per Tetrahedra (eV)	HOMO–LUMO[a] Bandgap (eV)	UV[a] Cutoff Wavelength (nm)
1	Tetrahedra	14.3	−67.8	8.22	151.1
2	Chain	−25.2	−94.4	7.22	172.1
2	Ring	39.0	−69.5	7.29	170.2
3	Chain	41.9	−60.6	6.87	180.8
3	Ring	11.9	−70.4	7.29	170.3
4	Chain	46.3	−58.5	5.16	240.7
4	Ring	56.2	−56.7	6.20	200.3
5	Chain	70.0	−59.0	6.52	190.5
5	Ring	−18.9	−76.7	7.60	163.4
6	Chain	−11.6	−75.2	8.80	141.1
6	Ring	84.3	−70.8	6.19	200.5

[a] *Abbreviations used:* HE, Hückel energy; HOMO, highest occupied molecular orbital; LUMO, lowest unoccupied molecular orbital; UV, ultraviolet.

114

TABLE 11.3. INDO Calculations for Silica Structures

Number of Silica Tetrahedra	Structure	Dopant [mol %]	INDO[a] Energy per Tetrahedra (a.u.)	HOMO–LUMO[a] Bandgap (a.u.)	UV[a] Cutoff Wavelength (nm)
1	Tetrahedra	0.00	−73.82	0.6201	87.1
2	Chain	0.00	−64.72	0.4129	130.7
2	Chain-Na	6.25	−64.46	0.3195	168.1
2	Chain-OH	5.88	−73.39	0.1561	345.9
2	Chain-water	5.88	−73.78	0.3950	136.7
2	Ring	0.00	−55.82	0.4786	112.8
3	Chain	0.00	−61.74	0.4069	132.7
3	Ring	0.00	−55.86	0.5082	106.2
4	Chain	0.00	−60.25	0.3867	139.6
4	Ring	0.00	−55.80	0.4725	114.3
4	Ring-Na	4.00	−55.62	0.3319	162.6
4	Ring-OH	3.85	−60.28	Degenerate	N/A
5	Chain	0.00	−59.35	0.4024	134.2
5	Ring	0.00	−55.76	0.3740	144.3
6	Chain	0.00	−58.55	0.3974	135.8
6	Ring	0.00	−55.79	0.4696	114.1
6	Ring-Na	2.78	−55.69	0.3564	151.5
6	Ring-OH	2.70	−58.73	Degenerate	N/A

[a] Abbreviations used: INDO, intermediate neglect of differential overlap; HOMO, highest occupied molecular orbital; LUMO, lowest unoccupied molecular orbital; UV, ultraviolet; N/A, not applicable.

115

NMR spectroscopy [9], where a linear, as opposed to a ring, growth model most consistently interprets the experimental structural evidence prior to gelation.

Investigators [10, 11] have proposed models for the structure of acid-catalyzed silica gels containing two levels of structure formed before gelation. These models propose the formation of primary particles of diameter 1–2 nm that agglomerate to form secondary particles of about 4–6 nm before drying. The secondary particles give rise to the pore structure after drying.

Table 11.4 shows the differences in the INDO structural energies between chains and rings. The relative stability of chains compared to rings decreases as the number of silica tetrahedra increases, as shown in Fig. 11.3 by the decrease in the difference between their calculated INDO energies. The difference is estimated to reach zero as the number of tetrahedra reaches about 10 or 12,

TABLE 11.4. Energy Difference between Chains and Rings

Number of Silica Tetrahedra	Cluster Size (Å)		INDO[a] (Chain–ring) (a.u.)	Hückel (Chain–ring) (eV)
	Rings	Chains		
2	6.567	9.090	8.90	24.86
3	7.143	12.671	5.88	−9.84
4	9.293	16.253	4.45	1.79
5	11.319	19.832	3.59	−17.67
6	11.88	23.414	2.76	4.44
⋮		⋮	⋮	
12		44.823	0.00	(Estimate)

[a] *Abbreviation used:* INDO, intermediate neglect of differential overlap.
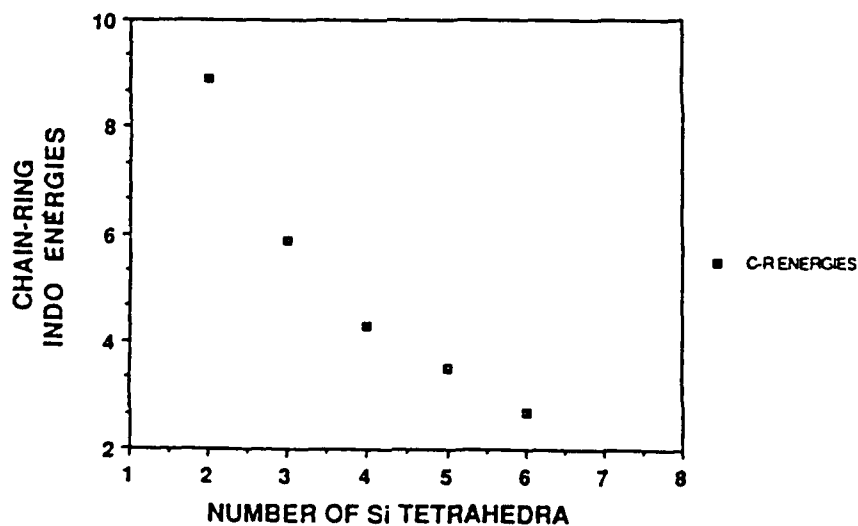

Figure 11.3. The relative stability of chains compared to rings as a function of the number of silica tetrahedra.

when the driving force for rings becomes more favorable than for chains. This result is similar to the size range where primary particle growth stops in acidic silica sols [10,11]. Acid catalysis ensures complete hydrolysis of the silica tetrahedra, as used in these calculations. The size of the INDO calculated rings or clusters for 10–12 tetrahedra appears to fall within the range of the radius of gyration of the primary particles calculated from small angle X-ray scattering analysis of acid-catalyzed silica sols [10,11].

As gelation occurs, the crosslinking of the structure becomes more dominant. Statistical analysis indicates that chain growth is limited by this process, and rings must be formed [12]. The energy differences in the ring structures in the INDO model are very small. This indicates that a broad distribution of ring sizes may be possible in a gel as they become energetically more favorable.

Tables 11.2 and 11.3 show the HOMO–LUMO bandgap energy and the associated theoretical UV cutoff. In both models the ring structures tend to yield a lower UV cutoff than the chain structures. Experimental UV cutoff values of dense dehydrated gel–silica are close to those predicted by the calculated ring structures [13] involving five tetrahedra per ring.

The effect of dopants on the UV cutoff is significant. The hydroxyl radical seems to have the most impact. The degenerate HOMO–LUMO bandgaps indicate that absorption is complete. In the case of the sodium dopant, this result tracks the experimental results of sol–gel soda–silica systems [4]. When the concentration of soda was increased from 0 to 7%, the UV cutoff increased by 105 nm from 200 nm to 305 nm. In the INDO model, as the sodium dopant was increased from 0 to 6.25%, the UV cutoff increased by 54.6 nm. Hydrogen-bonded water also increased the UV cutoff, as seen experimentally.

11.4. CONCLUSIONS

The HMO molecular orbital model is relatively simple and can be run on personal computers. The INDO model is more sophisticated and consequently more accurate; it also requires larger computational power, for example, Sun Microsystem. The differences in the INDO structural energies between rings and chains indicate that chain structures are the most stable up to about 10–12 silica tetrahedra. The calculated UV cutoffs in the pure silica is lower than the experimental values, however, ring structures with 5 tetrahedra are close to experimental values of pure gel–silica optics. Small concentration of hydroxyl, sodium, or water increases the UV cutoff wavelength, as expected.

ACKNOWLEDGMENTS

QUANTUM CALCULATIONS

REFERENCES

1. L. L. Hench, S. H. Wang, and J. L. Noques, *Multifunctional Materials*, SPIE Vol. 878, 76 (1988).

2. S. H. Wang, C. Campbell, and L. L. Hench, in: J. D. Mackenzie and D. R. Ulrich, Eds., *Ultrastructure Processing of Advanced Ceramics*, p. 145, Wiley, New York (1988).

3. R. V. Ramaswamy, T. Chia, R. Srivastava, A. Miliou, and J. West, *Multifunctional Materials*, SPIE Vol. 878, 86 (1988).

4. R. N. Li and L. L. Hench, in: C. J. Brinker, D. E. Clark, and D. R. Ulrich, Eds., *Better Ceramics Through Chemistry*, Vol. III, *Mat. Res. Soc. Symp. Proc.*, 589 (1988).

5. K. Sarnow, *Molecular Matters*, 80 Micro, pp. 100–107 (October 1983).

6. M. Zerner et al., Quantum Theory Project, Gainesville, Fl., Program No. 010183.

7. N. L. Allinger et al., QCPE, Bloomington, Indiana, Program No. 318.

8. L. L. Hench and J. K. West, in: *Principles of Electronic Ceramics*, Wiley, New York (in press).

9. L. W. Kelts, N. J. Effinger, and S. M. Melpolder, *J. Non-Cryst. Solids*, 83, 353 (1986).

10. G. Orcel, L. L. Hench, I. Artaki, J. Jonas, and T. W. Zerda, *J. Non-Cryst. Solids*, 105, 223 (1986).

11. B. Himmel, Th. Gerber, and H. Burger, *J. Non-Cryst. Solids*, 91, 122 (1987).

12. J. Zarzycki, in: L. L. Hench and D. R. Ulrich, Eds., *Science of Ceramic Chemical Processing*, p. 215, Wiley, New York (1986).

13. L. L. Hench, in: *Proceedings 4th Ultrastructure Processing Conference, Tucson, AZ, February 1989*.

SECTION VI

PROJECT D:
Biological Applications of Sol-Gel Science

An Investigation of Bioactive Glass Powders by Sol-Gel Processing

a. R. LI, A. E. Clark, and L. L. Hench

Advanced Materials Research Center, College of Dentistry, University of Florida, Alachua, Florida

Bioactive glass powders, with a composition of SiO_2-CaO-P_2O_5, have been successfully synthesized via a sol-gel process at considerably lower temperatures than required for conventional melting methods. Bioactive glass powders made via conventional methods form an interfacial bond with bone when they are implanted. Bonding is correlated with the formation of a surface hydroxyapatite layer. This study examined the formation of a hydroxyapatite layer in Tris-buffered solution as a function of SiO_2 content of sol-gel derived powders. A FT-IRRS technique was used to monitor the formation of the hydroxyapatite on the surface of the powders. X-ray diffraction analysis and BET were also used to characterize the chemical and physical properties of the sol-gel derived bioactive powders. It was discovered that: (a) the rate of hydroxyapatite formation decreased with increasing SiO_2 content for powders whose SiO_2 content was less than 90 mol%; (b) a hydroxyapatite film does not form for the powders whose SiO_2 content is more than 90 mol%; (c) the SiO_2 limit, beyond which the powders lost their bioactivity, was much higher for bioactive glass powders made through sol-gel process (90%) than those made by conventional melting methods (60%). These results indicate that it is possible to significantly expand the bioactive composition range through microstructural control made possible by sol-gel processing techniques.

INTRODUCTION

It is now well established that certain compositions of silicate-based glasses and glass–ceramic implants can bond to bone.[1-4] A common characteristic of these compositions is the presence of CaO, P_2O_5, Na_2O, and SiO_2 in the material. The bonding to bone has been associated with the formation of a hydroxyapatite (HA) layer on the surface of the implant.

It has also been shown that an even narrower range of glass compositions can bond to soft tissues.[5,6] A characteristic of the soft-tissue bonding compositions is a very rapid rate of HA formation. This has been previously attributed to the presence of Na_2O or other alkali cations in the glass composition which increases the solution pH at the implant–tissue interface and thereby enhances the precipitation and crystallization of HA.[7] The rate of HA formation has also been shown to be very strongly dependent on the ratio of SiO_2, glass network former, to Na_2O, network modifier, in the glass.[8] When the glass composition contains 60% SiO_2, or more, bonding to tissues is no longer observed.

Up to the present time, bioactive glasses have been produced using conventional glass technology. The glass components in the form of grains of oxides or carbonates

are mixed and then melted and homogenized at high temperatures, 1250–1400°C. The molten glass is then cast into steel or graphite molds to make bulk implants. A final grind and polish is often necessary to achieve required tolerances.

For some clinical applications, such as treatment of periodontal lesions[9] or urinary incontinence[10], powders of the bioactive glasses are required. With conventional glass processing, powders are made by pouring the molten glass into a liquid medium, such as water, fracturing the frozen glass into small fragments. Subsequent grinding and size separation steps are necessary to achieve powders with specific size ranges, such as 90–710 μm, required for periodontal treatment.

There are several disadvantages of these conventional glass processing methods for bioactive glasses:

(1) It is difficult to maintain the very high purity required for optimal bioactivity. This is primarily because of the high temperatures associated with melting and homogenization, but is also related to the low silica and high alkali content of the traditional bioactive glass compositions. These compositions are very reactive chemically and tend to dissolve even platinum and can easily pick up other multiple cations as impurities. Gross and Strunz[11] have shown how sensitive tissue bonding is to M^{3+}, M^{4+}, and M^{5+} impurity cations in bioactive glass–ceramics. Greenspan and Hench[12] have shown that a small amount of Al^{3+} can completely eliminate bone bonding for bioactive glasses. Recently Kitsugi and colleagues[13] and Kokubo and coworkers[14] have shown similar compo-

sitional sensitivities in other bioactive glass and glass–ceramic systems.

(2) Process steps of grinding, polishing, fritting, sieving, etc., all expose a bioactive powder to potential contaminants and the negative effects on bioactivity described above.

(3) There is a compositional limitation imposed on bioactive glasses and glass–ceramics made by conventional high-temperature processes. This is due to the extremely high equilibrium liquidus temperature of SiO_2, 1713°C, and the extremely high viscosity of silicate melts with high SiO_2 content.

(4) High-temperature processing in platinum crucibles and multiple handling steps also increase production costs considerably. The additional costs are not only in energy, but also in capital equipment, labor, maintenance, quality assurance, quality control, etc. Lowering the processing temperature lowers such costs considerably.

Low-temperature sol-gel processing offers an alternative to conventional glass and glass–ceramic processing with the potential advantages indicated above.

The sol-gel process has become a widely spread research field during the last decade.[15-17] Basically, the process involves the synthesis of an inorganic network by mixing the metal alkoxides in solution, followed by hydrolysis, gelation, and low-temperature firing to produce a glass. Inherent in this process is the ability to modify the network structure through controlled hydrolysis and polycondensation reactions.[18,19] Thus, structural variation can be produced without compositional changes. Because the glasses can be prepared from gels by sintering at relatively low temperatures (600–700°C), most of the disadvantages of high-temperature processing can be eliminated with much higher control over purity. Also, sol-gel processing offers potential advantages of ease of powder production, a broader range of bioactivity, and a better control of bioactivity by changing either the composition or the microstructure through processing parameters.

Thus, the objectives of this work are: (a) synthesize bioactive gel powders through sol-gel processing by controlling the hydrolysis and polycondensation reactions; (b) eliminate Na_2O from the compositions by taking advantage of low-temperature mixing of $CaO-P_2O_5-SiO_2$ sols; (c) determine the compositional dependence (SiO_2 content variation) of the formation of hydroxyapatite; and (d) compare the bioactivity range of melt-derived bioactive glasses with the bioactive gel powders made through sol-gel processing.

EXPERIMENTAL PROCEDURE

Table I shows the compositions of $CaO-P_2O_5-SiO_2$ gel powders investigated in the present studies. The samples

TABLE I. Compositions of Gel Powders (mol%)

Sample	SiO_2	P_2O_5	CaO
49S	50	4	46
54S	55	4	41
58S	60	4	36
63S	65	4	31
68S	70	4	26
72S	75	4	21
77S	80	4	16
81S	85	4	11
86S	90	4	6
90S	95	4	1

were prepared from tetraethyoxysilane (TEOS), triethyl phosphate [$OP(OEt)_3$], and calcium nitrate [$Ca(NO_3)_2 \cdot 4H_2O$]. Nitric acid was added to accelerate the hydrolysis reaction of TEOS. After mixing the components, the sol was cast into a polyethylene container and placed inside an oven at 60–180°C where the sol was gelled, aged, and dried. The dried gels were heated in a silica crucible at a temperature range of 600–700°C for several hours in a nitrogen atmosphere. The material then was ground into powders with a particle size range of 100–700 μm.

Previous studies indicate that the essential condition for a material to bond with bone is the formation of the surface hydroxyapatite layer in the body environment. Therefore, the powders made as described above were subjected to an *in vitro* solution test to evaluate the potential bioactivity of the material. In the *in vitro* test procedure, the gel powders were reacted with a Tris-buffered solution (pH = 7.2 ± 0.1) at 37°C for various times. The resultant reacted powders were then examined by Fourier Transform Infrared Reflection (FTIR) Spectroscopy on a Nicolet 20SXB Spectrometer with a diffuse reflectance stage between 1400 and 400 cm^{-1}. Also, to ensure that the gel powders did not undergo any reaction prior to the *in vitro* testing, unreacted powders were tested by FTIR.

There are several solution test procedures which can be used for powders.[20] The one which gave a more reliable and reproducible result for the bioactive gel powders is dynamic rather than static. In this study, powders were poured directly into the Tris-buffered solution in a Nalgene container and agitated in an incubator shaker for the reaction times indicated. This shaker is designed to deliver orbital motion in a controlled temperature environment. The operating temperature remained at 37°C ± 1°C and the spinning rate was 220 rpm. This dynamic test procedure allowed the reacting solution to surround and react with the powders continuously.

X-ray diffraction (XRD) was used to study the powders after heating between 600 and 700°C and after reaction in the *in vitro* test solution. The XRD range was from 5° to 85° 2θ at a rate of 3°/min, using Cu-Kα radiation at 40 KV. A Quanta Chrome Autosorb-6 was employed to measure the surface area and pore size distributions of the samples using N₂ as an absorbent.

RESULTS

Conventionally produced bioactive glasses, such as 45S5 Bioglass® (Copyrights, University of Florida, Gainesville, FL 32611) contain sodium oxide as one of the components necessary to develop bioactivity. With the glasses derived by sol-gel method, bioactivity could be achieved with sodium absent from the composition, reducing the glass from a four to a three component system.

Figure 1 shows the x-ray diffraction spectra of the gel powders after the dried gels had been heated between 600 and 700°C for 3 h. The x-ray diffraction spectrum of a standard bioactive glass (45S5 Bioglass") is also shown

in Figure 1 for comparison. The melt-derived glass shows no x-ray diffraction lines, only a very broad peak characteristic of an amorphous solid. The 49S, 54S, and 58S sol-gel derived powders show a very small amount of crystallinity. All the other sol-gel compositions show complete amorphous x-ray spectra. Figure 2 shows the FTIR spectrum of gel powders before the reaction *in vitro*. Figures 3 and 4 show the diffuse reflectance spectra of the various sol-gel derived powders at early stages of the *in vitro* reaction (1 and 8 h, respectively).

The peak at 1095 cm^{-1} in the FTIR spectra is assigned as a Si-O-Si stretching vibration.[21,22] The peak at 482 cm^{-1} is assigned as a Si-O-Si bending mode. The peaks at
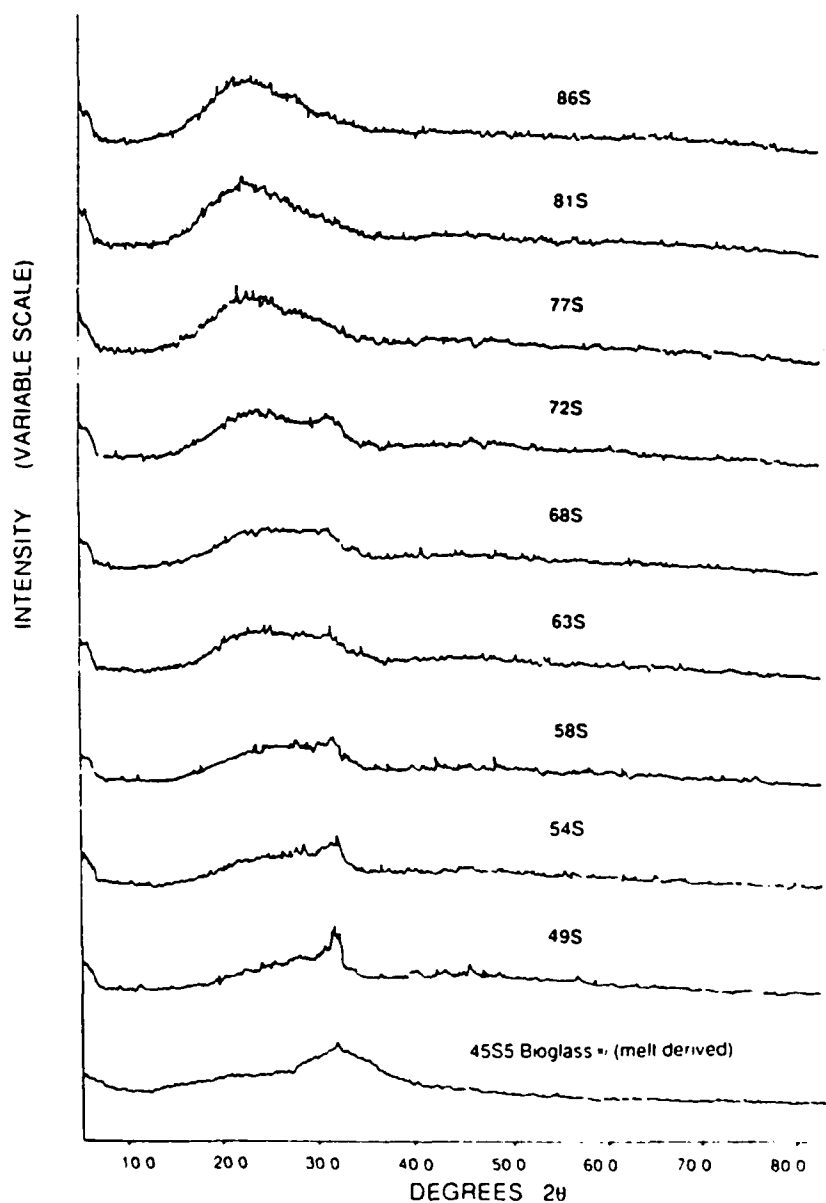

Figure 1. The comparison of x-ray diffraction data of the bioactive gel powders listed in Table I after heating to 600 C and 45S5 Bioglass" by standard melting and casting
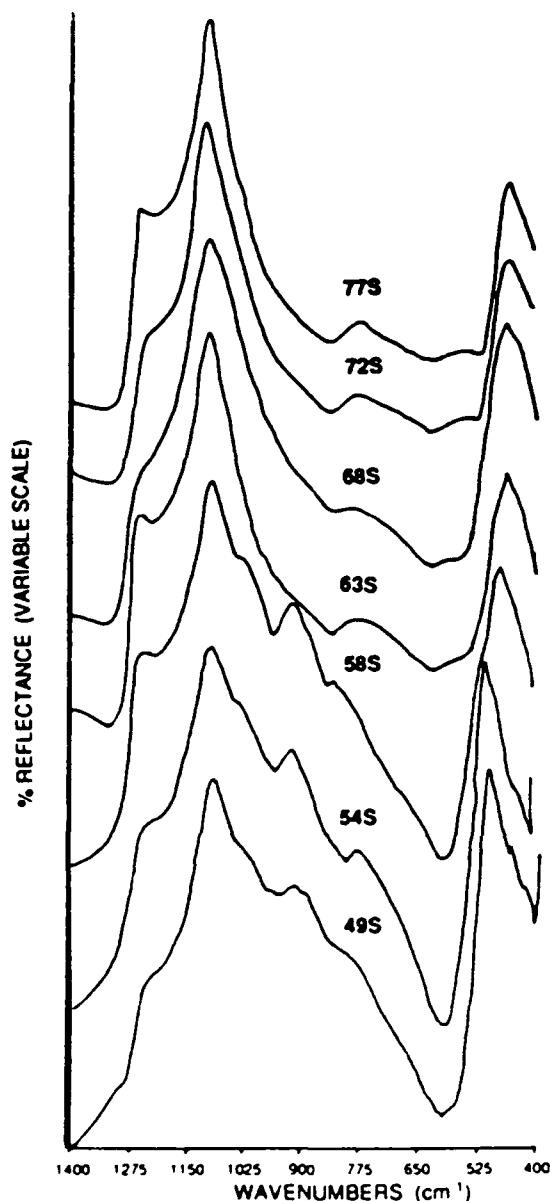
Figure 2. FT-IRRS spectra of gel powders with various composition before reaction.

Figure 3. FT-IRRS spectra of gel powders with various composition after 1 h.

598 cm^{-1} and 566 cm^{-1} are assigned as P–O bending vibrations in [PO$_4$] tetrahedra.[23] These two peaks are characteristic of a hydroxyapatite crystalline phase.

Figure 5 shows the time-dependent increase in intensity of the spectra of hydroxyapatite peaks for 58S composition. Figure 6 compares the FTIR spectra of two melt-derived glass powders, 45S and 60S after 20 h *in vitro* reaction and Figure 7 is the comparison of the x-ray diffraction spectra of 58S bioactive gel powders and 45S5 Bioglass® after different reaction times.

DISCUSSION

Conventional bioactive glasses contain less than 60 mol% SiO$_2$, have high Na$_2$O and CaO content and a high Ca/P

ratio, e.g., 45S5 Bioglass® contains 24.5% Na$_2$O, 24.5% CaO (in weight %), and a Ca/P ratio of 5.2. When bioactive glass is exposed to water or body fluids several key reactions occur. There is a cation exchange of Na^{+1} and Ca^{+2} cations from the glass for protons in the solution, producing hydrolysis of the surface silica group (silanols). The cation exchange also increases the hydroxyl concentration of the solution which leads to attack of the silica glass network producing additional silanol formation and controlled interfacial dissolution. As the interfacial pH becomes more alkaline, the hydrolyzed surface silanol groups repolymerize, producing a silica-rich surface layer. Another consequence of the alkaline pH at the glass solution interface is that CaO and P$_2$O$_5$,
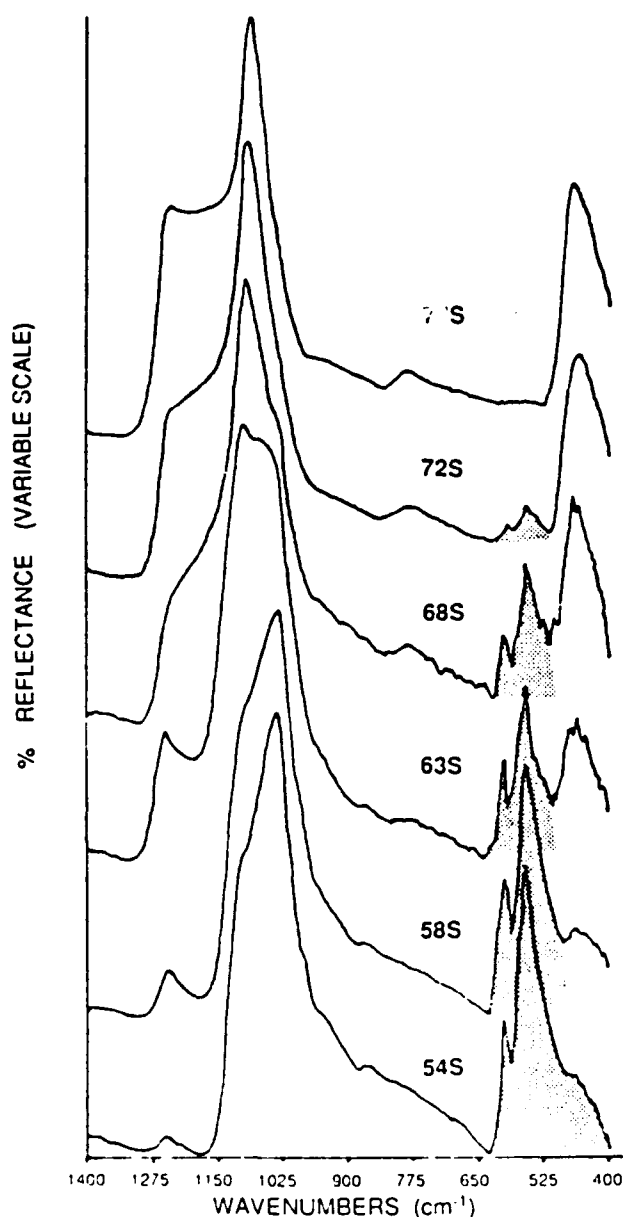
Figure 4. FT-IRRS spectra of gel powders with various composition after 8 h.

approaches and exceeds 60 mol%, the rates of network dissolution and hydroxyapatite crystallization are retarded and the bioactivity is reduced and eventually eliminated. After reaction, Figure 6 shows that a pair of hydroxyapatite peaks is present for the FTIR spectrum from the 45S5 glass surface. These peaks grow as the broad Si-O-Na and Si-O-Ca peak, shown for 45S5 before reaction, disappears. The 45S5 Bioglass® (45 wt% SiO_2) is very bioactive and bonds to both hard and soft tissues. In contrast, the 60S melt-derived composition (60 wt% SiO_2) does not develop an apatite layer, even after several weeks in solution. This composition is not bioactive and does not bond to bone or soft tissues. Therefore, the maximum SiO_2 content of bioactive melt-derived glasses is 60 mol%.

The gel powders made by sol-gel process contain no Na_2O. The spectra of unreacted samples show that there are only silica and silica plus alkaline earth vibrational peaks from 1400 to 400 cm^{-1} before reaction in the solution (Fig. 2). With a reaction time of only 1 h, the peaks at 598 cm^{-1} and 566 cm^{-1} increase their intensities for most compositions, indicative of the formation of an HA phase on the surface. No hydroxyapatite crystal is found for 77S within 1 h. The intensities of the characteristic hydroxyapatite peaks decrease with increasing SiO_2 content in the one hour test (Fig. 3).

The Si-O-Si rocking vibration peak at 482 cm^{-1} is diminished in the 54S and 58S samples after 8 h reaction in the solution (Figure 4). Because of the very small penetration depth of the IR beam (<1 μm), the hydroxyapatite peaks developed on the gel-glasses (Figs. 3–5) must be due to a surface layer of HA formed on the powders. This is confirmed by XRD (Fig. 7). The 58S gel powders show strong x-ray diffraction peaks which index as hydroxyapatite after only 8 h reaction in vitro, whereas the melt-derived 45S5 bioactive glass requires more than 100 h to demonstrate sharp HA lines. Otner instrumental techniques have confirmed this interpretation both in vitro and in vivo. In Figure 8, the rate of formation of the hydroxyapatite layer is compared for different compositions of the gel-glass powders. The comparison is made by obtaining a ratio of peak intensities of FT-IRRS spectra. The intensity of each peak was measured relative to the intensity between 470 and 610 cm^{-1}. I_1 refers to the intensity of P-O bending vibration at about 566 cm^{-1} and I_2 refers to Si-O-Si bending vibration at about 482 cm^{-1}. A ratio was calculated of the apatite peak intensity divided by the silica peak intensity, I_1/I_2. The plot of I_1/I_2 as a function of time shows that HA formation is delayed with the increasing of SiO_2 content at early stages. The data of Figure 8 suggest that the compositional limit of formation of HA on the gel-glasses is approximately 72% SiO_2. However, if the exposure time is increased to 7 days, HA formation is demonstrated for the gel powder with up to 90 mol% silica (86S) (Fig. 9). It should be noted that while the silica compositional limit for HA formation is extended, the
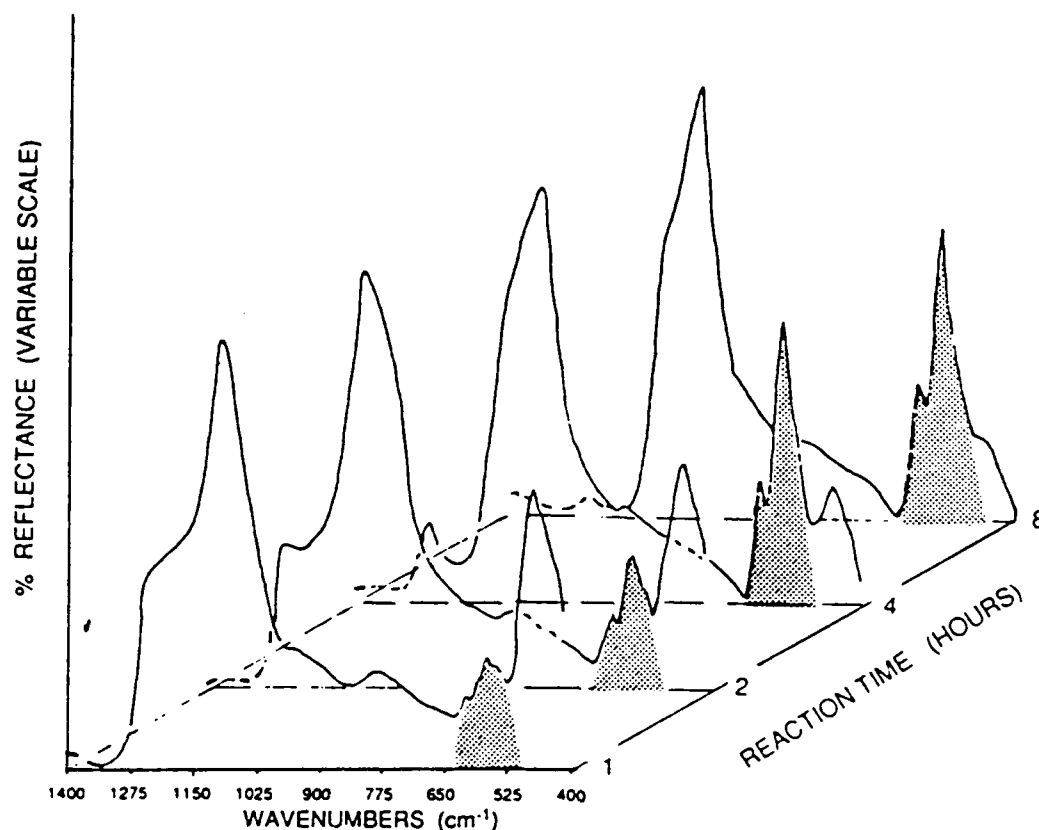
which have been released into solution during network dissolution, crystallize into a mixed hydroxy-carbonate apatite on the surface. The crystallites of the HCA phase are proposed to bond to interfacial metabolites such as mucopolysaccharides and collagen. It is hypothesized that this incorporation of organic biological constituents within the growing HCA- and SiO_2-rich layers appears to be the initial step in establishing bioactivity and bonding to tissues.

Studies have shown that there is a minimum rate of hydroxyapatite formation which is necessary to achieve bonding with hard tissues. Both the glass composition and the microstructure exert an influence on the development and growth of the HCA phase. As the SiO_2 content of the melt-derived bioactive glasses

Figure 5. FT-IRRS spectra of 54S gel powders with various reaction times.

A possible explanation for the extension of the compositional boundary for bioactivity is the presence of very small pores and large surface areas of the sol-gel derived powders (Table II). The surface area of all the sol-gel derived compositions range from 200 to 650 m^2/g and the total pore volume range between 0.3 and 0.6 cm^3/g as determined by Autosorb-6 analysis. These ultrastructural features may give rise to an increased density of potential nucleation sites that result in the formation of the hydroxyapatite layer on the surface of the gel-derived powders. Previous investigations[25] of melt-derived Bioglasses show that bonding with bone *in vivo* occurs within 10 to 30 days if the surface area developed in simulated test solutions is the range of 200–500 m^2/g. In contrast, compositions of glass that do not bond to bone and

Figure 6. FT-IRRS spectra for 45S5 Bioglass and 60S by melting method, after 20 h reaction.

kinetics of HA formation are retarded as the CaO and P$_2$O$_5$ content of the gel-glasses is varied. These results indicate that it is possible to extend the compositional boundary for bioactivity up to 90 mol% SiO$_2$ by making use of sol-gel processing.

TABLE II. BET Data of Bioactive Gel Powders

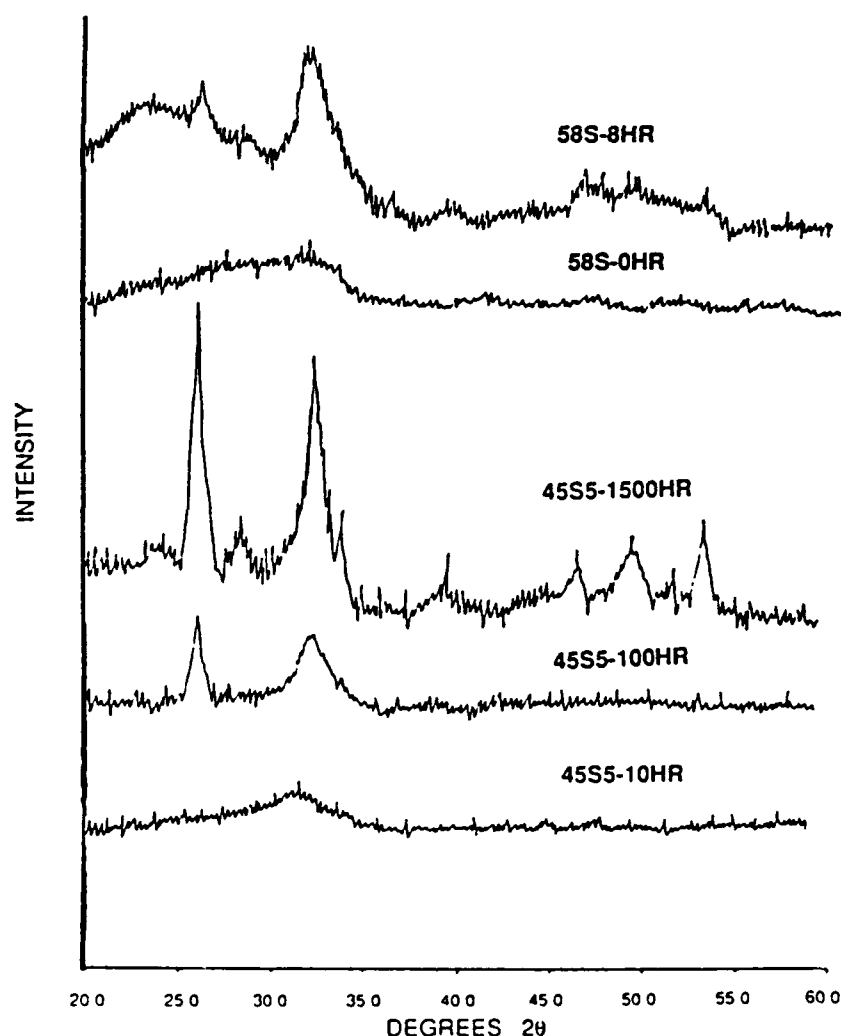|	Surface Area (m^2/g)	Total Pore Volume (cm^3/g)	Average Pore Size (Å)
49S	203	0.57	57
54S	213	0.53	50
58S	289	0.49	34
63S	324	0.44	27
68S	326	0.41	25
72S	380	0.38	20
77S	431	0.32	15
81S	547	0.37	14
86S	627	0.45	14

Figure 7. The comparison of x-ray diffraction data of the 58S bioactive gel powders and 45S5 Bio-glass* by standard melting after different reaction times.
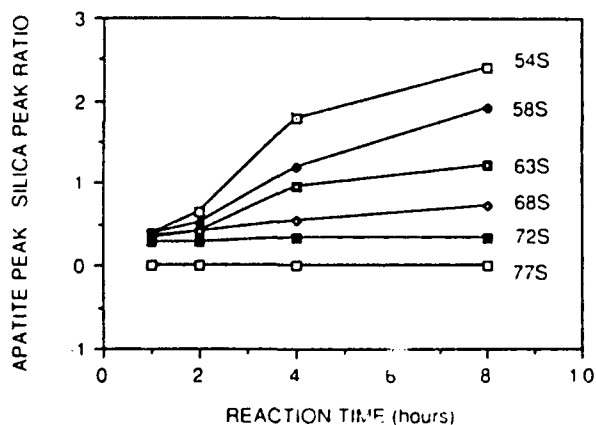

Figure 8. Rate of formation of hydroxyapatite at early stage for some bioactive gel powders.

powders will be highly bioactive since their initial surface areas are high. The exposure to the Tris-buffered solution increases the surface area even more. Thus the compositional range of bioactivity has been extended significantly through sol-gel-derived gels. This extended compositional range of HA formation and presumably bioactive bonding is summarized on Figure 10.

CONCLUSION

(1) Alkali-free bioactive $CaO-P_2O_5-SiO_2$ gel powders which can form a hydroxyapatite layer when exposed to Tris-buffered solution have been synthesized using low temperature sol-gel processing.

(2) The rate of formation of hydroxyapatite, which is an indicator of bioactivity, varies with the composition of the gel powders. Gel powders, which have lower SiO_2 content and higher CaO and P_2O_5 content, exhibit higher rates of HA formation.

are not bioactive develop less than 0.1 m²/g surface area when exposed to simulated test solutions. Consequently, it is concluded the sol-gel derived $CaO-P_2O_5-SiO_2$ gel
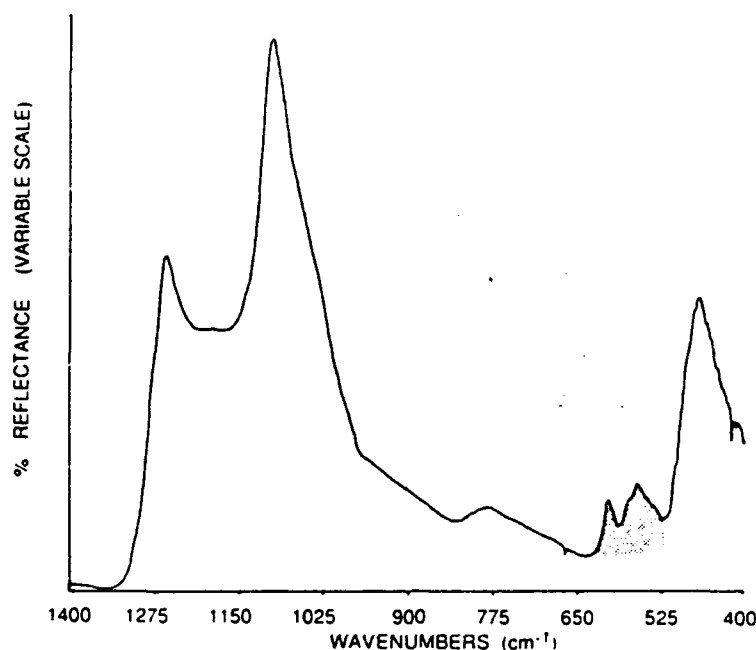
Figure 9. FT-IRRS spectrum for 86S bioactive gel powder after 7 days reaction in simulated *in vivo* solution.
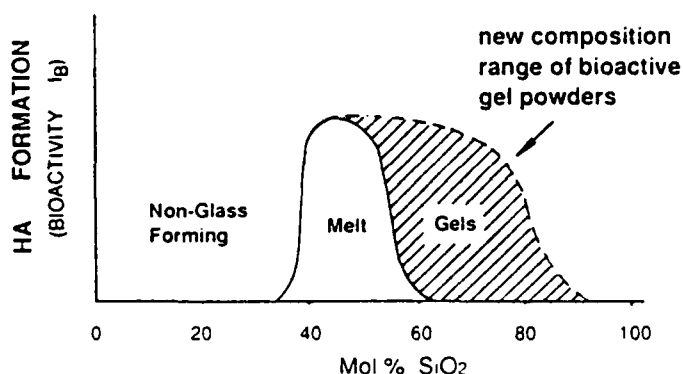

Figure 10. The difference in range of bioactivity for the bioactive gel vs. melt-derived Bioglasses[*].

(3) The compositional boundary of HA formation has been significantly extended through sol-gel de-rived bioactive gel powders over the melt-derived Bioglass[*] powders. The upper limit is approximately 90 mol% SiO_2.

NIDR, P50DE09307-01; AFOSR, 49620-88-C-0073.

REFERENCES

1. Hench, L. L.; Splinter, R. J.; Greenlee, T. K.; Allen, W. C. Bonding mechanisms at the interface of ceramic prosthetic materials. J. Biomed. Mater. Res. 2:117; 1971.
2. Hench, L. L.; Ethridge, E. C. Biomaterials—An Inter-facial Approach. New York: Academic Press; 1982.
3. Hench, L. L.; Clark, A. E. Biocompatibility of Orthopedic Implants. Williams, D. F. ed., Boca Raton:CRC Press; 1982:Vol. 2. Chap. 6.
4. Hench, L. L. Fundamental Aspects of Biocompatibility. Williams, D. F. ed. Boca Raton:CRC Press; 1982; Vol. 1, Chap. 4.
5. Wilson, J.; Pigott, G. H.; Schoen, F. J.; Hench, L. L. Toxi-cology and biocompatibility of bioglasses[x]. J. Biomed. Maters. Res. 15:805; 1981.
6. Wilson, J.; Merwin, G. E.; Rodgers, L.W.; Martin, R. G.; Spilman, D. Facial bone augmentation using Bioglass in dogs. Biological and Biomechanical Performance of Bio-materials, Christel, P.; Meunier, A; Lee, A. J. C. eds. Amsterdam: Elsevier; 1963:93.
7. Clark, A. E. Solubility and biocompatibility of glass, Gainesville:Univ. Florida; 1974. Dissertation.
8. Hench, L. L. Bioactive ceramics. Bioceramics: Material Characteristics Versus In Vivo Behavior, Ducheyne, P.; Lemons, J. E. eds. New York:The New York Academy of Sciences; 1988:54.
9. Wilson, J.; Low, S.; Fetner, A.; Hench, L. L. Bioactive Materials for Periodontal Treatment—A Comparative Study in Biomaterials Clinical Applications. Pizzoferrato, A.; Marchetti, P. G.; Ravaglioli, A.; Lee, A. J. C. eds. Amsterdam:Elsevier. 1987:223.
10. Ramer, M. Bioglass[*]—hylan suspension for treatment of urinary incontinence. Gainesville: Univ. Florida; 1990. MS Thesis.
11. Gross, U. M.; Strunz, V. The anchoring of glass ceramics of different solubility in the femur of the rat. J. Biomed. Mater. Res. 14:607; 1980.
12. Greenspan, D; Hench, L. L. Chemical & mechanical be-havior of Bioglass coated alumina. J. Biomed. Mater. Res. 10:503; 1976.
13. Kitsugi, T.; Yamamuro, T.; Nakamura, T.; Kotani, S.; Kokubo, T.; Effects of varying amounts of Al_2O_3 on the bond between A-W glass ceramics and bone. Oonishi, H.; Aoki, H.; Sawai, K. eds. Bioceramics, Vol. 1. Ishiyaku Euro America Inc.; 1989.
14. Kokubo, T.; Ito, S.; Huang, Z.T.; Hayashi, T.; Sakka, S.; Kitsugi, T.; and Yamamuro, T. Ca, P-rich layer formed on high-strength bioactive glass-ceramic A-W. J. Biomed. Mater. Res. 24:331; 1990.

15. Sakka, S. Glasses and glass-ceramics from gels, J. Non-Cryst. Solids 73:651; 1985.
16. Zarcycki, J. Processing of gel glasses. Uhlman, D. R., Kreidl, N. J. eds. Glass Science and Technology. Vol. 2, 209.
17. Orgaz-Orgaz, F. Gel to glass conversion: Densification kinetics and controlling mechanisms. J. Non-Cryst. Solids 100:115; 1988.
18. Brinker, C. J.; Scherer, G.W. Sol-gel glass: I. Gelation and gel structure. J. Non-Cryst. Solids 70:301; 1985.
19. Pope, E. J. A.; Mackenzie, J. D.; Sol-gel processing of silica. II. The role of the catalyst. J. Non-Cryst. Solids 87:185; 1986.
20. Warren, L.; Clark, A. E.; Hench, L. L. Quality assurance of Bioglass powders. J. Biomed. Mater. Res. Appl. Biomater. 23(A2):201; 1989.
21. Bell, R. J.; Dean, P. Atomic vibrations in vitreous silica. in Discuss. Faraday Soc. 50:55; 1970.

22. Gaskell, P. H. Vibrational spectra of simple silicate glasses. Discuss. Faraday Soc. 50:82; 1970.
23. Fowler, B. O. Infrared studies of apatites, I. Vibrational assignments for calcium, strontium and barium hydroxyapatites utilizing isotopic substitution. Inorg. Chem. 13:194; 1974.
24. Ogino, M.; Hench, L. L. Compositional dependence of the formation of calcium phosphate films on Bioglass™. J. Biomed. Mater. Res. 14:55; 1980.
25. Walker, M. M. An investigation into the bonding mechanisms of Bioglass™. Gainesville: Univ. Florida; 1977. MS Thesis.

b. **The Kinetics of Bioactive Ceramics Part III: Surface Reactions for Bioactive Glasses compared with an Inactive Glass**

L.L. Hench, Ö.H. Andersson* and G.P. LaTorre

Advanced Materials Research Centre, University of Florida, One Progress Blvd, Alachua, FL 32615, U.S.A and
* Department of Chemical Engineering, Åbo Akademi University, Biskopsgatan 8, SF-20500 Åbo, FINLAND.

ABSTRACT

Reactions that produce a biologically equivalent hydroxyl-carbonate apatite layer on an implant surface lead to adherent tissue bonding and "bioactive fixation". The effects of various compositional factors, such as SiO_2/ alkali ratio, CaO/P_2O_5 ratio, Al_2O_3 and B_2O_3 content, and CaF_2/CaO ratio, on the sequence and rates of surface reactions of various bioactive glasses are measured using Fourier Transform Infrared Reflection Spectroscopy. Five stages of reaction are identified. The rate of silica polycondensation of surface silanol groups (Stage 3) appears to control the rate of formation of an amorphous calcium phosphate layer (Stage 4) and its crystallization into hydroxyl-carbonate apatite (HCA) (Stage 5). Increasing SiO_2 content of the glass from 45 to 53% slows down HCA crystallization by 40X; increasing to 63% stops HCA formation altogether.

INTRODUCTION

The bonding of bioactive ceramics to tissues is a time dependent kinetic phenomena. As discussed in Parts I and II of this series of papers (1,2) there are six stages of interfacial reactions that describe the chemical changes occurring on the biomaterial side of the bond:

Stage (1)   *Rapid exchange of Na^+ or K^+ with H^+ or H_3O^+ from solution,*

$$Si\text{-}O\text{-}Na^+ + H^+ + OH^- \rightarrow Si\text{-}OH + Na^+_{(solution)} + OH^-$$
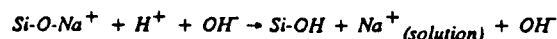
Stage (2)   *Loss of soluble silica in form of $Si(OH)_4$ to the solution resulting from breakage of Si-O-Si bonds and formation of Si-OH (silanols) at the glass solution interface.*

$$2(Si\text{-}O\text{-}Si) + 2(OH^-) \rightarrow Si\text{-}OH + OH\text{-}Si$$
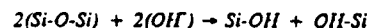
Stage (3)   *Condensation and repolymerization of a SiO_2-rich layer on the surface depleted in alkalis and alkaline earth cations.*

$$2(Si\text{-}OH) + 2(OH\text{-}Si) \rightarrow \text{-}Si\text{-}O\text{-}Si\text{-}O\text{-}Si\text{-}O\text{-}Si\text{-}O\text{-}$$
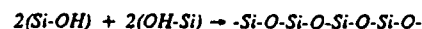
Stage (4)   *Migration of Ca^{2+} and PO_4^{3-} groups to the surface through the SiO_2 rich layer forming a CaO-P_2O_5-rich film on top of the SiO_2-rich layer, followed by growth of the amorphous CaO-P_2O_5-rich film by incorporation of soluble calcium and phosphates from solution.*

Stage (5)   *Crystallization of the amorphous CaO-P_2O_5 film by incorporation of OH^-, CO_3^{2-}, or F anions from solution to form a mixed hydroxyl-carbonate, apatite layer (HCA) or hydroxyl-carbonate fluorapatite (HCFA) layer composed of small crystallites.*

Stage (6)   *Agglomeration and chemical bonding of biological moieties within the growing HCA layer leading to incorporation of collagen fibrils produced by osteoblasts or fibroblasts.*

82

The consequence of this sequence of reactions is the creation of an interfacial bonding zone between tissue and the bioactive glass implant that is a 30-μm layer of hydroxyl carbonate apatite (HCA) crystals on top of a 100 to 120 μm layer rich in SiO_2. The thickness of both layers depends considerably on composition of the implant, time after implantation, and surgical fit of the implant. Electron and optical micrographs reviewed in refs. 3 and 4 show the direct bonded interface between the bone of many species and several bioactive glass and glass-ceramic implants from 7 to 365 days after implantation.

The rates of these stages are dependent upon composition of bioactive glass or glass-ceramic, as discussed in Parts I and II and refs. 4-5. The three compositions reported previously are given in Table 1. The most significant difference observed in Part II was a delay in the onset of crystallization of the amorphous calcium phosphate layer to a well ordered crystalline phase (Stage 5) for a bioactive glass containing B_2O_3 and a lower calcium/phosphorous ratio (glass #10).

The objective of this paper is to: 1) repeat the previous experiment on the reaction sequence of the 45S5 composition using a Nicolet 20 SBX Fourier Transform IR Spectrometer. The previous paper (Part II) used data obtained several years ago by Kim, et al. with an older FTIR. Also previous work did not look for precise information on the time change between reaction stages. The second objective is to compare Stages 1-5 of the new data on 45S5 with the previous studies by Kim, et al. (6) and the authors (2). A third objective is to extend the compositional dependence of the kinetic studies to include bioactive glass #9 and the non-bonding glass #1 from Andersson's investigations (7). Thus the relationship between the glass surface reaction sequence (Stages 1-6) and implant bonding behavior should be obtained.

Table 1 shows that glass #9 has substantially more SiO_2 content than the other glasses previously investigated. However, the Na_2O content is nearly the same. There is also a somewhat lower CaO and P_2O_5 content for the glass. Composition #1 has an even greater SiO_2 content of 63.5% with a substantially reduced Na_2O and CaO content. Previous investigations of compositions with this large amount of SiO_2 indicate that the glass is outside the bone bonding boundary (5). Push-out studies by Andersson and co-workers have shown that glass #1 does not bond to canine bone within eight weeks (8). However, glass #9 does bond within seven weeks (9). The strength of bonding of glass #9 at seven weeks is in the order of 20 MPa, equivalent to that of glass #10 at the end of eight weeks. The variability in push-out strength is such that there is no statistical difference between push-out strength of glasses #9 and #10. Previous work has shown that 45S5.4F and 45S5 bioactive glass bonds to bone with high strengths within four weeks (3,10).

Table 1
Glass Compositions by Synthesis wt%.

Designation	SiO_2	Na_2O	CaO	CaF_2	P_2O_5	B_2O_3	Al_2O_3
45S5.4F	43.300	23.640	14.150	13.130	5.770	0.000	0.000
45S5	44.970	24.550	24.490	0.000	5.990	0.000	0.000
#1(S63.5P6)	63.500	15.000	14.000	0.000	6.000	0.500	1.000
#9(S53P4)	53.000	23.000	20.000	0.000	4.000	0.000	0.000
#10(S45P7)	45.000	24.000	22.000	0.000	7.000	2.000	0.000

EXPERIMENTAL METHOD

The glasses listed in Table 1 were reacted at 37°C in tris buffer solution with a surface area to volume ratio 0.1 cm^{-1} with procedures equivalent to that of Kim, et al. (6). The surface films formed during reaction were analyzed with the Nicolet SXB with a diffuse reflection attachment. The time periods studied are shown in the figures.

EXPERIMENTAL RESULTS

45S5: The FTIR spectra of the 45S5 glass are shown before reaction (t=0) and after completion of Stages 1-4 at 90 mins. (Fig. 1A) and after completion of Stage 5 (Fig. 1B) at 120 mins. The peak assignments are listed on the spectra in Fig. 1B and are discussed in ref. 6. The time dependent changes in the Si-2NBO stretching vibration associated with Stages 1 and 2 is plotted in Fig. 2. The frequency of this vibration mode decreases from 930 cm^{-1} at the onset of the surface reaction and by 10 mins., Table 2, has been replaced by a newer lower frequency mode assigned to the Si-O-Si bond vibration between two neighboring SiO$_4$ tetrahedra. The wave-number for this new mode is approximately 840 cm^{-1}. With time this mode also continues to decrease in frequency throughout the reaction sequence, finally reaching a value as low as 720 cm^{-1}. This new mode corresponds to formation of the network of the silica gel layer produced by a condensation reaction between neighboring surface silanol groups, e.g. as shown in eq. (1).

$$SiOH + SiOH = Si - O - Si + H_2O \tag{1}$$

Eventually the Si-O-Si stretching mode is masked by the growing apatite layer.

Figure 2 also shows that the Si-O-Si bending vibration at 495 cm^{-1} continuously decreases through reaction Stages 1-3. However, in Stage 4 there is a slight increase in the vibration until Stage 5 is reached when there is a sharp decrease prior to the vibrational mode being completely masked by the crystallizing hydroxyl-carbonate apatite layer.

Table 2
Time for Onset of Reaction Stages 1, 2, 3, 4 and 5.

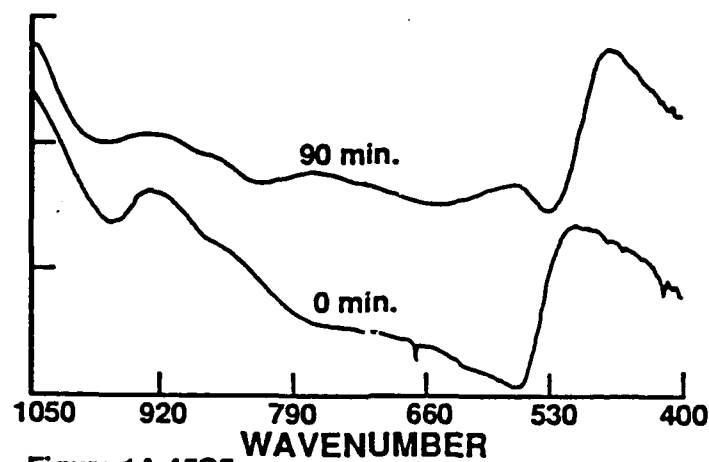| Composition	Time (Min)										
	1	2	10	20	40	90	120	360	720	1440	4320
45S5.4 (2)	1+2		3+4				5				
45S5 (old) (2)	1+2				3+4		5				
45S5 (new)	1+2		3+4				5				
Composition #1 (S63.5P6)	NO SPECTRAL CHANGES NOTED										
Composition #9 (S53P4)	1+2					3		4			5
Composition #10 (2) (S45P7)	1+2			3+4				5			

Figure 1A 45S5
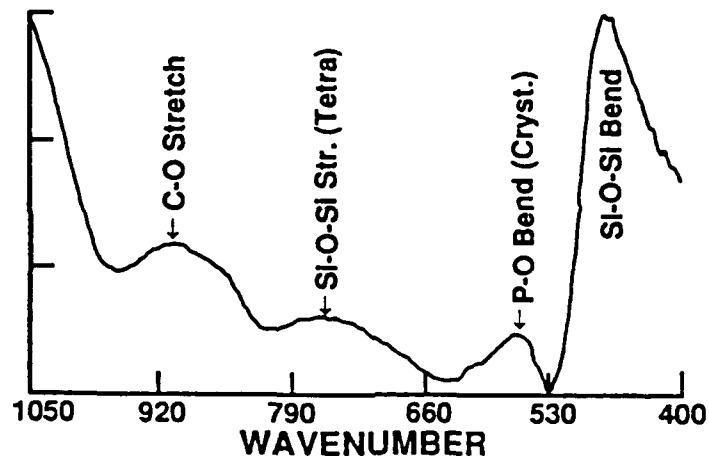

Figure 1B 45S5 120 Min.
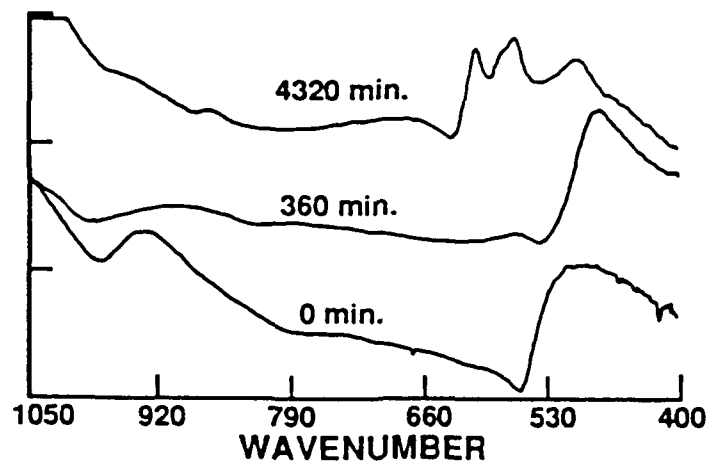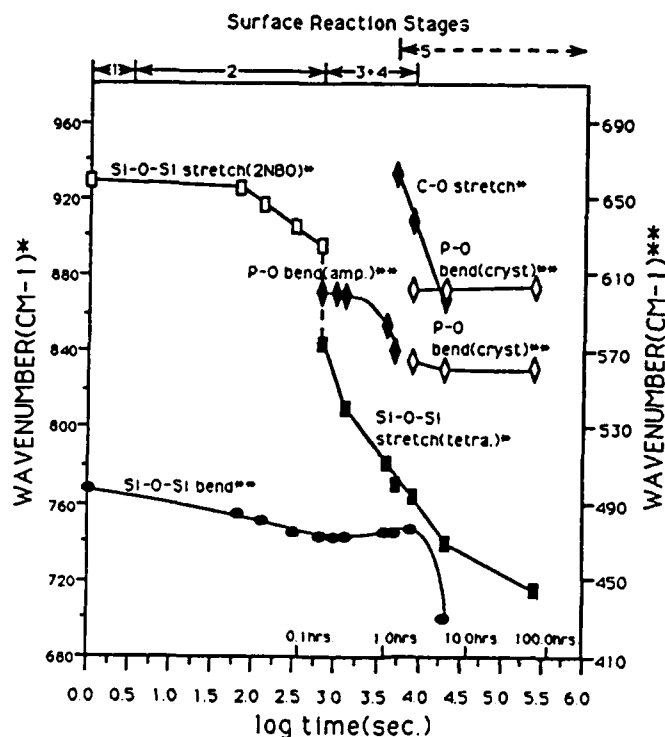

Figure 1C Comp #9 (S53P4)

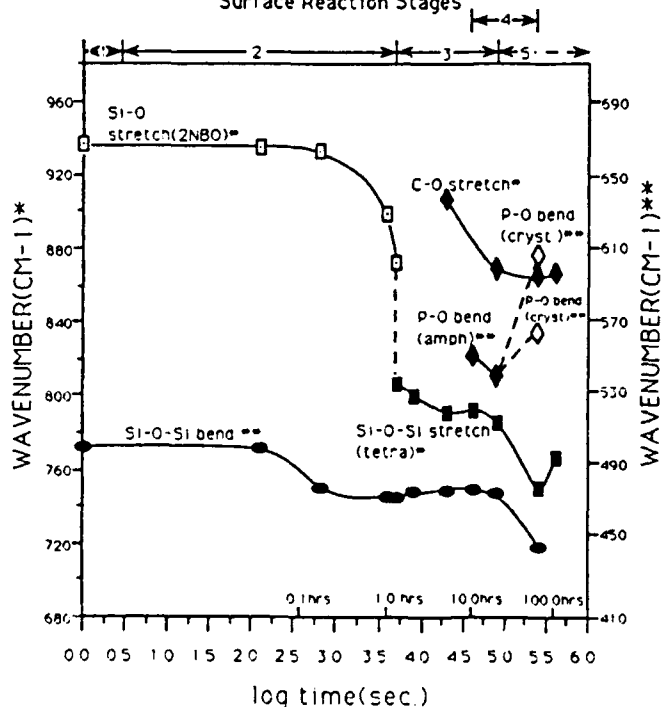Figure 2 : Wavenumber verses time for 45S5(rerun on SXB)

Figure 3 : Wavenumber verses time for OA composition #9

One of the most distinctive features of the surface reactions is the onset of P-O bending vibrations from an amorphous calcium phosphate film that is present as early as 10 mins. on the 45S5 surface. This vibrational mode decreases in frequency, starting at 600 cm^{-1} and decreases to 570 cm^{-1}, until crystallization of the apatite occurs at 120 mins. Thus the onset of Stage 5 of the 45S5 composition is 120 mins. With crystallization, the P-O bending vibration divides into two modes with one at 600 cm^{-1} and the second at 565 cm^{-1} (11). Both modes remain unchanged thereafter.

Figure 2 shows that just prior to the onset of crystallization of the apatite phase is the appearance of a C-O stretching vibration in the amorphous calcium phosphate layer. This mode initially appears at a wavenumber of approximately 930 cm^{-1} after one hour. It decreases in frequency to 870 cm^{-1} as the crystallization of the hydroxyl-carbonate apatite phase occurs and is subsequently not visible after the growth of the phase reaches a critical thickness.

These results for 45S5 are very similar to those previously reported by Kim, et al. (6) and Andersson, et al. (2). The primary difference is the earlier onset of Stages 3 and 4 observed in this study. The amorphous calcium phosphate phase occurs as early as 10 mins. in this study, which is approximately twice as fast as previously reported (Table 2). This difference is attributed to the greater resolution of the SXB FTIR used in the present study.

Composition #1 (S63.5P6)

No changes in the spectrum of this glass are visible even after 5 days exposure to tris buffer at 37°C. Thus the increase in SiO_2 content from 53 wt% to 63 wt% is sufficient to slow down the surface alkali exchange, network dissolution and hydrolysis to an extent that prohibits formation of either the silica-rich film or precipitation of a calcium phosphorous-rich film on the surface of the glass.

Composition #9 (S53P4)

The spectrum of this composition before reaction and after 360 and 4320 mins. reaction is shown in Fig. 1C. The appearance of new double peaks at 610 and 565 cm^{-1} show that a crystalline hydroxyl-carbonate apatite layer has formed on this glass by 4320 mins. The time dependent changes of the surface reactions for glass #9 are plotted in Fig. 3. They can be compared with similar plots for glass 45S5, Fig. 2, and glass #10 reported previously (2), obtained under identical experimental conditions.

Figure 3 and Table 2 show that the reaction sequence observed for glass #9 is equivalent to the reaction sequence previously reported for glasses 45S5.4F, 45S5 and composition #10 (S45P7), ref. 2. Thus the presence of 8 wt% more SiO_2 in the glass did not alter the sequence of the five stages of surface reactions. However, it is clear that the rate of the third stage of reaction, the polycondensation of the SiO_2-rich layer, has been substantially decreased for glass #9. The time required for formation of the Si-O-Si stretching vibration due to polycondensation of neighboring silanol groups was lengthened to 90 mins. Likewise, the formation of the amorphous calcium phosphorous layer is decreased to 360 mins. The incorporation of carbonate species within the amorphous layer occurs as seen previously on the other bioactive glasses and eventually crystallization of the hydroxyl-carbonate apatite phase on the surface occurs. However, this crystalline phase is delayed until 4,320 mins. This is a decrease of nearly 40X over the onset of crystallization of the HCA layer on 45S5.4F and 45S5 bioactive glasses. It is a decrease of nearly 12X over that of composition #10 (Table 2).

DISCUSSION

Previous work by Andersson, et al. (7) showed that glass #1 developed only a thin silica-rich layer and no calcium phosphate layer. This composition also did not result in interfacial bonding. In contrast both glasses #9 and #10 did form substantial interfacial push-out strengths within 7-8 weeks. In various models 45S5.4F and 45S5 implants have also developed substantial interfacial strengths due to bonding in bone (3,10). Also, Wilson and Nolletti (12) have shown that bioactive glasses 45S5, 45S5.4F and compositions similar to #10 bond to soft tissues. The compositional bonding boundary for soft tissue adherence is close to composition for glass #9 reported herein.

These studies of the surface reaction kinetics lead to the following findings:

1) Compositions in excess of 60% SiO_2 (glass #1) have sufficiently slow reactions that a calcium phosphate-rich film does not form and no in-vivo bonding takes place. This finding confirms previous studies (3-5,13).

2) Increasing the SiO_2 content from 45% (by weight) to 53% SiO_2 substantially reduces the rate of formation of surface silanols and slows down the subsequent polycondensation reaction required to form a silica-rich layer. Consequently, the time to form the amorphous calcium phosphate layer is increased. The rate of crystallization of the hydroxyl-carbonate apatite (HCA) layer is greatly slowed down. This drastic reduction in the rate of formation of the HCA layer is in spite of having sufficient CaO and P_2O_5 content in the glass available for formation of the calcium phosphate-rich film. Consequently, these results indicate that the kinetics of formation of the polycondensation reaction of silica (Stage 3) are critical in controlling the rate of formation of the calcium phosphate film, and its nucleation and crystallization to HCA. This finding is consistent with previous studies on P_2O_5 free Na_2O-SiO_2 glasses (13). Kokubo (14) has shown that glasses that contain only CaO and SiO_2 form an apatite film on the surface by incorporating phosphate ions from a simulated body fluid. The presence of pre-existing apatite crystals within the glass-ceramic does not affect this process.

3) These results indicate that the critical reaction rate constant in bioactive glasses and glass-ceramics is Stage 3 which controls the polycondensation of silanol groups that form Si-O-Si bonds on the surface. This is an exothermic reaction and occurs due to the presence of a metastable pentacordinated silica molecule on the surface as an intermediate step in the reaction (15). It is possible that this metastable state and the loss of H_2O from the condensation reaction is associated with the nucleation of the calcium phosphate complexes on the glass surface. These complexes incorporate CO_2 molecules from the solution and result in the nucleation of a hydroxyl-carbonate crystal. Any changes in composition which slow down or eliminate the presence of the Stage 3 silica polycondensation reaction appear to greatly decrease the rate of formation of the hydroxyl-carbonate apatite layer. It is this layer that forms the bonding with biological moieties and eventually gives rise to tissue bonding and bioactivity. Thus, the rate of tissue bonding appears to be controlled by the rate of the Stage 3 reaction.

ACKNOWLEDGEMENTS

REFERENCES

1.   Hench, L. L. The Kinetics of Bioactive Ceramics, Part I: Reaction Rates in Bioceramics 3, Hulbert, S., ed., 1991.

2.   Andersson, O. H., LaTorre, P., and Hench, L. L. The Kinetics of Bioactive Ceramics, Part II: Surface Reactions of Three Bioactive Glasses, Bioceramics 3, Hulbert, S., ed., 1991.

3.   Hench, L. L. and Clark, A. E. In Biocompatibility of Orthopedic Implants, Vol. 2, Williams, D. F., ed., CRC Press, Boca Raton, Florida, 1982, Chap. 6.

4.   Gross, U., Kinne, R., Schmitz, H. J., Strunz, V. In CRC Critical Reviews in Biocompatibility, Vol. 4, Issue 2, Williams, D. L., ed., CRC Press, Boca Raton, Florida, 1988, 155.

5.   Hench, L. L. In Bioceramics: Materials Characteristics Versus In Vivo Behavior, Vol. 523, Ducheyne, P. and Lemmons, J., eds., Annuals of the New York Academy of Sciences, 1988, 54-71.

6.   Kim, C. Y., Clark, A. E., and Hench, L. L. J. Non-Cryst. Solids, 1989, 113, 195-202.

7.   Andersson, Ö. H. The Bioactivity of Silicate Glass, Ph.D. Dissertation, Dept. of Chemical Engineering, Åbo Akademi University, Finland, 1990.

8.   Andersson, Ö. H., Liu, G., Karlsson, K. H., Niemi, L., Miettinen, J., and Juhanoja, J. J. Mater. Sci., Materials in Medicine, 1990.

9.   Andersson, Ö. H., to be published.

10.   Hench, L. L., Paschall, H. A., Allen, W. C. and Piotrowski, G. National Bureau of Standards Special Publication 415, May 1975, 19-35.

11.   Le Geros, R. F., Bone, G., and Le Geros, R. Calcif. Tissue Res., 1978, 26 111.

12.   Wilson, J. and Nolletti, D. In Handbook of Bioactive Ceramics, Vol. I., Yamamuro, T., Wilson, J., and Hench, L. L., eds., CRC Press, Boca Raton, Florida, 1990, Chap. 28.

13.   Ogino, M., Ohuchi, F. and Hench, L. L. J. Biomedical Maters. Res., 1980, 14, 55-64.

14.   Kokubo, T. In Handbook of Bioactive Ceramics, Vol. I, Yamamuro, T., Hench, L. L. and Wilson, J., eds., CRC Press, 1990, 41.

15.   Davis, L. P. and Burggraf, L. W. In Ultrastructure Processing of Advanced Ceramics, Mackenzie, J. D. and Ulrich, D. R., eds., J. Wiley, New York, 1988, 367.

SECTION VII

PROJECT E:
Electronic Characterization of
Semiconductor Interfaces

a. Visible Light Emission from P - N Porous Silicon Homojunction
Diodes

Zhiliang Chen and Gijs Bosman
Department of Electrical Engineering
University of Florida
Gainesville Fl 32611

and

Romulo Ochoa

Department of Materials Science and Engineering
University of Florida
Gainesville Fl 32611

Abstract

We observed visible light emission with a peak wavelength of 640 nm from $p^+ - n^+$ forward biased porous silicon homojunction diodes. The light emission is attributed to electron-hole recombination across the direct bandgap of the monocrystalline quantum wires which make up the porous silicon junction layers.

This paper reports the fabrication and characterization of a light emitting diode (LED) made of a $p^+ - n^+$ porous silicon (PS) homojunction. Our work is based on recent developments which indicate that the monocrystalline quantum wires, responsible for the porous structure [1], have direct bandgaps ranging from 3.5 to 1.5 eV for wire diameters between 10 and 35 Angstrom [2]. These quantum wires form during electrochemical etching of silicon wafers in diluted HF [1].

Realizing that a wide spectrum of applications in the area of silicon based photonics may result from these developments, many researchers, including ourselves, repeated Canham's photoluminescence (PL) experiment, with some modifications [3,4,5] and for other materials such as Ge [6] and SiGe [7], and basically found similar PL results. Encouraged by these results, projects to fabricate PS based devices that exhibit electroluminescence (EL) were initiated .

Richter et al. [8] published current-induced light emission data measured on n-type PS samples covered by a 12 nm gold layer. A spectrum with a peak at 680 nm was measured when a current of 5 mA passed through the sample. The voltage across the sample was 200 V.

A Schottky-barrier type structure using p-type PS was fabricated and analyzed by Koshida et al. [9]. Their EL device exhibited rectifying junction behavior, although their non-ideality factor was quite large. When the forward current density exceeded 90 mA/cm^2 at 7 V, a stable and uniform light emission resulted with a peak wavelength of 680 nm.

Namavar et al. [10] observed visible EL from a p-type PS / n-type ITO heterojunction diode having rectifying properties and a non-ideality factor of 10. The measured light intensity appeared to depend linearly on the injected current. In both the Schottky [9]- and the heterojunction [10]- diode the light emission is explained in terms of electron-hole recombination across the direct bandgap of the p-type PS layer making up one side of the junction.

The focus of this paper is on the fabrication and characterization of a PS homojunction formed between a heavily doped n-type and p-type PS layer.

P-type, <100> silicon wafers with a resistivity of 6 - 18 Ω cm were implanted through the back side with Boron to provide a p^+ ohmic contact layer. To form a $n^+ - p^+$ junction, Phosphorous and Boron were implanted through the top surface and subsequently annealed. The resulting doping profile measured with spreading resistance probes is shown in figure 1. A n^+- layer with a doping density between $(1-2) \times 10^{19}$ /cm^3 extends from the surface to a depth of 2.5 μm, followed by a p^+ - layer with a peak doping density of 1×10^{19}/cm^3 . The background, p - type substrate doping is 8×10^{14}/cm^3 . Samples of 0.5×0.5 cm^2 were cut from the wafer and mounted on the anode of a teflon chemical cell filled with 20 % HF by volume after covering the ohmic, sputtered Aluminum back contact with wax. The $n^+ - p^+ - p$ layer ordering ensures that the junction electric field does not impede the flow of charge required for the electrochemical process to take place. The electrochemical etching was carried out in the dark.

A Hewlett Packard semiconductor parameter analyzer was programmed to provide a constant current density of 20 mA/cm^2 for a specific amount of time and was also used to monitor the voltage V across the chemical cell during etching. Figure 2 shows V as a function of time t for a period of almost 600 seconds. Notice that for t between 0 and 100 s. V is rather constant, then a sharp drop occurs, followed by a gradual increase to again a constant level of about 0.75 V. We believe that the HF-liquid / silicon surface junction, which results from the surface Fermi level pinning at adsorbed F$^-$ sites is responsible for this V(t) behavior [11]. For 0 < t < 100 s., pores form in the heavily doped n-region. The liquid-surface barrier is high due to Fermi level pinning at F$^-$ sites at about 0.4 eV above the valence band [11], making it difficult for the surface bond electrons to escape. This severely limits the flow of charge resulting in a high voltage drop across the cell when driven by a constant current source. At t = 100 s. the pores start to penetrate the n - p junction region. The

surface barrier becomes lower than in the n^+ - case, as a simple
picture of Fermi level pinning will illustrate, and surface bond
electrons can more easily escape. Consequently, the liquid-silicon
interface impedes charge flow less and a low voltage across the
cell develops under constant current conditions. For 200 < t < 250
s., a constant V(t) is observed which we associate with pore
penetration of the p^+ - region. At t = 250 s. a gradual increase
sets in which indicates that the pores have reached the region
where the acceptor doping level decreases (see Fig. 1) and thus
the surface barrier widens, reducing the probability for surface
electron escape. This pore progression model is confirmed by
spreading resistance probe measurements on our electrochemically
etched, porous samples. Spreading resistance data on n- and p-
type porous sample sections show higher resistivity values with a
larger data variance than result from bulk layers and are
therefore a useful tool to determine the spatial extent of pore
formation. Based on this insight we electrochemically etched the
samples for six minutes since that results in n^+ - p^+ PS
homojunctions with the pores extending to p^+ - p interface as
illustrated by the inset of figure 2.

After etching, the samples were exposed to 49 % HF for 30
minutes under equilibrium conditions and cleaned using DI water. A
100 Angstrom gold layer was deposited on the PS surface and used
as top electrical contact. A standard mesa etch procedure was used
to define a matrix of 5 x 5 mesas with a cross-sectional area of
about 1 mm^2 each.

Orange/reddish light emanated from the side surface of
individual mesas at a forward bias turn-on voltage V_L of 5 - 10 V
and was discernable with the eye in the dark. We observed a direct
correlation between the quality of a mesa and its value of V_L.
Mesas with good I - V characteristics had lower V_L values. No
visible light emission was observed under reverse bias conditions.
The I - V characteristics of the mesa devices were found to be
stable for at least six hours in stress tests during which visible
light emission persisted.

To increase the light output two adjacent rows of five mesas each were contacted using silver paste and biased in parallel.

Figure 3 shows the current voltage characteristic of a sample array consisting of ten mesas in parallel. Note that the sample has excellent rectifying properties, has a non-ideality factor of 3 measured over three decades of current (inset) , and a series resistance of 250 Ω .

Normalized PL and EL spectra are shown in figure 4. The measured data was smoothened to reveal the peak position and the spectral shape more precisely. The spectral measurements were carried out using a double monochromator with photon counting electronics. The PL spectrum was measured on a single $p^+ - n^+$ mesa using a 514.5 nm Argon laser, whereas the EL spectrum was produced by the array described above biased with a current source at 60 mA. The peak wavelengths of the PL and EL spectra are the same at 640 nm which corresponds to a wire size of 22 Angstrom [2]. The EL spectrum is slightly broader that the PL spectrum. This may result from the array area being 10 times larger than a single mesa area so that a wider quantum wire size distribution may be expected in the former.

In summary, we observed visible light emission from $p^+ - n^+$ porous silicon homojunction diodes biased at low forward bias voltages of 5 - 10 V. Spectral measurements on an array of 10 devices biased at 60 mA indicated a peak wavelength of 640 nm. We attribute the light emission to electron-hole recombination across the direct bandgap of the quantum wires that make up the porous silicon junction layers. Band calculations indicate that the peak wavelength of 640 nm corresponds to a quantum wire size of 22 Angstrom. TEM measurements are underway to further investigate the relationship between the peak wavelength of EL and PL spectra and the quantum wire size.Finally, the above outlined low cost fabrication procedure results in reproducible and stable devices and has a high yield.

References

1. L. T. Canham, Appl. Phys. Lett. **57**, 1046 (1990).

2. G. D. Sanders and Y.- C. Chang, Phys. Rev. B. **45**, 9202 (1992).

3. A. Halimaoui, C. Oules, G. Bomchil, A. Bsiesy, F. Gaspard, R. Herino, M. Ligeon, and F. Muller, Appl. Phys. Lett. **59**, 304 (1991).

4. J. C. Barbour, D. Dimos, T. R. Guilinger, M. J. Kelley, and S. S. Tsao, Appl. Phys. Lett. **59**, 2088 (1991).

5. K. H. Jung, S. Shih, T. Y. Hsieh, D. L. Kwong, T. L. Lin, Appl. Phys. Lett. **59**, 3264 (1991).

6. R. Venkatasubramanian, D. P. Malta, M. L. Timmons, and J. P. Hutchby, Appl. Phys. Lett. **59**, 1603 (1991).

7. S. Gardelis, J. S. Rimmer, P. Dawson, B. Hamilton, R. A. Kubiak, T. E. Whall and E. H. C. Parker, Appl. Phys. Lett. **59**, 2118 (1991).

8. A. Richter, P. Steiner, F. Kozlowski, and W. Lang, Electron Device Lett. **12**, 691 (1991).

9. N. Koshida and H. Koyama, Appl. Phys. Lett. **60**, 347 (1992).

10. F. Namavar, H. P. Maruska, and N. M. Kalkhoran, Appl. Phys. Lett. **60**, 2514 (1992).

11. J. D. L'Ecuyer and J. P. G. Farr, Proceedings of 4th Intl. Symp. on Silicon-on-Insulator Tech. and Devices, Montreal (1990).

Figure Captions.

Figure 1. Doping profile of Silicon N - P junction measured with spreading resistance probes.

Figure 2. The voltage V across the chemical cell measured as a function of time during electrochemical etching of a silicon wafer in the dark. The cell was biased with a current source. The inset schematically shows the layered structure of a single mesa.
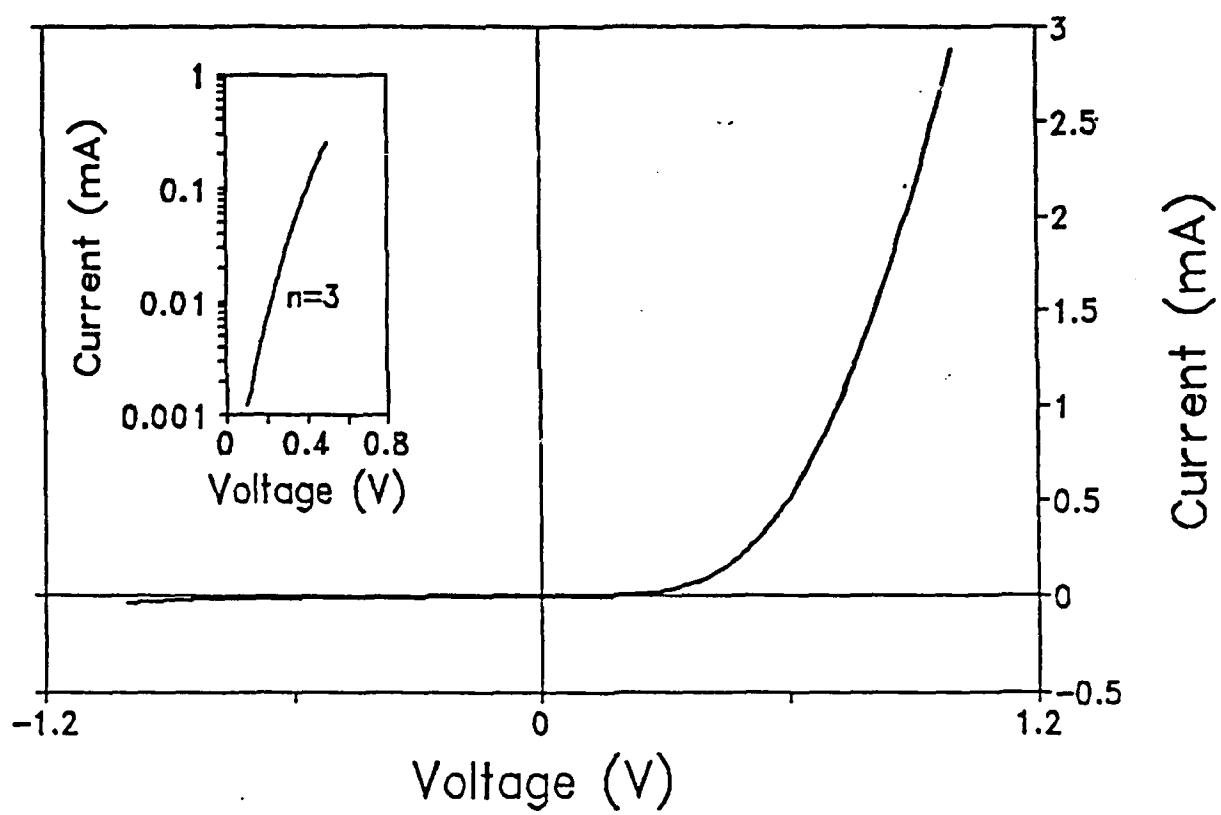
Figure 3. The current - voltage characteristic of a p^+ - n^+ porous silicon homojunction diode array. The inset shows a semi-logarithmic plot of forward current and voltage revealing a non-ideality factor of 3.
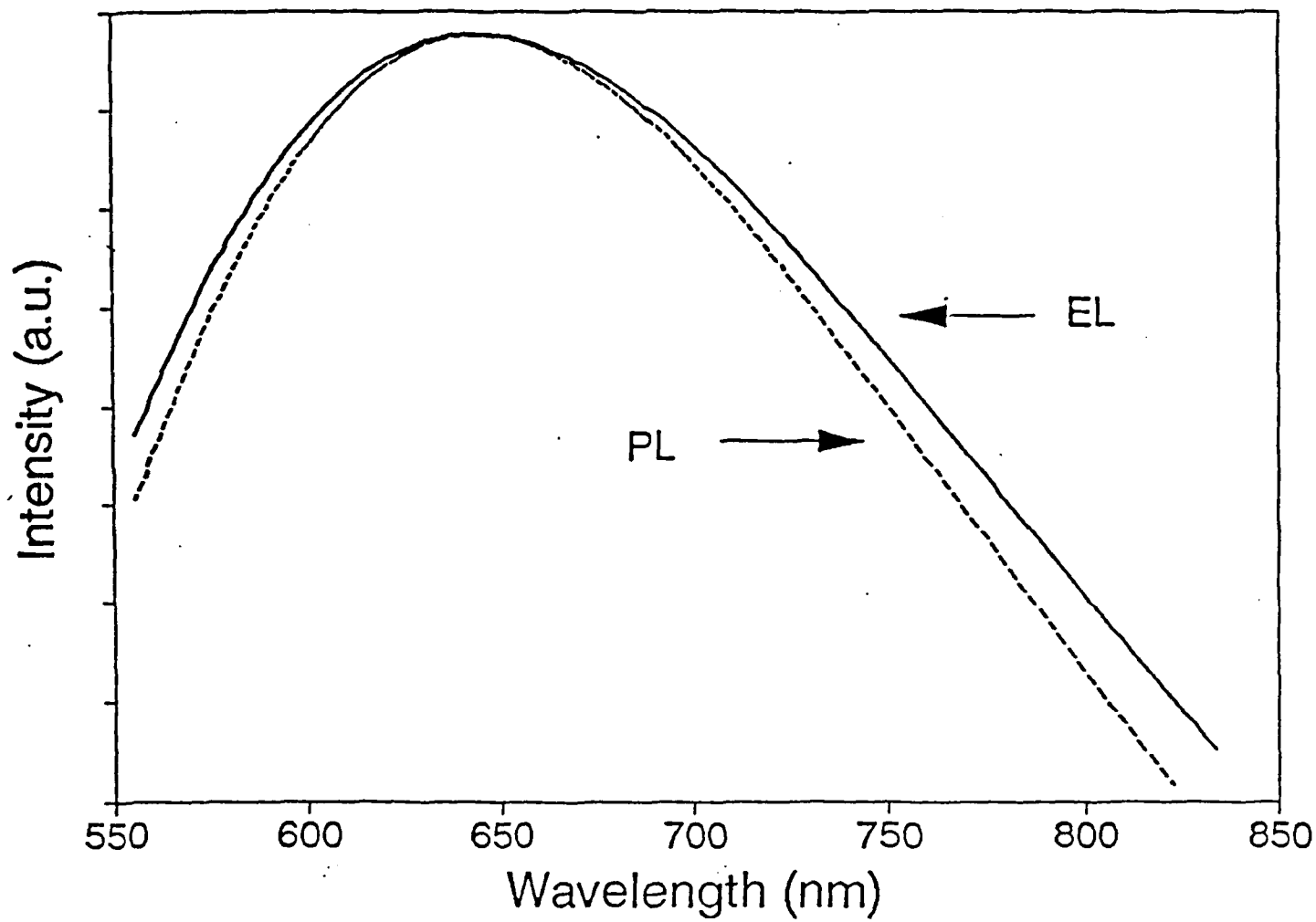
Figure 4. Normalized EL and PL spectra of a diode array and single diode, respectively.
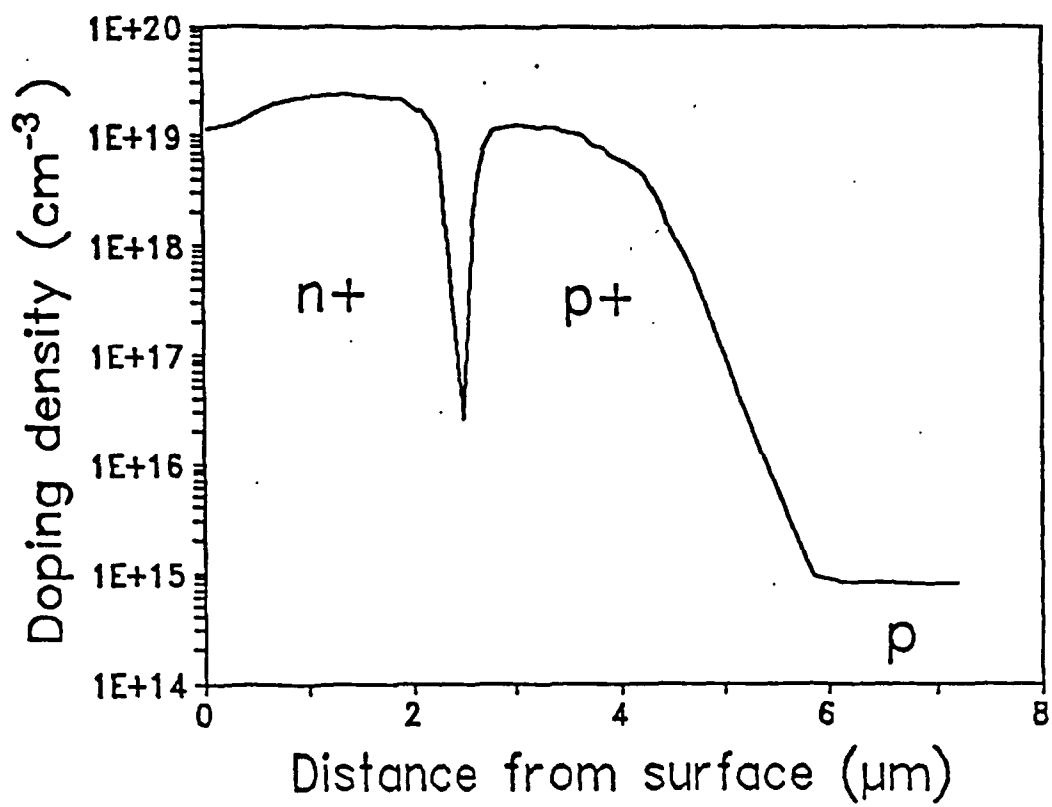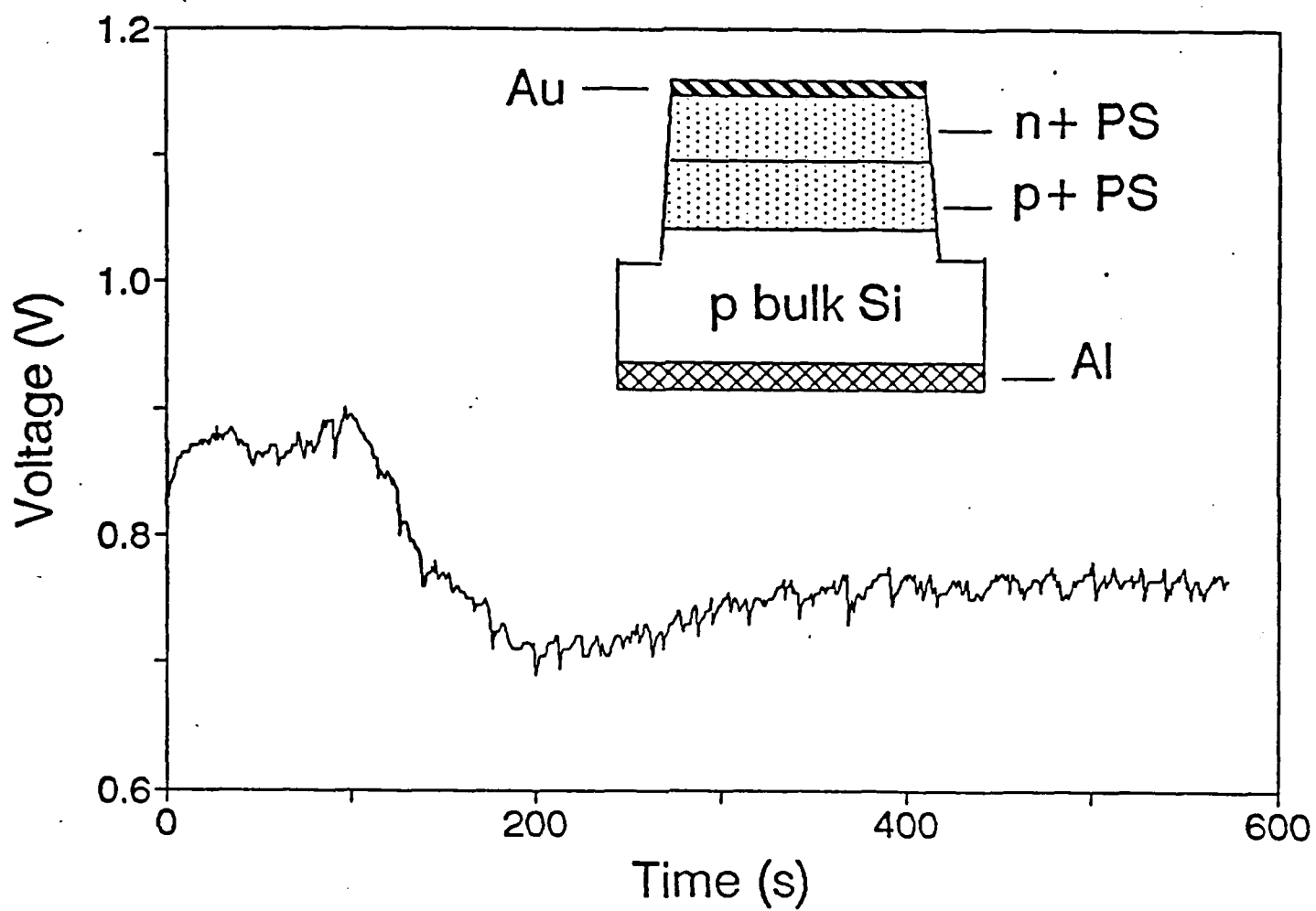
SECTION VIII

PROJECT F:
General Materials Science

a. Evidence for Protonic Conduction in Alkali-Free Phosphate Glasses

Makoto Kotama, Koji Nakanishi, Hideo Hosono, and Yoshihiro Abe

*Department of Materials Science and Engineering, Nagoya Institute of Technology, Gokiso-cho,
Showa-ku, Nagoya 466, Japan*

L. L. Hench

Advanced Materials Research Center, University of Florida, Alachua, Florida 32615

ABSTRACT

Species of electrical charge carriers in oxide glasses containing neither alkali ions nor transition metal ions is the subject of considerable uncertainty. Two different approaches adopted here made it clear that protons in $45BaO-55P_2O_5$ glasses are the charge carriers. One approach adopted is of a change in color by formation of H_xWO_3, which was caused by injection of the protons of the glass into WO_3 thin film under an electrical field, and the other is of a change in electrical conductivity by H^+-D^+ substitution in the glasses.

In most oxide glasses, electrical charge carriers are alkali ions such as Na^+ and Li^+ in alkali-containing glasses, or electrons in transition metal-containing glasses. Namikawa et al. (1) suggested that protons may be the charge carriers in alkali-free $BaO-P_2O_5$ glasses. Abe et al. (2) found that electrical conductivity is proportional to the square of proton concentration in alkaline-earth phosphate glasses and suggested that the protons in these glasses are the charge carrying species.

Generally, a small amount of "water" remains as -OH groups in glasses. It is expected that the protons of the -OH groups in alkaline earth phosphate glasses are responsible for the electrical conduction since the strength of the O-H bonding in these glasses is much lower owing to the formation of the strong hydrogen bonds of $-OH \cdots O^-$. Hosono et al. (3) showed that D^+ ions doped in $45MgO-55P_2O_5$ glasses are as mobile as H^+ ions in the glasses under an electrical field. Abe et al. (4) suggested that the species in $PbO-SiO_2$ glasses are also impurity protons in the glasses.

On the other hand, many researchers still have a prejudice that protons in oxide glasses are not so mobile to be the electrical charge carriers in any glasses. In fact, electrical charge carriers in fused SiO_2 glass are not protons but impurity Na^+ ions (5). Ernsberger (6-8) asserts that proton migration is only observed in highly hydrated glasses and crystals; the mechanism involves the handing-on of the proton from one H_2O to another by temporary formation of H_3O^+. Molecular water is necessary so that H^+ from H_3O^+ can be passed on to a different molecule from that from which it came. It is evident from IR spectroscopy that in the $BaO-P_2O_5$ glasses used here, no molecular water exists, but hydroxyl groups do exist (P-OH). We believe that whether protons in a glass become the charge carriers or not depends on the O-H bonding strength. It is a reasonable assumption that the protons (H^+) in the glasses are mobile if the O-H bonding is weak, that is, the hydrogen bond of $OH \cdots O^-$ is strong. The purpose of the present study is to give some proof that the protons in the $45BaO-55P_2O_5$ glasses are the electrical charge carriers.

Experimental Procedure

Preparation of glasses.—Guaranteed-grade reagents of barium carbonate and orthophosphoric acid (85%) were used as starting materials. Glasses were prepared by a conventional melt-quenching technique. Concentration of the remaining water (OH) was controlled by changing the melting temperature and time. Details of the preparation process are described in Ref. (9). Proton-free glasses containing various amounts of deuterons were prepared according to the process involving hydration of a "dry" glass in an autoclave (3).

Preparation of WO_3 film and construction of electrochromic (EC) cell.—Amorphous WO_3 films (3000 Å thick) were deposited onto one side surface of optically polished $BaO-P_2O_5$ glass plates (ca. 5 mm square by 1 mm thick) by vacuum evaporation. The as-deposited WO_3 films obtained by the evaporation were slightly deficient in oxygen so that the specimens were heated to 290°C and held for 2 h in dry oxygen atmosphere before they were submitted to the present electrochromic cell experiment. The heat-treatment made a change in the color of the films from light blue to light brown. The color is dependent on the stoichiometry of the film composition. Figure 1 shows a schematic diagram of the EC cell in which $BaO-P_2O_5$ glass is used as an electrolyte. Platinum was used for the electrodes and the electric leadwires. Gold foil was sandwiched between the electrode and the specimen in order to improve the physical contact. An external dc voltage of 250 V ($\approx 3.0 \times 10^3$ V/cm) was applied between the electrodes at 200°C in air and dry nitrogen atmosphere, respectively. The same experiment was carried out for the WO_3-deposited SiO_2 glass.

Electrical conductivity measurement.—Disk-like specimens (ca. 3 cm diam by 0.3 cm thick) were cut from the mother glass blocks and polished with 3 μm alumina abrasive. Gold films sputtered on the specimen were used as
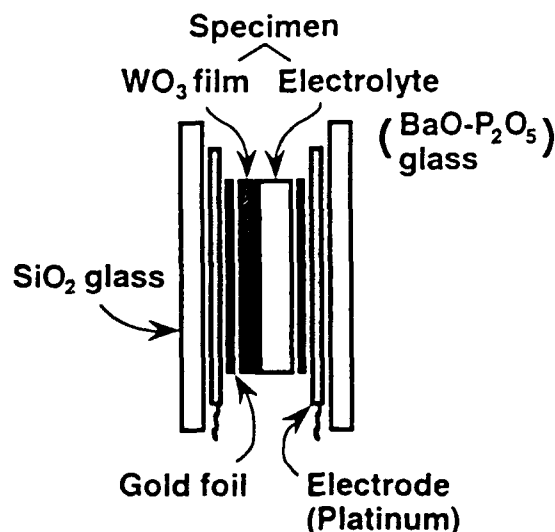

Fig. 1. Schematic diagram of an EC cell used in the experiment. The electrolyte is $45BaO-55P_2O_5$ glass.

2928

J. Electrochem. Soc., Vol. 138, No. 10, October 1991 · The Electrochemical Society, Inc.

105

electrodes in a three-electrode configuration. Direct-current (dc) conductivity was measured with a vibrating-reed electrometer over the temperature range from 100 to 200°C. Above 200°C, conductivity was measured by alternative-current (ac) method with a LCR meter in the frequency range from 100 Hz to 100 kHz. The dc conductivity was evaluated from the Cole-Cole plots assuming a RC parallel circuit for the specimens.

Determination of proton content.—Proton content was determined on the basis of Lambert-Beer's law by measuring the intensity of the IR absorption band due to the OH (≈ 2800 cm^{-1}) or OD (≈ 2100 cm^{-1}) stretching vibration (10). The $45BaO$-$55P_2O_5$ glasses containing D^+ instead of H^+ were prepared according to the previous paper (3). In the case of the proton-free but deuteron-containing specimens, it is impossible to evaluate the OD content directly from the "raw" spectrum because the absorption bands originated from the glass network of P-O-P bonds superimposed on the OD stretching band around 2100 cm^{-1}. The OD band appeared clearly by removing the network-related absorptions, *i.e.*, the spectrum of the "dry" glass was subtracted from a given raw spectrum. The molar extinction coefficient (ϵ_{OH}) of the OH band used was 150 L · mol^{-1} · cm^{-1}, which was evaluated from the plots (11) showing the relation between ϵ_{OH} and the OH band position. The quantitative relation between ϵ_{OH} and ϵ_{OD} is given by

$$\epsilon_{OD} = 0.60\, \epsilon_{OH} \qquad [1]$$

The procedure for obtaining the equation is described in Ref. (3).

Results and Discussions

Coloration of WO₃ film.—The coloration mechanism of WO₃ is

$$a\text{-}WO_3(\text{light brown}) + xM^+ + xe^- \rightarrow M_xWO_3(\text{blue}) \qquad [2]$$
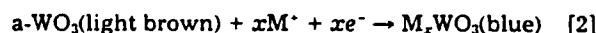
Tungsten bronze (M_xWO_3) is formed to be colored when cations (*i.e.*, H^+, Na^+, Ag^+) enter into the WO₃ film from an electrolyte and electrons from an electrode. The color center arises from the added electrons which are trapped by W^{6+} ions.

Figure 2 shows the optical transmission spectra of the specimen with WO₃ film; curve a and curve b are before and after the voltage is applied, respectively, and curve c is the difference spectrum between the curve a and b. On applying an external dc 250 V to the cell for several hours in dry nitrogen atmosphere, the specimen (WO₃ film) became blue and the optical transmission was reduced to be $\approx 50\%$ at 900 nm. The broad absorption band around 900 nm was obtained from the difference spectrum. It is known that the color band around 900 nm is characteristic of a series of bronzes. It is evident that the protons in the BaO-P_2O_5 glass were injected into the WO₃ film and as a result, the hydrogen tungsten bronze (H_xWO_3) was formed. After the reverse voltage was applied to the colored specimen for the same duration time in the dry nitrogen atmosphere, the transmission was recovered almost perfectly to the initial state. In the case of the WO₃-deposited SiO_2 glass specimen, no reduction of the transmission was observed.

In the case of the experiment in air, the specimen was colored more deeply than in the dry nitrogen atmosphere when the external voltage was applied. Although the bleaching was observed when the reverse same voltage was applied, the transmission was insufficiently recovered to the initial state. This was caused by the protons which are supplied under the electrical field from the air atmosphere to the WO₃ film. The SiO₂ glass specimen with WO₃ film showed no coloration in air as well as in the dry nitrogen atmosphere. It is clear that the BaO-P_2O_5 glass plays the role of proton conductor.

Change in electrical conductivity by substitution of D^+ for H^+ of the glasses.—Figure 3 shows the IR spectra of the specimens ($45BaO$-$55P_2O_5$ glass plates) containing protons or deuterons. The broad band around 2800 cm^{-1} is due to the O-H stretching mode. It is located at lower wave number in comparison with $45MgO$-$55P_2O_5$ glasses (3100 cm^{-1}).

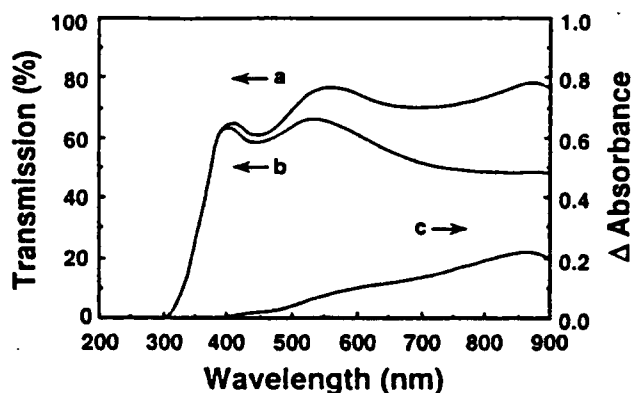Fig. 2. Optical transmission spectra of a WO₃-deposited 45BaO-55P₂O₅ glass and an absorption spectrum of the WO₃ film. Curve a and b are spectra of specimen before and after the dc voltage was applied, respectively. Curve c is the difference spectrum between a and b, which is characteristic of tungsten bronzes.

This indicates that the protons in the BaO-P_2O_5 glasses form stronger hydrogen bonds with acceptor oxygens than those in the MgO-P_2O_5 glasses. As a result, when compared at the same proton content, the activation energy of $45BaO$-$55P_2O_5$ glasses for the proton conduction is lower than that of $45MgO$-$55P_2O_5$ glasses; the conductivity of the former glasses is $\approx 10^{3.5}$ times as large as that of the latter ones. Upon substitution of D^+ for H^+, the band position moved from 2760 to 2130 cm^{-1}. Then the ratio of the wave number of the OH band to that of the OD band is 1.30, which is close to the value (1.44) estimated by a harmonic oscillator approximation.

Direct-current conductivity (σ) varied exponentially with temperature for all the specimens over the temperature range measured

$$\sigma = \sigma_0 \exp(-E/RT) \qquad [3]$$

where σ_0 and E are the pre-exponential factor and the activation energy for the conduction, respectively. Figure 4 shows the relation between the conductivity (σ_{417}) at 144°C ($1000/T = 2.4$) and the concentration of the protons or deu-
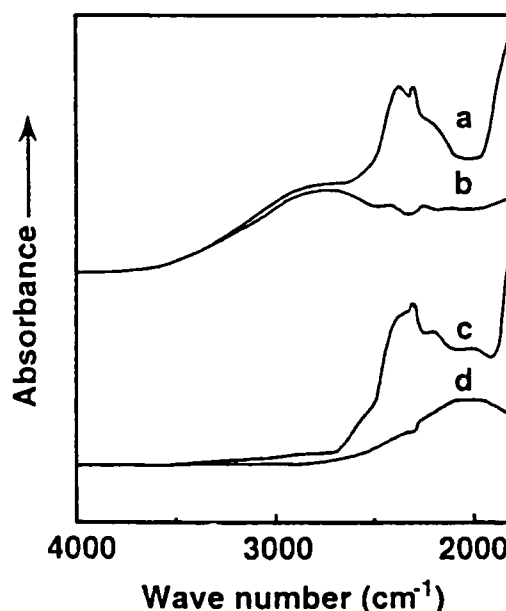

Fig. 3. IR spectra of 45BaO-55P₂O₅ glasses containing residual water. Curves a and c are typical spectra of specimens containing light and heavy water, respectively. Curves b and d are the "isolated" spectra of the light water and heavy water, respectively. These were obtained by subtracting absorptions due to the network of the host glass from the "raw" spectra a and c.
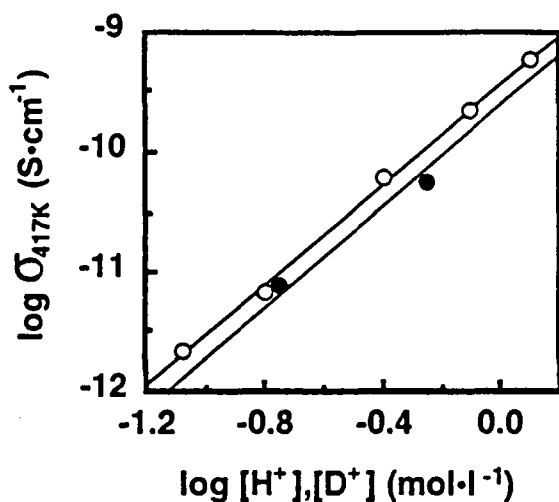
Fig. 4. Relation between electrical conductivity (σ_{417}) at 417 K and proton (○) or deuteron (●) concentration in 45BaO-55P$_2$O$_5$ glasses.

terons in the specimen. This relation is expressed by Eq. [4], which has been previously reported (2)

$$\sigma_{417} = A_0 [H^+]^2 \qquad [4]$$

where A_0 is a constant depending on the host glass and is a measure of proton mobility. The value of A_0 depends on ν_{OH} as given by Eq. [5] (2)

$$\log A_0 = -0.00970\, \nu_{OH} + 17.1 \qquad [5]$$

where ν_{OH} is the peak wave number of the stretching O-H infrared absorption band. The reason why the conductivity increases in proportion to the square of the proton [H$^+$] or deuteron [D$^+$] concentration has not been clear yet. The conductivity in the deuterated analog is somewhat lower than that in the protonated specimen when compared at the same concentration. These results also agree well with an assumption that the proton in some glasses are the main electrical charge carriers.

In addition, the assumption receives a support from the following results.

1. Electrical conductivity increases with proton concentration in alkali-free alkaline-earth phosphate glasses (2).

2. Electrical conductivity decreases with the strength of the O-H bonding, i.e., it increases with the strength of the hydrogen bonding (2).

3. Examination of the Seebeck effect shows that the sign of charge carriers in CaO · P$_2$O$_5$ glass is positive ($\approx$2 mV/deg) (12).

Concluding Remarks

Many researchers still have a prejudice that protons in oxide glasses are not mobile under an electrical field. This is true in some oxide glasses such as SiO$_2$ glass and silicate glasses containing a large amount of alkali ions. However, the mobility of protons in glasses depends on the O-H bonding strength; it is possible that protons are the electrical charge carriers in some glasses in which O-H bonding is weak, i.e., hydrogen bonding is very strong.

Evidence for protonic conduction in alkali-free BaO-P$_2$O$_5$ glasses were given in the present work. In alkaline-earth phosphate glasses, the O-H bonding is weak owing to the formation of strong hydrogen bonding. Alkaline-earth phosphate glasses have a potential use for the high proton conductive electrolyte when the OH concentration is increased.

REFERENCES

1. H. Namikawa and Y. Asahara, *Yogyo Kyokai-shi*, **74**, 205 (1966).
2. Y. Abe, H. Hosono, Y. Ohta, and L. L. Hench, *Phys. Rev. B*, **38**, 1016 (1988).
3. H. Hosono, T. Kamae, and Y. Abe, *J. Am. Ceram. Soc.*, **72**, 294 (1989).
4. Y. Abe, H. Hosono, Y. Hikichi, and L. L. Hench, *J. Mater. Sci. Lett.*, **9**, 1443 (1990).
5. R. H. Doremus, *This Journal*, **115**, 181 (1968).
6. F. M. Ernsberger, *Phys. Chem. Glasses*, **21**, 146 (1980).
7. F. M. Ernsberger, *J. Non-Cryst. Solids*, **38 & 39**, 557 (1980).
8. F. M. Ernsberger, *J. Am. Ceram. Soc.*, **66**, 747 (1983).
9. Y. Abe, H. Shimakawa, and L. L. Hench, *J. Non-Cryst. Solids*, **51**, 357 (1982).
10. Y. Abe and D. E. Clark, *J. Mater. Sci. Lett.*, **9**, 244 (1990).
11. H. Scholze, *Glastech. Ber.*, **32**, 81 (1959).
12. Y. Abe et al., Unpublished data.

SECTION IX

LIST OF MIRP PUBLICATIONS
1988-1992

"Gel-Silica Optics," L. L. Hench, S. H. Wang, and J. L. Nogues, in Multifunctional Materials, Vol. 878, Robert L. Gunshor, ed., SPIE, Bellingham, WA, 1988, pp. 76-85.

"New Perspectives of Silicon Carbide: An Overview, With Special Emphasis on Noise and Space-Charge-Limited Flow," Carolyn M. Van Vliet, Gijs Bosman, and Larry L. Hench, Ann. Rev. Mater. Sci. 18 (1988) 381-421.

"Ceramics and the Challenge of Change," L. L. Hench, Advanced Ceramic Materials 3[3] (1988) 203-206.

"Theory and Experiments of 1/f Noise in Schottky-Barrier Diodes Operating in the Thermionic-Emission Mode," Min-Yih Luo, Gijs Bosman, Aldert van der Ziel, and Larry L. Hench, IEEE Transactions of Electron Devices 35[8] (1988) 1351-1356.

"Structural Evolution at Low Temperature of Formamide Modified Silica Xerogels," Gerard Orcel, Jean Phalippou and Larry Hench, J. Non-Crystalline Solids 104 (1988) 170-180.

"Optical Properties of Gel-Silica Glasses," Shi-Ho Wang, Candace Campbell and L. L. Hench, in Ultrastructure Processing of Advanced Ceramics, John D. Mackenzie and Donald R. Ulrich, eds., John Wiley and Sons, New York, NY, 1988, pp. 145-157.

"Dielectric Relaxation Analysis of Gel Drying, S. Wallace and L. L. Hench, in Ultrastructure Processing of Advanced Ceramics, John D. Mackenzie and Donald R. Ulrich, eds., John Wiley and Sons, New York, NY, 1988, pp. 873-890.

"Effect of Formamide Additive on the Chemistry of Silica Sol-Gels, Part II: Gel Structure," G. Orcel, L. L. Hench, I. Artaki, J. Jonas and T. W. Zerda, J. Non-Crystalline Solids 105 (1988) 223-231.

"Preparation and Characterization of Monolithic Si-Ce-O Gels," A. Sivade, G. Orcel, L. L. Hench, J. Bouaziz, R. Sempere and D. Bourret, J. Non-Crystalline Solids 105 (1988) 332-342.

"Dielectric Relaxation Analysis of Water Adsorption in Sol-Gel Derived Silica Gel Monoliths," S. Wallace and L. L. Hench, in Better Ceramics Through Chemistry III, C. Jeffrey Brinker, David E. Clark and Donald R. Ulrich, eds., Vol. 121, Materials Research Society, Pittsburgh, PA, 1988, pp. 355-360.

"Physical Properties of Dried Na_2O-SiO_2 Monoliths," Rounan Li and L. L. Hench, in Better Ceramics Through Chemistry III, C. Jeffrey Brinker, David E. Clark and Donald R. Ulrich, eds., Vol. 121, Materials Research Society, Pittsburgh, PA, 1988, pp. 589-592.

"Physical and Structural Evolution of Sol-Gel Derived TiO_2-SiO_2 Glasses," Yeu-Chyi Cheng and Larry L. Hench, in Better Ceramics Through Chemistry III, C. Jeffrey Brinker, David E. Clark and Donald R. Ulrich, eds., Vol. 121, Materials Research Society, Pittsburgh, PA, 1988, pp. 593-596.

"Corrosion of Silicate Glasses: An Overview," L. L. Hench in Materials Stability and Environmental Degradation, Aaron Barkatt, Ellis D. Verink, Jr., and Leslie R. Smith, eds., Vol. 125, Materials Research Society, Pittsburgh, PA, 1988, pp. 189-200.

"Protonic conduction in Oxide Glasses: Simple Relations Between Electrical Conductivity, Activation Energy, and the O-H Bonding State," Yoshihiro Abe, Hideo Hosono, Yoshio Ohta, and L. L. Hench, Physical Review B 38[14] (1988) 10166-10169.

"Gel Silica Waveguides", R. V. Ramaswamy, T. Chia, R. Srivastava, A. Miliou, and J. West, 1988, SPIE, Vol. 878.

"Sol-Gel Composites," R. C. Dalton, M. B. Troffer, S-M Sim and D. E. Clark, to be published by VCH Publishers, Palo Alto, CA, Encyclopedia of Composites (1988).

"Electrophoretic Alumina Sol-Gel Coatings on Metallic Substrates," D. E. Clark, W. J. Dalzell, Jr. and D. C. Folz, in Ceramic Engineering and Science Proceedings, 9 [9-10], pp 1111-1119 (1988).

"Laser-Assisted Fabrication of Optical Waveguides in Sol-Gel Glasses", A. Miliou, R. Srivastava, V. Ramaswamy, T. Chia, and J. West, IGWO, Feb. 6-8, 1989, Houston, TX.

"Glasses From Sol-Gel Monoliths," L. L. Hench in Advances in Materials Science and Enginering, Concise Subject Encyclopedia, R. Brook, ed., Pergamon Press, New York, 1989.

"Bioceramics and the Origin of Life," L. L. Hench, J. Biomed. Maters. Res. 23 (1989) 685-703.

"Sol-Gel Processing of Large Silica Optics," L. L. Hench, M.J.R. Wilson, C. Balaban and J. L. Nogues, to be published in the Proceedings of the 4th International Conference on Ultrastructure Processing of Ceramics, Glasses and Composites, Tucson, AZ, Feb. 19-24, 1989.

"Structural Analysis of Water Adsorbed in the Pores of Alkoxide Derived Silica Gel Monoliths," S. Wallace and L. L. Hench, to be published in the Proceedings of the 4th International Conference on Ultrastructure Processing of Ceramics, Glasses and Composites, Tucson, AZ, Feb. 19-24, 1989.

"Quantum Calculations on Sol-Gel Silica Clusters," J. K. West, S. Wallace, L. L. Hench and C. R. Lishawa, to be published in the Proceedings of the 4th International Conference on Ultrastructure Processing of Ceramics, Glasses and Composites, Tucson, AZ, Feb. 19-24, 1989.

"Dilatometry of Gel-Silica," Bing Fu Zhu and L. L. Hench, to be published in the Proceedings of the 4th International Conference on Ultrastructure Processing of Ceramics, Glasses and Composites, Tucson, AZ, Feb. 19-24, 1989.

"Real Time Monitoring of Silica Gel Drying Behavior," M.J.R. Wilson, and L. L. Hench, to be published in the Proceedings of the 4th International Conference on Ultrastructure Processing of Ceramics, Glasses and Composites, Tucson, AZ, Feb. 19-24, 1989.

"Sol-Gel Derived Titania-Silica Gel-Glasses," Yeu-Chyi Cheng and L. L. Hench, to be published in the Proceedings of the 4th International Conference on Ultrastructure Processing of Ceramics, Glasses and Composites, Tucson, AZ, Feb. 19-24, 1989.

"A Topological Model of the Sintering of Sol-Gel Silica," W. L. Vasconcelos, R. T. DeHoff and L. L. Hench, to be published in the Proceedings of the 4th International Conference on Ultrastructure Processing of Ceramics, Glasses and Composites, Tucson, AZ, Feb. 19-24, 1989.

"Science of Chemical Processing of Ceramics and Technology" L. L. Hench, in Advanced Ceramics, Waldimir Pirro E. Longo, Sergio Neves Monteiro, Jamil Duailibi Filho, eds., II ENOMET, Rio de Janeiro, Brazil, 1989, pp. 2-14.

"Physical Evolution of Gel-Silica Monoliths," W. L. Vasconcelos, R. T. DeHoff, and L. L. Hench, in Advanced Ceramics, Waldimir Pirro E. Longo, Sergio Neves Monteiro, Jamil Duailibi Filho, eds., II ENOMET, Rio de Janeiro, Brazil, 1989, pp. 16-23.

"Multifunctional Silica Optics," L. L. Hench and A. Fosmoe in Mat. Res. Soc. Symp. Proc. Vol. 175, Multifunctional Materials, A. Buckley, G. Gallagher-Daggitt, F. E. Karasz, D. R. Ulrich, eds., Materials Research Society, Pittsburgh, PA, 1990, pp. 23-34.

"Quantum Chemistry of Sol-Gel Silica Clusters," Jon K. West, Bing Fu Zhu, Yeu-Chyi Cheng, and L. L. Hench, J. Non-Crystalline Solids 121 (1990) 51-55.

"Structural Evolution During Sintering of Optical Sol-Gel Silica," W. L. Vasconcelos, R. T. DeHoff, and L. L. Hench, J. Non-Crystalline Solids 121 (1990) 124-127.

"Processing of Gel-Silica Monoliths for Optics," L. L. Hench and M.J.R. Wilson, J. Non-Crystalline Solids 121 (1990) 234-243.

"Mechanical Properties Evolution During Sintering of Optical Sol-Gel Silica," W. L. Vasconcelos and L. L. Hench, J. Non-Crystalline Solids 121 (1990) 132-135.

"A Positronium Decay Analysis of the Pore Ultrastructure of Sintered Gel-Silica Monoliths," T. W. Zerda, W. L. Vasconcelos, and L. L. Hench, J. Non-Crystalline Solids 121 (1990) 143-146.

"The Sol-Gel Process," L. L. Hench and J. K. West, Chem. Rev. 90 (1990) 33-72.

"Gel-Silica Science," L. L. Hench and W. Vasconcelos, Annu. Rev. Mater. Sci. 20 (1990) 269-298.

"The Sol-Gel Glass Transformation of Silica," L. L. Hench and S. H. Wang, Phase Transitions 24-26 (1990) 785-834.

"The Chemical Processing of Silicates for Biological Applications - A Review," L. L. Hench and June Wilson, in Better Ceramics Through Chemistry IV, Brain J.J. Zelinski, C. Jeffrey Brinker, David E. Clark and Donald R. Ulrich, eds., Vol. 180, Materials Research Society, Pittsburgh, PA, 1990, pp. 1061-1071.

"Transpiration Cooled Porous Type VI Silica Rocket Windows," Albert G. Fosmoe, II and Larry L. Hench, in Better Ceramics Through Chemistry IV, Brain J.J. Zelinski, C. Jeffrey Brinker, David E. Clark and Donald R. Ulrich, eds., Vol. 180, Materials Research Society, Pittsburgh, PA, 1990, pp. 843-848.

"Laser Densification Modeling," Taipau Chia, L. L. Hench, Chaobin Qin, and C. K. Hsieh, in Better Ceramics Through Chemistry IV, Brain J.J. Zelinski, C. Jeffrey Brinker, David E. Clark and Donald R. Ulrich, eds., Vol. 180, Materials Research Society, Pittsburgh, PA, 1990, pp. 819-824.

"Molecular Orbital Modeling of Water Adsorption on a Tetrasiloxane Ring," J. K. West and S. Wallace, S. in Better Ceramics Through Chemistry IV, Brian J.J. Zelinski, C. Jeffrey Brinker, David E. Clark, and Donald R. Ulrich, eds., Vol. 180, Materials Research Society, Pittsburgh, PA, 1990, p. 255-260.

"From Concept to Commerce: The Challenge of Technology Transfer," L. L. Hench, MRS Bulletin, August 1990, 49-53.

"Gel-Silica Hybrid Optics," L. L. Hench, J. K. West, B. F. Zhu and R. Ochoa, Proceedings of SPIE Meeting, San Diego, CA, July 11-13, 1990.

"Molecular Orbital Modeling of Water Adsorption on a Tetrasiloxane Ring," J. K. West and S. Wallace, Spring MRS Meeting, San Francisco, CA, April 16-21, 1990.

"Protonic Conduction in $PbO-SiO_2$ Glasses: A Quantitative Estimation," Y. Abe, H. Hosono, Y. Hikichi and L. L. Hench, J. of Maters. Sci. Letters 9 (1990) 1443-1444.

"Optical Composites," L. L. Hench, Ceramic Transactions, Vol 19, Advanced Composite Materials, M. D. Sacks, ed., Am. Ceram. Soc., Westerville, OH, 1991, pp. 265-278.

"Molecular Orbital Calculations on Water Adsorption on a Tetrasiloxane Ring Using the AM1 Semi-Empirical Hamiltonian," J. K. West and S. Wallace, Ceramic Transactions, Vol 19, Advanced Composite Materials, M. D. Sacks, ed., Am. Ceram. Soc., Westerville, OH, 1991, pp. 183-188.

"Ultrastructure Processing," L. L. Hench and B. I. Lee, Encyclopedia of Physical Science and Technology, 2nd Edition, Academic Press, San Diego, CA, 1991.

"Sol-Gel Silica for Precision and Multifunctional Optics," L. L. Hench, Ceramics International 17 (1991) 209-216.

"Molecular Design of Bioactive Glasses and Ceramics for Implants," L. L. Hench in Ceramics: Toward the 21st Century, Naohiro Soga and Akio Kato, eds., The Ceramic Society of Japan, Tokyo, 1991, pp. 519-534.

"The Kinetics of Bioactive Ceramics, Part III: Surface Reactions for Bioactive Glasses Compared with an Inactive Glass," L. L. Hench, O. A. Andersson and G. P. LaTorre, in Bioceramics, Volume 4, W. Bonfield, G. W. Hastings and K. E. Tanner, eds., Butterworth-Heinemann Ltd., Guildford, England, 1991, pp. 155-162.

"Bioceramics: From Concept to Clinic," L. L. Hench, J. Am. Ceram. Soc. 74[7] (1991) 1487-1510.

"Bioceramics," L. L. Hench and J. Wilson, MRS Bulletin XVI[9] (1991) 62-74.

"Evidence for Protonic Conduction in Alkali-Free Phosphate Glasses," Makoto Kotama, Koji Nakanishi, Hideo Hosono, Yoshihiro Abe, and L. L. Hench, J. Electrochem. Soc. 138[10] (1991) 2928-2930.

"An Investigation of Bioactive Glass Powders by Sol-Gel Processing," R. Li, A. E. Clark, and L. L. Hench, J. Appl. Biomaterials 2 (1991) 231-239.

"Sol-Gel Processing of Large Silica Optics," L. L. Hench, M.J.R. Wilson, C. Balaban and J. L. Nogues, in Ultrastructure Processing of Advanced Materials, D. R. Uhlmann and D. R. Ulrich, eds., John Wiley & Sons, New York, 1992, pp. 159-177.

"Quantum Calculations on Sol-Gel Silica Clusters," J. K. West, S. Wallace, L. L. Hench and C. R. Lishawa, in Ultrastructure Processing of Advanced Materials, D. R. Uhlmann and D. R. Ulrich, eds., John Wiley & Sons, New York, 1992, pp. 111-118.

"Real Time Monitoring of Silica Gel Drying Behavior," M.J.R. Wilson, and L. L. Hench, in Ultrastructure Processing of Advanced Materials, D. R. Uhlmann and D. R. Ulrich, eds., John Wiley & Sons, New York, 1992, pp. 247-254.

"Sol-Gel Derived Titania-Silica Gel-Glasses," Yeu-Chyi Cheng and L. L. Hench, in Ultrastructure Processing of Advanced Materials, D. R. Uhlmann and D. R. Ulrich, eds., John Wiley & Sons, New York, 1992, pp. 333-339.

SECTION X

CUMULATIVE LIST OF MIRP PATENTS AND PATENTS PENDING
1988-92

"Alkali-Free Bioactive Sol-Gel Powders," U.S. Patent No. 5,074,916, L. L. Hench, Rounan Li, and A. E. Clark

"Process of Using Type VI Porous Sol-Gel Derived Silica Monoliths for Transpiration Cooled Windows in Rocket Guidance Systems," L. L. Hench, J. K. West, G. P. LaTorre, and A. G. Fosmoe, II

"Low Density Silica Gel Monoliths with Controlled Textures," L. L. Hench, D. Parsell and B. F. Zhu

"Method to Polish Type VI Porous Sol-Gel Silica Monoliths and Remove the Waste Products of the Polishing Process from the Porous Substrate," L. L. Hench, J. K. West, G. LaTorre, B. F. Zhu

"Method and Apparatus Required to Dehydrate Pure Silica Xerogels without Cracking," M.J.R. Wilson, J. K. West and L. L. Hench

"Control of Gel-Silica Structures and Porosities by Aging Treatment," L. L. Hench and S. Liu

"Laser Dye Impregnated Silica Gels," L. L. Hench, J. H. Simmons, B. F. Zhu, R. Ochoa

"Gel-silica Microlenses Made Through Laser Densification," T. Chia, J. K. West and L. L. Hench.

"High Temperature Aging Treatment as a Preparation for Drying Large Pore Silica Sol-Gel Monoliths," A. Fosmoe, J. K. West, G. LaTorre, and L. L. Hench.

"Method for Forming Microoptic Comonents," (Original Title: Negative Microlense Arrays, Microoptical Components, Potential Geodesic Lenses, and Acousto-optic Components) T. Chia, J. K. West, and L. L. Hench.

"Laser Densified Optical Waveguides," T. Chia, J. K. West, and L. L. Hench.

DISTRIBUTION LIST

Capt. Thomas E. Erstfeld   6
Program Manager
Directorate of Chemistry and Materials Science
Department of the Air Force
Air Force Office of Scientific Research (AFSC)
Bolling Air Force Base, DC 20332-6448

Dr. Donald L. Ball   1
Director of Chemistry and Materials Science
Department of the Air Force
Air Force Office of Scientific Research (AFSC)
Bolling Air Force Base, DC 20332-6448

Professor J. D. Mackenzie   1
University of California
Department of Materials Science
 and Engineering
6531 Boelter Hall
Los Angeles, CA 90024

Dr. Norman M. Tallan   1
AFWL/ML
Wright Patterson AFB, OH 40483

Dr. Charles Lee   1
Program Manager
Directorate of Chemistry and Materials Science
Department of the Air Force
Air Force Office of Scientific Research (AFSC)
Bolling Air Force Base, DC 20332-6448